Master Thesis

Master in Energy Engineering

Modelling of secondary batteries for state-of-charge evaluation

Thesis report

Author: Alejandro Zaragoza Soto
Tutor: Francisco Díaz González

Date: September 2019

Escola Tècnica Superior
d'Enginyeria Industrial de Barcelona

Abstract

Energy storage is one of the biggest challenges the energy field is addressing. It is meant to represent the key solution for large penetration of renewables in the grid and for the decarbonisation of the transport sector. Among the different storage technologies, Lithium-ion batteries have become the most reliable, competitive and efficient one for applications like electronic devices, electric vehicles or stationary electricity storage for the residential sector, and several large-scale battery plants are being installed for power system support.

This thesis is focused on the modelling and simulation of Li-ion batteries for the state-of-charge evaluation. Battery models allow to simulate their behaviour under different conditions and to predict their performance without the necessity of a real application. The state-of-charge evaluation is a crucial feature of Battery Management Systems (BMS), as they permit the efficient and safe usage of batteries and they provide useful information about its current state.

In this research, a deep literature review of secondary batteries, including their fundamentals, different chemistries and characteristics is presented, with a special focus on Li-ion batteries. After that, battery models and State-of-Charge (SoC) estimation techniques are also studied and compared.

The case study of the thesis consists in the experimental testing of a maximum voltage of 4.2 V Li-ion battery, and its comparison with different simulated battery models. In order to perform the battery test, an Arduino platform is designed to collect the voltage and current measurements. The results of the test provide the charging and discharging voltage profile of the battery, as well as the state-of-charge profile as a function of the open circuit voltage. The energy efficiency of the battery is evaluated in 89.836 %.

With the experimental test results, three different battery models are presented and implemented in Matlab-Simulink: the simple model, the zero-hysteresis model and the combined model. The off-line SoC estimation technique of Least Squares Estimation (LSE) has been used in all the cases to obtain the model parameters needed to run the simulations.

The simple model simulation satisfactorily reproduces the battery behaviour. The energy efficiency calculated by this model is slightly higher than the real one: 91.279 % and the Root-Mean-Square Error (RMSE) between the test voltage and the model voltage is 0.215 V.

The zero-hysteresis model simulation provides similar results than the simple model, with an energy efficiency of 91.278 % and an RMSE of 0.228 V.

The combined model results to be the most accurate with respect to the test. However, this model is not able to reproduce the battery behaviour for a very low state-of-charge. The energy efficiency of the battery from this model is 89.989 % and its RMSE is 0.1879 V.

Table of contents

List of figures

List of tables

Glossary

EV	Electric Vehicle
BMS	Battery Management System
BESS	Battery Energy Storage System
SoC	State-of-Charge
SoH	State-of-Health
DoD	Depth-of-Discharge
OCV	Open Circuit Voltage
ANN	Artificial Neural Network
EIS	Electric Impedance Spectroscopy
(E)KF	(Extended) Kalman Filter
LSE	Least-Squares Estimation
PWM	Pulse-Width-Modulation
RMSE	Root-Mean-Square Error

1. Introduction

The year 2019 has marked a turning point in history. For the first time, different collectives around the developed world have started to mobilize and take action under the same movement against fossil fuels, greenhouse gas emissions and conservative politics influenced by big corporations of the energy and transport sector. Although scientific community reached a unanimous consensus about the climatic threat the world is facing many years ago, the reality is that the actions that are being taken to stop this crisis are not enough, and we are dangerously close to a non-return point.

If we take a look over the historical data about CO_2 concentration in the atmosphere, it is undeniable that human activity since the industrial and technological revolution has broken the natural course of Earth. In 2019, different official observatories as Manua Loa (Hawaii) or Izaña (Tenerife) has registered concentrations above 415 ppm, a new record in human history (Figure 1).

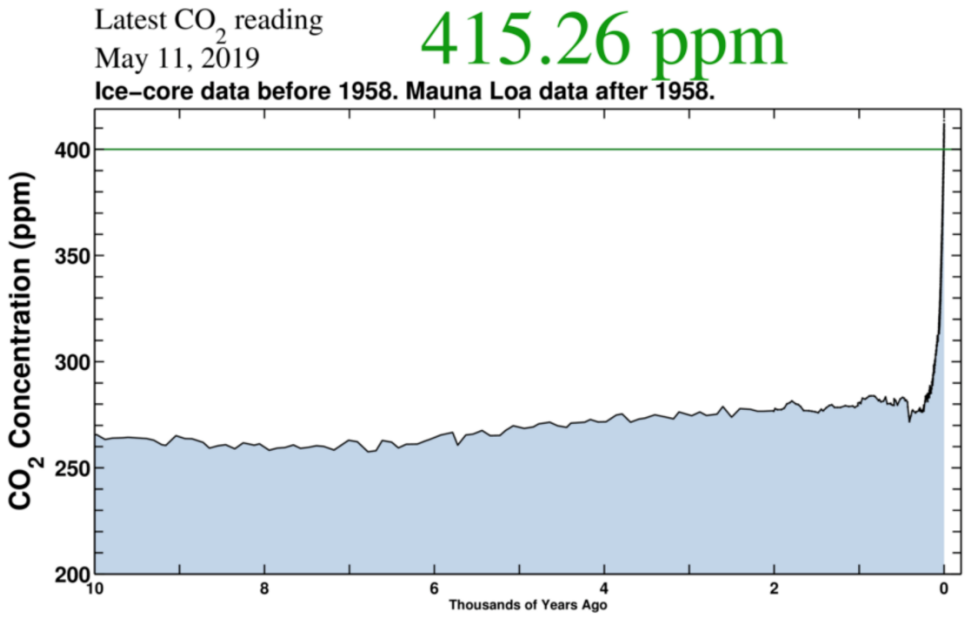

Figure 1. Global CO2 concentration over recent history. Source: [1]

Against this hazard, renewable energies, decentralization of the power systems, decarbonisation of transport and residential sector and energy storage, are key motors in the game, and they should focus the investment and resources of governments and scientific community worldwide. According to [2], renewables will make up 90 % of the European electricity mix by 2040, and electric vehicles (EVs) will add around 3950 TWh of new electricity demand globally by 2050.

This thesis is focused on one of these big challenges: energy storage. Renewables (mostly solar and wind) present an inherent characteristic: they are intermittent. In order to be able to build a reliable, stable power system based on renewables, it is necessary to have the proper technology able to store the excess of energy generated in periods of strong wind and irradiation, and with the capability to deliver it whenever necessary. Moreover, the emergence of EVs in the global transport market implies the requirement of efficient, light, lasting batteries which could reach high levels of autonomy and security.

Among different energy storage technologies, Li-ion batteries have revolutionized the sector, positioning as the main storage solution applied on portable electronic devices, EVs and stationary electricity storage in the residential sector. Although it was an exclusive, expensive technology at the beginning, today Li-ion battery's manufacturing process and production costs, as well as their performance, are difficult to match (Figure 2). This competitive advantage will only grow more and more in the following years when big global powers of the sector (China, USA, Korea and Europe) conduct their projects of Li-ion gigafactories.

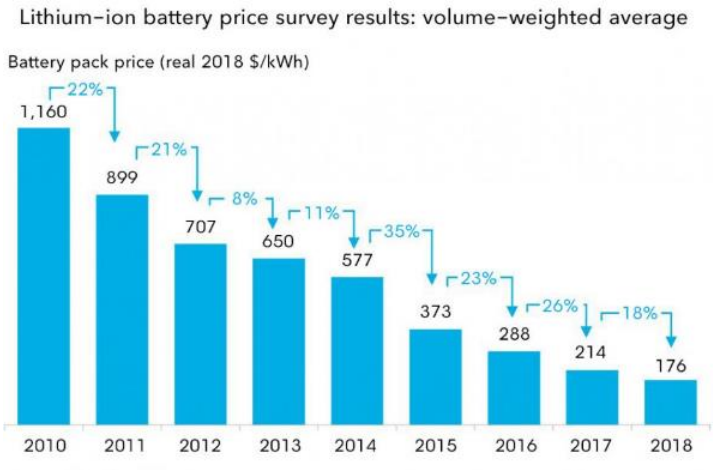

Figure 2. Li-ion batteries price evolution. Source: [3]

With this trend, the perspective of battery market evolution is more than favourable, which indisputably will boost big investors and governments to bet for this technology as a key driver to complete the global energy transition. In Annex A, a list of the biggest Li-ion batteries manufacturers is attached [4]**.**

This thesis is focused on secondary Li-ion batteries, making emphasis in theoretic models that allow to simulate and estimate the stored energy in the battery cells, which is crucial for Battery Management Systems (BMS). In the following section, a comprehensive study of secondary batteries, battery models and State-of-Charge (SoC) estimators is addressed. After that, a case study based on experimental testing and model simulations is conducted, extracting valuable results and conclusions.

2. State of the art

2.1. Batteries and energy storage

The first generation of batteries started with the so-called *voltaic pile* in 1800 invented by Alessandro Volta. By using two different metals (zinc and copper) and salt water, Volta was able to measure a voltage difference between the pieces of metal. At that date, electricity was not yet discovered, so in the first stage, this finding was understood as a constant voltage source. Some years after, thanks to Volta's work, André Marie Ampère discovered the electric current, and this supposed the beginning of electrodynamics [5]. The model and structure of the battery were progressively sophisticated by scientists, prompting the first battery cells. A brief resume of the history of battery development can be consulted in [6].

Generally, battery cells are based on reduction and oxidation reactions (redox). In these reactions, one substance is reduced (it gains electrons) and other is oxidized (it loose electrons). They are composed of two circuits, one internal and other external. The internal circuit is meant as the path that the ions generated in the redox reactions must flow through, while the external circuit is composed of the elements that transport the electrons. The main components of a battery cell are:

- **Electrodes**: pieces of metal where redox reactions occur. The negative electrode (anode) provides electrons to the load and is oxidized during the electrochemical reaction. Conversely, the positive electrode (cathode) accepts electrons and is reduced during the reaction.
- **Electrochemical active substances**: substances in the anolyte and catholyte regions that react with the electrodes substances generating the redox reaction.
- **Electrolyte**: solid or liquid insulating substance that balances the charge of both catholyte and anolyte region by exchanging ions between them.
- **Separator**: avoids direct contact between electrochemically active substances in the anolyte and catholyte regions.

The general structure of a cell is depicted in Figure 3 The two electrodes are made up of two materials called Y0 (for the anode) and X0 (for the cathode). The anode is surrounded by the substance or component Y1, while the cathode is surrounded by the component X1. Both cathode and anode are also surrounded by the electrolyte, Z. The materials X0–X1 and Y0–Y1 define two pairs of electrochemically active substances that have a voltage difference. By adding an external load between the electrodes, the electrical circuit is closed and the battery is discharged, which means that redox reactions start to occur, producing an electric current through the load. The electrons and the positive ions $Y2^+$ result from the oxidation reaction between substances Y0 and Y1. The electrons are collected by the cathode, yielding a reduction reaction between substances X0 and X1, which in turn results in the ion $X2^-$. The internal circuit allows the ionic exchange. In this process, the active substances are eroded, so the electric potential between them is diminished.

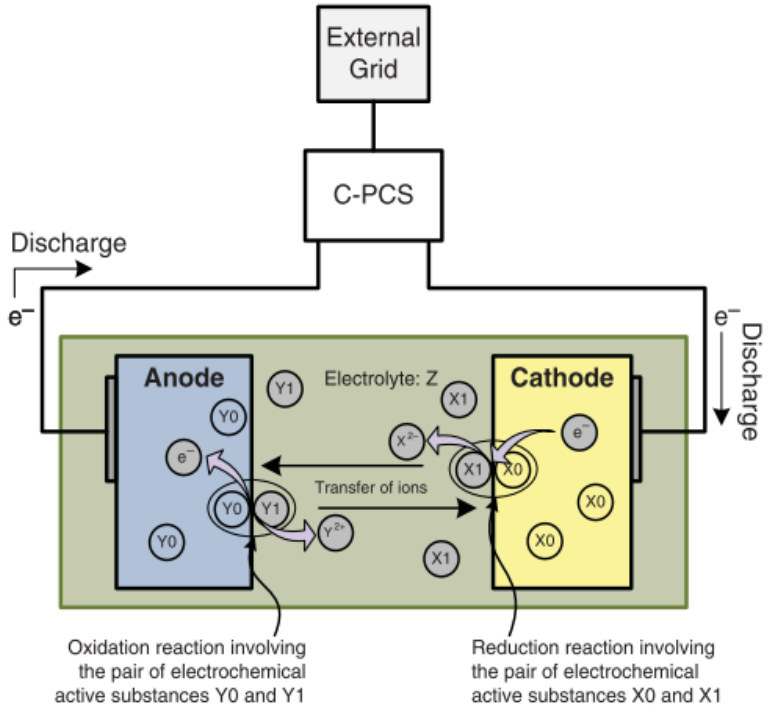

Figure 3. General structure of a battery cell. Source: [7]

There are two types of batteries: primary and secondary batteries. Primary batteries are those which can only be used once. The electrochemical active substances have a maximum voltage difference that is reduced during the discharging process until they decompose totally [8].

In secondary batteries or rechargeable batteries, the electric potential difference can be restored by applying an external electricity source that reverses the electric current to charge the battery. This kind of batteries is the base of modern Battery Energy Storage Systems (BESSs) that store electric energy to use it at a later time. The first secondary battery technology was the lead-acid battery, invented in 1859 by Gaston Planté [9].

The deployment of secondary batteries has been enormous in the last years, being used in transport, telephone exchange, electronic portable devices or emergency lighting, and they constitute one of the principle technologies used to store energy at a large scale. The classification of secondary batteries can be based on their construction (sealed or vented), the electrolyte (acid or alkaline), end use (stationary or portable) or active substances.

In the last years, Lithium-ion batteries have become the most spread and developed technology for many different applications (EVs, large scale energy storage, portable devices…). As Li-ion is the principal technology studied in this thesis, it will be described in depth later on. In the next section, the main technologies of secondary batteries (apart from Li-ion) attending to their active substances are presented.

2.1.1. Lead-acid Batteries (Pb-acid)

Lead-acid is the elder technology of secondary batteries and has been in the market for over 140 years. They are used mainly for engine batteries and standby/backup systems. The chemistry of the reactions in this kind of cells is:

Anode: $Pb + SO_4^{2-} \Leftrightarrow PbSO_4 + 2e^-$

Cathode: $PbO_2 + 4H^+ + SO_4^{2-} + 2e^- \Leftrightarrow PbSO_4 + 2H_2O$

Total: $Pb + PbO_2 + 2H_2SO_4 \rightarrow 2PbSO_4 + 2H_2O$

As the electrolyte of Pb-acid batteries is consumed during the discharge process, a normal estimator of their SoC is the specific gravity. One of the main problems of this technology is sulfation. This effect is originated when the battery is not charged completely or when it is exhausted. In these cases, sulfate crystals appear decreasing the battery's capacity. Moreover, overcharging scenarios can produce that the water originated in the catholyte region split into oxygen and hydrogen, which may produce explosions because of the flammability of hydrogen [7].

There exist two main types of Pb-acid batteries: flooded and valve-regulated. The problems presented before are related to the most common type, that is the flooded batteries. Valve-regulated batteries are today under research, presenting the advantage of being sealed, which avoids gas leakages. The reason for the vast deployment and use of lead-acid batteries lies on its maturity and low cost.

2.1.2. Nickel-Cadmium Batteries (Ni-Cd)

Nickel Cadmium Batteries are used in calculators, digital cameras, laptops, flashlights, electric vehicles (EVs) and space applications. Depending on the use, they can also be flooded or sealed. The chemistry of the reactions is:

Anode: $Cd + 2OH^- \Leftrightarrow Cd(OH)_2 + 2e^-$

Cathode: $NiO_2 + 2H_2O + 2e^- \Leftrightarrow Ni(OH)_2 + 2OH^-$

Total: $Cd + NiO_2 + 2H_2O \rightarrow Cd(OH)_2 + Ni(OH)_2$

Ni-Cd batteries present several advantages from lead-acid, as they have higher cyclability, high-discharge rates, low operating temperatures and low maintenance. Furthermore, they can be charged with alternating current and overcharges do not affect their performance [6].

The main drawbacks of this technology are the cost of the materials, the toxicity of Nickel and Cadmium and the so-called memory effect, originated from incomplete discharging events. After several cycles, the Depth of Discharge (DoD) is reduced and set to the previous minimum level, yielding a capacity reduction of the cell [7].

2.1.3. Sodium-Sulfur Batteries (NaS)

Batteries based on sodium are relevant because of its high electrochemical reduction potential of 2.271 V, which can yield to a cell output voltage greater than 2 V if it is coupled with an appropriate electropositive substance [6]. The most promising one is the sodium-sulphur battery, whose chemical reaction formulation is:

Anode: $2Na \Leftrightarrow 2Na^{+} + 2e^{-}$

Cathode: $xS + 2e^{-} \Leftrightarrow S_x^{2-}$

Total: $2Na + xS \rightarrow Na_2S_x$

NaS batteries present clear differences from the previous technologies presented. Here, the electrodes are in the liquid state, while the electrolyte is a solid (normally ceramic beta-alumina tubes). This is a recent technology that has presented very good performance in terms of low self-discharge, low maintenance, high energy efficiency and great energy density (151 kWh/m^3), which has propitiated its wide installation for stationary power storage [7].

The development of NaS batteries has been hampered by the necessity of achieving low resistance to the flow of sodium ions through the beta-alumina solid electrolyte and because of problems of dimensional stability for their automatic manufacturing [10]. Significant advantages in the inner circuit should be addressed in order to optimize the ceramic electrolyte/electrode interface. According to the current status of R&D in this technology, NaS has a very promising future in large-scale energy storage. Some of the newest researches are focused on different designs as planar types, new electrode systems workable at low temperature (~100 ºC) and ambient-temperature sodium (ion) batteries [11].

2.1.4. Flow Batteries

Flow Battery Energy Storage Systems (FBESS) have an important difference from the previous technologies. In this case, instead of having an electrolyte inside the cell, there are two aqueous electrolytic solutions stored in external tanks. During charge and discharge processes, the electrolytes are pumped to the cell, where their electrochemically active substances react with the electrodes (redox reactions). Figure 4 shows the operation mode and structure of a general flow battery.

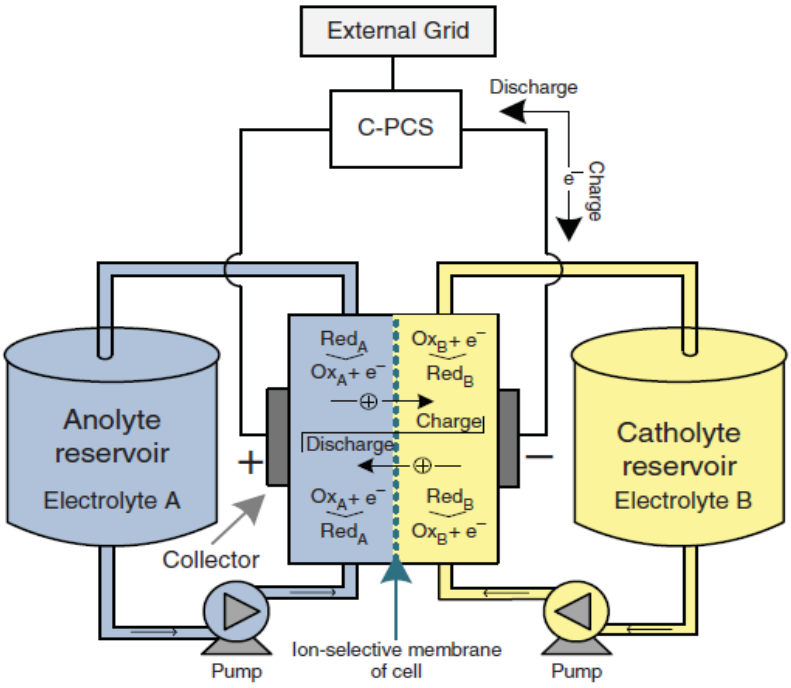

Figure 4. General structure of a flow battery. Source: [7]

The first modern redox flow battery was de Iron/Chromium (FeCr) battery, primarily developed at NASA. They were moved out of the market because of their required high operation temperature and the consequent high cost [12]. Today there are two main families of flow batteries by their active substance:

Vanadium-based Flow Batteries (VFB)

The most studied and installed vanadium flow batteries use graphite based electrodes (anode and cathode) and sulphuric acid as an electrolyte with dissolved vanadium sulfates, with a polymer membrane separating the two regions [7]**.** The global redox chemical reaction is:

Anode: $V^{2+} \Leftrightarrow V^{3+} + e^-$

Cathode: $VO_2^+ + 2H^+ + e^- \Leftrightarrow NVO^{2+} + H_2O$

Total: $V^{2+} + VO_2^+ + 2H^+ \Leftrightarrow V^{3+} + VO^{2+} + H_2O$

This chemistry corresponds to the first generation of vanadium-based flow batteries. This technology is considered competitive with other secondary battery systems thanks to the large availability and low price of vanadium, high energy efficiency, long life cycle and low toxicity [13]. However, its low specific energy (15-25 Wh/kg) and its narrow operating temperature (10-40 ºC) reduce its possibilities for large-scale deployment.

Further researches led to the second generation of VFB based on a mixture of vanadium chloride and vanadium bromide as an electrolyte, improving the solubility of the active substance and the specific energy (25-50 Wh/kg) [14]. And more recently, an American laboratory presented the third generation of VFB that uses H2SO4/HCl electrolyte solution in both half-cells, which improves stability and solubility over a wider range of operating temperatures [15].

Zinc-Bromide Flow Batteries (ZBB)

In ZBB cells the electrodes are based on a carbon-plastic composite. The electrolyte is an aqueous solution of dissolved zinc bromide salts, and the separator used to be made up of polyolefin sheets [7].

The global redox reaction is:

Anode: $Zn_{(s)} \Leftrightarrow Zn^{2+}_{(aq)} + 2e^-$

Cathode: $Br_{2(aq)} + 2e^- \Leftrightarrow 2Br^-_{(aq)}$

Total: $Zn_{(s)} + Br_{2(aq)} \Leftrightarrow 2Br^-_{(aq)} + Zn^{2+}_{(aq)}$

This chemistry is the base of the most studied and developed Zinc-based flow batteries. Together with zinc-ferrycyanide batteries, they have been commercialized for more than 40 years up to MW scale for diverse applications as load-levelling or EVs. They present relatively high cell voltages around 1.7 V, good reversibility and the advantage of the use of abundant, cheap active materials. Moreover, liquid-phase positive active materials allow increasing the storage volumes and the concentrations of the positive electrolytes. Their main barrier is the low current density (~50 mA/cm^2) [16]**.**

Recent studies have introduced attractive new positive species as organic active materials or Iodine, showing a reasonable performance. In addition, other systems involving gaseous positive active materials are under study, mainly by using oxygen [16]**.**

Apart from the chemistries mentioned before, other solutions are under study in order to find new technologies that overcome the main drawback of current flow batteries: the low energy density. For instance, a concept that enhances the energy density is the redox targeting [17] applied in flow batteries based on lithium metal anodes, or storage tanks with solid/semi-solid active materials, presenting better results in energy density [12]**.**

2.2. Lithium-ion technology

'Lithium-ion batteries' is a general term that includes all those batteries that exchange Li-ions between their electrodes. They were introduced in the '90s by Sony Corporation, and in a few years they have become the most promising battery technology for a wide range of applications such electronics, EVs and stationary electricity storage. The main reason for this boost is that lithium is the most electropositive and lightest metal in the Earth, which provides the best characteristics for battery development.

2.2.1. Electrochemistry

In this section, the specific electrochemistry of general Li-ion batteries is presented. The material in the cathode is lithium metal oxide, where the most common is the lithium cobalate (LCO). The negative electrode is basically carbon (C) and lithium atoms. Regarding the electrolyte, the most typical form is an organic solution of lithium-based dissolved salts ($LiPF_6$, $LiClO_4$…). In the case of the separator, it used to be a porous material based on polyethylene or polypropylene. The schematic representation of a typical discharging process of a Li-ion battery is presented in Figure 5.

The global redox reaction of a generic metal Li-ion battery can be written as:

Anode: $Li(C) \Leftrightarrow Li^+ + e^-$

Cathode: $Li^+ + e^- + CoO_2 \Leftrightarrow LiCoO_2$

Total: $Li(C) + CoO_2 \Leftrightarrow LiCoO_2$

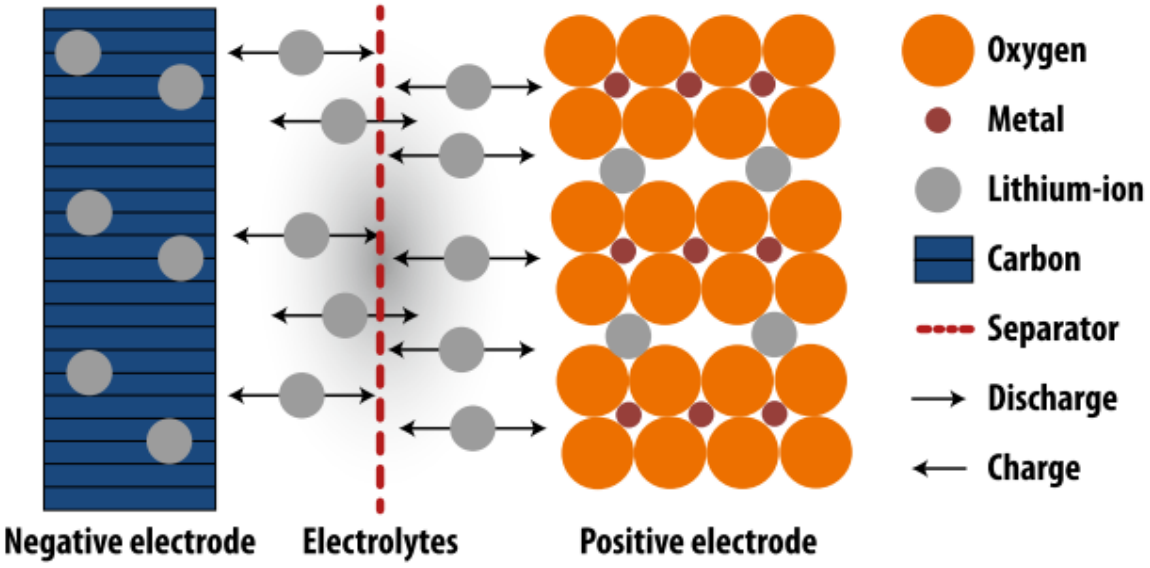

Figure 5. Scheme of a discharging process in a Li-ion battery. Source: ISEA, 2012

Lithium ions are extracted from the cathode during the charging process and they are incrusted into the graphite electrode. The free electrons flow through the external path closing the circuit. In these reactions, the voltage difference between electrodes reaches up to 3.7 V, which is the highest potential any battery technology currently generates [7].

As commented, there are several lithium-based battery technologies, differing between them in their active materials (basically the cathode) and electrolyte. The main families of lithium batteries are commented in the following paragraphs.

Lithium cobalt oxide (LCO) and nickel cobalt aluminium (NCA)

Lithium-cobalt oxide was he first technology commercialized in lithium. It presents a higher energy density compared to other li-ion types. However, this kind of cells has several disadvantages or drawbacks that have placed these batteries out of the market: short lifespan, limited charging rates and low thermal stability. Because of that, their application is reduced to electronics and communication market, but they are not suitable for stationary applications.

An improvement of LCO came with the show up of nickel to use it instead of cobalt with the addition of aluminium atoms, also called lithium cobalt aluminium (NCA). These new materials solve some problems of the previous LCOs as higher energy density and lower cost, and better thermal stability thanks to the aluminium doping [18]. NCA improvements have yielded their utilization in electromobility (e.g. Tesla Motors EVs).

Lithium nickel manganese cobalt (NMC) / lithium manganese oxide (LMO)

Nickel-manganese-cobalt (NMC) cells appeared as a consequence of the research for cheaper elements for battery cells due to the high cost of cobalt. The proportion of these three materials is not standard, and several options have been studied and implemented from 1/1/1 (which means the same ratio of Ni, Mn and Co) to 5/3/2 or 4/4/1, providing different characteristics and operation. NMC are usually utilised in stationary applications and EVs.

In the case of lithium manganese oxide batteries (LMO), they offer higher rates of charge/discharge. The principal advantage of LMO is that manganese is very cheap (around five times less than cobalt). However, their energy density and cyclability are low. The main application of this kind of chemistry is traction.

An interesting strategy is to combine NMC-LMO cells that provide a balanced performance and cost.

Lithium iron phosphate (LFP)

The crystalline structure of LFP atoms provides better thermal stability compared with other chemistries, which makes them the safest option nowadays in the market. Phosphate cathode is non-toxic, so they are more environmentally friendly. Regarding its operation features, LFP offers relatively high power capability and cyclability. In addition, the wide range of discharge rates make them suitable for stationary applications and specially for electromobility.

The negative side of this chemistry lays in the low-rated cell voltage it offers, which yields in a lower energy density. This problem is under research, and the addition of metal atoms of vanadium or titanium, or the reduction of particles to nanosize, seems to be very promising alternatives.

Lithium titanate (LTO)

Although graphite is the most extended element for anodes in Li-ion batteries, the lithium titanate is gaining interest in recent days in particular for stationary applications. The advantages of titanium over graphite are related to power and chemical stability. Moreover, LTO structure enables faster ion flows, which permits faster charging.

Cell voltage in LTO is considerably reduced from other Li-ion batteries (2-2.5 V) but still is higher than lead acid or nickel-cadmium. Over all the advantages, the safety in operation of LTO is the most relevant. Titanate high potential prevents electrolyte decomposition, which is related to overheating and capacity fade problems inside the cell. Estimations predict highest cyclability figures for LTO, up to 20,000 cycles or more. For now, the reduced volume of production implies costs too high to be deployed at large-scale.

2.2.2. Characteristics and comparison

As exposed before, different substances and combinations have been used in the battery industry in order to gradually upgrade the performance of the battery. Today, the Li-ion batteries have reached the front position in the market for most of the applications, but the rest of technologies as lead-acid or molten salts are still used. None of the chemistries presented here is totally obsolete, and deep research is being conducted in every typology of battery.

In this section, a summary table of the principal kind of secondary batteries is presented, gathering the most important characteristics of each of them in terms of voltage, application, efficiency or lifespan.

The data used in Table 1 is indicative and extracted from the literature review already presented and commented. The specific values of this characteristic may differ from one model to another of batteries, and depend on the manufacturing process, materials and shapes.

Table 1. Characteristic of batteries by type

Type	Subtype / Chemestry	Operating Voltage (V)	Nominal Voltage (V)	Operative Temperature (C)	Cyclability	Energy Density (Wh/kg)	Monthly self-discharge	Efficiency	Maximum discharge rate
Lead-acid	Pb-H_2SO_4	1.75-2.27	2	(-40,50)	1200 (80% DoD, C/8)	170	2-4%	70-80%	1C cont.
Alkaline	Ni-Cd	0.9-1.5	1.3	(-20,60)	800 (80% DoD, C/8)	213	10%	60-80%	10C cont.
Molten Salt	NaS	2.31-1.63	2.1	(-300,350)	4500 (80% DoD, 1C)	783	0%	89%	1C cont/5C peak
Li-ion	LCO	4.2-3.0	3.6	(-20,55)	3000 (80% DoD, C/8)	709	<5%	>92%	1C cont. / 30C pulse
	NMC	4.1-3	3.7	(-20,55)	2500 (100% DoD;C/2)	837	<5%	>92%	5C cont. / 30C pulse 35C
	LMO	4.2-3	3.37	(-20,55)	>2000 (100% DoD;1C)	625	<5%	>92%	10C cont. / 40C pulse
	LFP	3.6-2.5	3.3	(-30,55)	>3000 (100% DoD;1C)	479	<3%	>92%	35C cont. / 30C pulse
	LTO	2-2.5	2.4	(-40,55)	6000 (90% DoD;5C)	30-110	2-5%	98%	1C cont. / 25C (40A pulse)

2.3. Battery modelling

Battery models are important to test, analyse and study the behaviour of the batteries in different scenarios and environments. As normally it is difficult to perform this studies in real-time operation, operative and accurate models are crucial for the correct implementation of BMS, for detecting errors and weak points of the systems and for the identification of important parameters that affect the battery behaviour, lifespan and safety. There exist numerous models in the literature that differs in the accuracy, complexity, parametrization effort and the phenomena they reproduce. Accordingly, the selection of the suitable is normally a trade-off of the previous aspects.

Diverse classifications of battery models can be found in the literature. *Díaz et. al.* [7] distinguished four different groups of battery models according to their approach: electrochemical, analytical, stochastic electrical circuit models. More recent works as *Saidani et. al.* [19] and *Barcellona et. al.* [20] present slightly different categories based on the specific physical aspect reproduced (electrical, physical, aging models…) or the methodology they use (mathematical, physical, circuital approaches). By cross-referencing all the sources consulted, the principal models are described down below.

2.3.1. Electrochemical models

Electrochemical models, physics-based models or *white boxes* are based on partial differential equations (PDE) and their aim is to reproduce electrochemical reaction effects. They link physical parameters to internal electrochemical dynamics of the cell, so they reach high accuracy, but their complexity and processing capacity required are also high. Because of their large number of parameters, their application on dynamic simulation environments is limited [7].

2.3.2. Analytical and stochastic models

Analytical and stochastic models or *black boxes* are based on a mathematical approach. They are described by simple equations, analytical or stochastic functions, and they try to reproduce the external behaviour of the system without going deep into the chemistry of the cell [20]. Stochastics are hardly implementable in dynamic simulation environments, as for the case of electrochemical models. In the case of analytical models, they can be used in the estimation of the SoC, but are not suitable to reproduce the dynamic behaviour of the battery.

For the analytical approach, Peukert's law is one of the simplest and most used models that predicts the capacity of a battery [21] Other usual models are the Kinetic Battery Model and the Diffusion Model [22]**.**

Stochastic models are based on Markov chain which allows predicting a future step of the system by only knowing the present state (memoryless process). *Chiasserini and Rao* proposed several stochastic models in this direction [23]**.**

2.3.3. Equivalent circuit models

Equivalent circuit battery models have been developed especially for EV's power control and BMS for power system applications. They are characterized for the use of lumped models, and they are suitable to reproduce *I-V* characteristic curves and dynamic responses. These models represent a good trade-off between mathematical models and physical ones, as they are less complex but accurate enough for their purposes [7]. However, they have limitations in providing insights into the electrochemistry of the cells, so they cannot be used to study effects like degradation or capacity fading [24]**.**

Inside this category, there exist two principal kinds of models: electrical and impedance based models. The ideal electrical model is formed by a voltage source that reproduces the OCV Figure 6a. From here, the model can be upgraded by the addition of a resistor that simulates the internal resistance of the battery Figure 6b and several RC parallel blocks that reproduce different dynamic behaviours of the battery Figure 6c. This last option is called Thevenin model in the case of one RC branch and Extended Thevenin model for two to *n* RC branches.

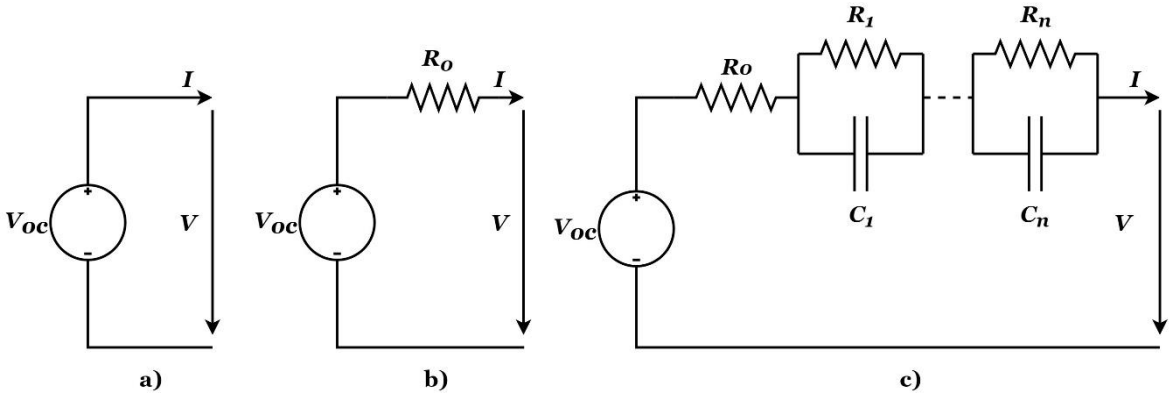

Figure 6. Electrical models of batteries

A notorious work on the battery modelling based on this topology of electric circuits is the one performed by *Plett* from 2004 [25]–[27]. In his work, Plett started from the topology conformed by the voltage source in series with a resistance Figure 6b and proposed several lumped models including Kalman filters to analyse also the hysteresis effect:

- Simple model
- Combined model
- Zero-state hysteresis model
- One-state hysteresis model
- Enhanced Self-Correcting (ESC) model (two-state low-pass filter)
- Enhanced Self-Correcting (ESC) model (four-state low-pass filter)

Models based on RC branches have been also studied in detail in many works. *Hu et al.* [28] developed a comparative study of the twelve most common circuital models and compare the practicality of them according to their complexity, accuracy and generalizability. Their summary table is highly recommended to check the different model equations and the description of each method.

2.4. Methods of SoC estimation

The SoC of a battery, which is used to describe its remaining capacity, is a crucial parameter for control strategy, for the correct management of the energy and for guaranteeing a safe utilization of the system by preventing over-charge episodes that can produce permanent damages. For this reason, scientists and technicians of the sector are putting a lot of effort into its accurate estimation.

The SoC definition is not a trivial issue. The most fundamental expression can be written as follows:

$$SoC\ (t) = \frac{Q(t)}{Q_n} \tag{1}$$

Where $Q(t)$ represents the current capacity and Q_n is the nominal capacity of the battery. The latter is given by the manufacturer and represents the maximum amount of charge that is possible to store in the battery. Conversely, the instantaneous SoC during the real operation of the battery cannot be directly measured. Batteries are complex electrochemical systems, and its operation is affected by multiple variables and effects such as current rate, temperature or historical utilization (SoH). Therefore, this SoC needs to be estimated and thus, reliable and flexible SoC estimators must be developed.

There are many methods studied and applied until now and there is not a perfect one, nor a standard criterion for their classification. The suitability of every method depends on the application, the desired level of accuracy and the computational power required. In order to understand the existing estimators and evaluate their application, several previous works have been consulted.

Rahimi et. al. [29] studied the different approaches available at that date to address the SoC estimation, and discussed their advantages and disadvantages. They divided the methods into five categories: Electrochemical approach, Coulomb counting, open circuit voltage measurement, Kalman filters and sliding-mode observers. Electrochemical approaches are based on detailed electrochemical equations, so they are accurate but difficult to implement *in situ.* The Coulomb counting results easy to implement but they depend on the initial SoC and their application is limited. OCV measurement approach is also easily implementable, but the relaxation effect takes place, limitng again its utilization in real-time situations. Extended Kalman filers and slidig-mode observers solve most of the previous problems while providing high accuracy on the estimations. However, they require more complex algorithms and calculations.

In 2013, *Chang* [11] developed a classification based on the methodology used for the SoC estimation: direct measurement, book-keeping, adaptive systems and hybrids. Inside each category, they collect and explain different methods also commenting their extends. Also in 2013, *Lu et. al.* [30] developed a classification of methods, this time attending to the algorithms they are based on. In this research, the advantages and disadvantages of each method, as well as its input variables, are gathered in a summary table.

Just to give one more example of research which contains a comparison of SoC estimation methods, *Kalawound* [31] developed an exhaustive literature review of previous works and ended to present a novel classification of estimators with regards to their concept, adaptability and performance in real-time applications. By doing this, the authors wanted to identify the to-be improved aspects of existing methods in order to find de *ideal one.* With this disruptive classification, the methods can be characterized according to their type of input (online, offline or estimated), their SoC model (lookup table, physical or statistical) and the type of processing the results (open-loop or closed-loop).

To give some examples, the simple SoC estimation method based on Ah-counting uses online measured variables that are processed in a lookup table or by statistics models, and they provide an estimation of the SoC without any further processing.

In the case of the method of Open Circuit Voltage estimation, it uses estimated OCV input that can be correlated by a lookup table or a regression model with the SoC, and the results can be processed in an open or closed-loop to minimize the error.

Finally, the example of using an Artificial Neural Network (ANN) to estimate the state-of-charge can be characterized for using online measured variables, statistical regression models based on non-linear equations and closed-loop processing of the results.

This review of existing methods and classifications for the state-of-charge estimation can be used as a guide-map for evaluating different methodologies and to find the most suitable approach depending on the specific situation of each project. Table 2 summarizes the consulted publications and includes the references for further quests.

Table 2. Summary of SoC methods and classifications by author

Source	Category	Method
Rahimi, 2012 [29] by approach		Electrochemical
		Coulomb-counting
		Open Circuit Voltage measurement
		Extended Kalman Filter
		Sliding mode observer
Chang, 2013 [11] by methodology	Direct Measurement	Open Circuit Voltage
		Terminal Voltage
		Impedance
		Electric Impedance Spectroscopy (EIS)
	Book-keeping estimation	Coulomb-counting
		Modified Coulomb-counting
	Adaptive systems	BP neural network
		RBF neural network
		Support vector machine
		Fuzzy neural network
		Kalman filter
	Hybrid methods	Coulomb-counting and EMF
		Coulomb-counting and Kalman filtering
		Per-unit system and EKF
Lu, 2013 [30] by algorithm		Discharge test method
		Ampere-hour integral method
		Open Circuit Voltage method
		Battery model-based SoC estimation method
		Neural network model
		Fuzzy logic
		Resistance based methods
		Weighted fusion algorithm
		Kalman filter
		Sliding mode observer
Kalawound, 2015 [31]	Input variables and parameters	Input parameter
		Offline measured
		Online measured
		Estimated
	SoC estimation model	Lookup table
		Physical Model
		Statistical regression model
	Type of processing	Open-loop
		Closed-loop

3. Methodology

The methodology followed in this project is resumed in Figure 7. It is divided into three important parts: the first one (orange boxes in Figure 7) comprises the selection of the battery model based on the literature review, its mathematical definition and the identification of its main parameters.

The second stage of the project is the experimental work with Arduino (green boxes in Figure 7). In this section, an electronic circuit attached to an Arduino platform is built in order to perform several tests (charging/discharging). These experiments provide real data about the Li-ion battery studied, giving useful information about battery behaviour, and this data will be used in the next section to run the model.

Once the experimental tests are performed and the results are processed, the project steps forward to a simulation stage (blue boxes in Figure 7). The implementation of battery models and their simulations will be performed using Matlab and Simulink. In this final part, tests data is used to characterize the models defined in the first section and to run the SoC estimator. Finally, the results of the simulation are compared to real data.

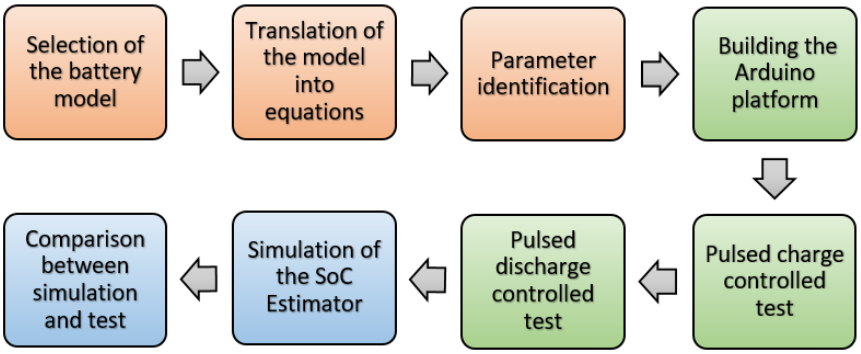

Figure 7. Methodology followed in the thesis

This methodology is designed to be as replicable as possible, in the way that different models, SoC estimators, even batteries, can be used apart from de ones studied in this thesis.

In the following sections, every step of the methodology here described is explained, and the results of the experimental and simulation phases are presented.

4. Battery model selection

In this section, three different battery models are presented: the simple model, the zero-hysteresis model and the combined model. All these three models are based on the topology of an equivalent circuit that corresponds to the one shown in Figure 6b.

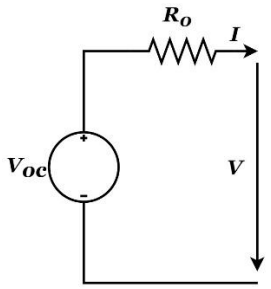

Figure 8. RV model of a battery

Where V_{oc} represents the Open Circuit Voltage, R_0 simulate the internal resistance of the battery, I is the charge/discharge current and V is the voltage output at the terminals of the battery.

As we defined previously, SoC is the ratio of the capacity in every moment and the rated capacity (Equation 1). The capacity of the cell is the specific Ampere-hours that are stored in the cell. Consequently, this capacity is, in fact, the integration of the current over time in a charging process or a discharging process. Considering this, and applying the SoC definition in (Equation 2) the specific SoC can be expressed as:

$$z(t) = z(0) - \int_0^t \eta_i \frac{i(\tau)}{C_n} d\tau \tag{2}$$

Where $z(t)$ is the cell SoC in the time t, $i(t)$ is the instantaneous cell current (positive or negative depending on the regime of the battery), and $z(0)$ is the SoC in the initial state. η_i is the Cell Coulombic efficiency, equals to 1 in the case of discharge and less or equal to one for charge. In a discretized format, and assuming a sampling period Δt, Equation 2 is represented by:

$$z_{k+1} = z_k - \left(\frac{\eta_i \Delta t}{C_n}\right) i_k \tag{3}$$

These equations are a common factor for the three battery models that are studied in this section. In the next subsections, each of the models is characterized by their expression to obtain the cell voltage, and the way to calculate their characteristic parameters.

4.1. Simple model

In the simple model, as well as the majority of the other equivalent circuit models, the OCV is modelled as a function of the SoC. Going into the mathematical language, this model can be expressed by:

$$y_k = OCV(z_k) - R_0 I_k \tag{4}$$

Where now y_k, z_k and I_k are the battery terminal voltage, SoC and current, respectively. At this point, the battery model is then characterized by equations (3) and (4). The first one is defined as the 'state equation' and the second one is the 'output equation'. This model is 'linear in the parameters', so in order to implement this model into a platform and simulate it, it is necessary to identify the characteristic parameters. In order to calculate the parameters of the model, an offline processing method can be easily applied:

The output vector can be defined as:

$$Y = [y_1 - V_{oc}(z_1), y_2 - V_{oc}(z_2), \dots, y_N - V_{oc}(z_N)]^T \tag{5}$$

And the matrix H as:

$$H = [h1, h2, \dots, h_N]^T \tag{6}$$

Where the rows of H are defined as:

$$h_j^T = [i_j^+, i_j^-] \tag{7}$$

Being i_j^+ and i_j^- the charging and discharging currents respectively, calculated as:

$$\begin{aligned} &i_j^+ = i_j \;\; if \;\; i_j > 0 \\ &i_j^- = i_j \;\; if \;\; i_j < 0 \\ &else \;\; i_j^+ = i_j^- = 0 \end{aligned} \tag{8}$$

Therefore, the matrix equation of the model can be expressed as:

$$Y = H\theta \tag{9}$$

Where $\theta^T = [R^+, R^-]$ is the parameter vector with unknown elements. Considering that the simple model studied is 'linear in the parameters', then the identification of the parameters values of the model can be easily addressed by the Least-Squares Estimation (LSE) technique, resulting in that the vector of unknown elements can be obtained by:

$$\theta = (H^T H)^{-1} H^T Y \tag{10}$$

4.2. Zero-hysteresis model

This model takes into consideration an effect called hysteresis, that is not considered in the simple model. The hysteresis effect is well explained in [32]. Basically, it's a phenomenon in which the voltage lags the expected or estimated OCV when the direction of the current changes (charge/discharge).

In this model, the hysteresis effect is introduced in the form of a new parameter in the voltage expression:

$$y_k = OCV(z_k) - s_k M(z_k) - R i_k \tag{11}$$

Where s_k represents the sign of the current. Given a sufficiently small and positive ε:

$$s_k = \begin{cases} 1 & if\ i_k < \epsilon, \\ -1 & if\ i_k > \epsilon \\ s_{k-1} & if\ |i_k| \leq \epsilon \end{cases} \tag{12}$$

And $M(z_k)$ is half the difference between the extremes of the charging-discharging curve minus the internal resistance loss.

This model is also 'linear in the parameters', so the off-line identification method using LSE technique is used to obtain the unknowns parameters. The output vector is:

$$Y = [y_1 - V_{oc}(z_1), y_2 - V_{oc}(z_2), \dots, y_N - V_{oc}(z_N)]^T \tag{13}$$

The matrix:

$$H = [h_1, h_2, \dots, h_N]^T \tag{14}$$

Where the rows of *H* are defined as:

$$h_j^T = \left[i_j^+, i_j^-, s_j\right] \tag{15}$$

And once again, $Y = H\theta$ where now the parameter vector is $\theta^T = [R_0^+, R_0^-, M]$ and it can be obtained by:

$$\theta = (H^T H)^{-1} H^T Y \tag{16}$$

4.3. Combined model

The combined model takes its name from a confluence of different ways of predicting the terminal voltage as a function of the SoC, as the 'Shepherd model', the 'Unnewehr universal model' or the 'Nernst model' [25]. The equivalent circuit representation of the model is the same as the simple model (Figure 8). But in this case, the mathematical expressions that describe the behaviour of the battery are different.

The expression of the terminal voltage, that depends on the internal resistance R and the SoC z_k now includes some new constants that make the model fit better. This formula is:

$$y_k = K_0 - R_0 i_k - \frac{K_1}{z_k} - K_2 z_k + K_3 \ln(z_k) + K_4 \ln(1 - z_k) \tag{17}$$

The unknown parameters are then obtained following the same procedure as before. As this model is 'linear in the parameters', the LSE technique is adequate to obtain their values. The output vector is defined as:

$$Y = [y_1, y_2, \dots, y_N]^T \tag{18}$$

And the matrix:

$$H = [h_1, h_2, \dots, h_N]^T \tag{19}$$

Where the rows of *H* are defined as:

$$h_j^T = \left[1, i_j^+, i_j^-, \frac{1}{z_j}, z_j, \ln(z_j), \ln(1 - z_j)\right] \tag{20}$$

And where i_j^+ and i_j^- follows the same logic as before:

$$\begin{aligned} i_j^+ &= i_j \;\; if \;\; i_j > 0 \\ i_j^- &= i_j \;\; if \;\; i_j < 0 \\ else \;\; i_j^+ &= i_j^- = 0 \end{aligned} \tag{21}$$

Therefore, the matrix equation of the model can be expressed as:

$$Y = H\theta \tag{22}$$

Where $\theta^T = [K_0, K_1, K_2, K_3, K_4, R_0^+, R_0^-]$ is the parameter vector with unknown elements. Considering that the combined model is also 'linear in the parameters', then the identification of the parameters' values of the model can be addressed by the Least-Squares Estimation (LSE) technique, and the vector of unknown elements can be obtained by:

$$\theta = (H^T H)^{-1} H^T Y \tag{23}$$

5. Experimental testing

In this section, a real lithium-ion battery is tested in several ways in order to obtain useful data and conclusions regarding its behaviour. These tests have been carried out experimentally in a lab environment, and real electronic components have been utilized and integrated into a protoboard. The configuration of the circuit will vary for each experiment.

To do this, an Arduino board has been utilized to connect the electric circuit and the PC. Arduino is an open-source electronics platform based on easy-to-use hardware and software. It is a very cheap, easy way to build electric circuits and obtain outputs from a set of inputs, managed by a code. The Arduino programming language is based on Wiring and is also easy-to-learn even for beginners.

As a generic scheme, the configuration of the Arduino board, the electronic circuit and the PC is shown in Figure 9.

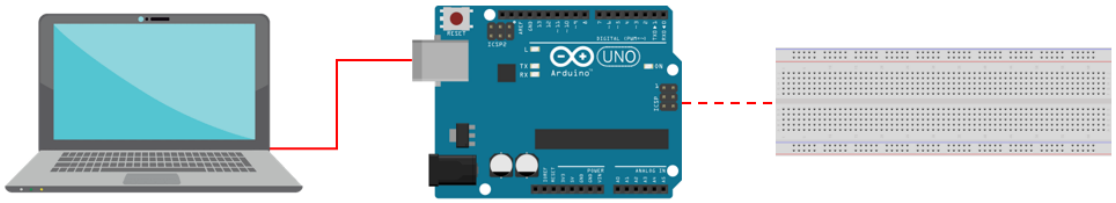

Figure 9. Scheme of Arduino-laptop communication

The Arduino Board used in this project is Arduino UNO. It is a microcontroller that has 14 digital input/output pins (of which 6 can be used as PWM outputs), 6 analogue inputs, a USB connection, a power jack, an ICSP header and a reset button. It can be used as a voltage source of 3.3 V or 5 V (Annex C. Datasheets).

Firstly, the commercial battery used in this project is charged in a pulse controlled procedure. This test will provide information about the capacity of the cell, the charging rates and the transients of voltage change during the charging process. The electric diagram of the circuit for this test is represented in Figure 10.

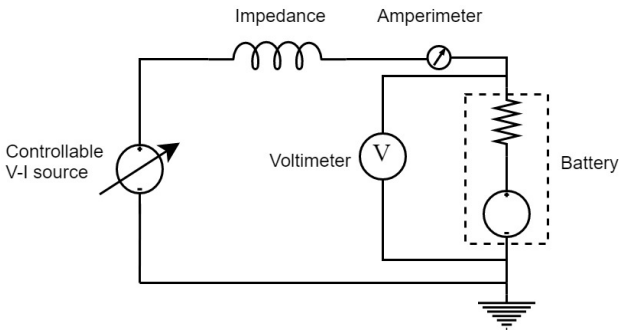

Figure 10. Electric diagram of charging circuit

The real configuration of the circuit is presented in Figure 11.

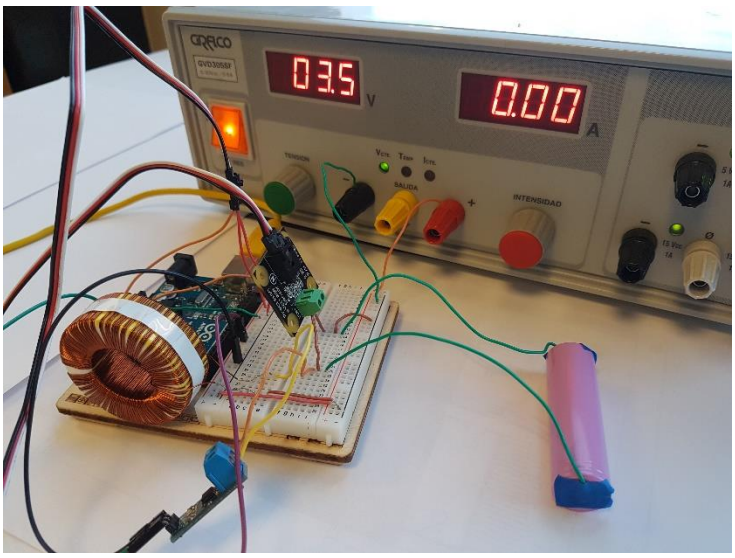

Figure 11. Real picture of the Arduino platform during charging test

Once the battery is fully charged, then the process is reversed and a controlled discharged test is addressed. In this case, the electric diagram of the circuit is shown in Figure 12**.**

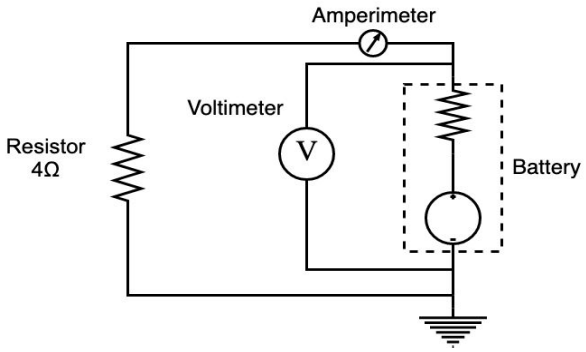

Figure 12. Electric diagram of discharging circuit

Basically, the charged battery is connected to a 4 Ω resistor that dissipates the energy stored in the battery in the form of heat. In opposition to the first test, where the power source allows to maintain a constant current during the process, now the passive device that drives the discharge process cannot assure a constant discharge current according to the Ohm's Law:

$$V = I \cdot R \tag{24}$$

So as the voltage cell is continuously reduced, by connecting a constant resistor the discharge current is then being reduced too.

The results of these test will provide some useful information as mentioned before, and some of them will permit to obtain the necessary parameters to run the battery models simulations.

5.1. Test material

The main devices utilised in this configuration are listed below and their characteristics are shown in Tables 3-8. The datasheet of all of them is attached in Annex C. Datasheets:

- *Arduino UNO board*

Table 3. Arduino UNO Characteristics

Item	Specification
Operating Voltage	5 V
Input Voltage (recomm)	7-12 V
Input Voltage (limits)	6-20 V
Digital I/O Pins	14 (6 PWM)
Analog Input Pins	6
DC Current per I/O Pin	40 mA
DC Current for 3.3V Pin	50 mA
Flash memory	32 kB
SRAM	2 kB
EEPROM	1 KB
Clock Speed	16 MHz

- *Li-ion Battery*

Table 4. ICR18650 battery characteristics

Item	Specification
Model	ICR18650
Nominal Capacity	2600 mAh (0.2C, 2.75V disc.)
Charging Voltage	4.2 ± 0.05 V
Nominal Voltage	3.7 V
Charging Method	CC-CV
Charging Current	Standard: 1300 mA Rapid: 2600 mA
Charging time	Standard: 3 h Rapid: 2.5 h
Max. Charging Current	2600 mA
Max. Discharge Current	5200 mA
Discharge Cut-off Voltage	2.75 V
Initial internal resistance	0.1 Ω

- *Inductor*

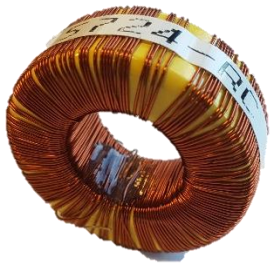

Table 5. Inductor characteristics

Item	Specification
Model	5724-RC
Inductance ± 15 % @1kHz	4000 µH
Current Max.	1.75 A
Inductance Min.	2100 µH
DCR Max.	1.16 Ω

- *Voltage sensor*

Table 6. Voltage sensor characteristics

Item	Specification
Model	1135_0B
Voltage Difference Max.	± 30 V
Measurement Error Max.	0.5 %
Sensor Response Time Max	10 ms
Voltage Offset Max	± 100 mV DC
Supply Voltage	5V DC
Current Consumption Max.	3.6 mA

- *Current sensor*

Table 7. Current sensor characteristics

Item	Specification
Model	ACS712
Measurement Range	± 5 A
Resolution	26 mA
Sensibility	185 mV/A
Voltage Offset Max	2.5 V
Supply Voltage	5V DC

- *Controllable source*

Table 8. Controllable source characteristics

Item	Specification
Model	GVD305
Output Voltage	0 - 30 V DC
Output Current	0 - 5 A
Power	150 W

5.2. Results

This test is carried out in a controlled procedure, where the charging process is assessed by a pulsed current signal of 1 A amplitude. The pulses have been set to last 15 min, and a relaxation period between pulses of 15 min is also necessary in order to lead the voltage cell stabilise. During the discharging phase, the relaxation time between pulses is maintained, as well as the 15 min of pulse. The amplitude of the pulsed current is, however, now function of the voltage drop caused by the internal resistor and the external resistor connected to the circuit. The test results are shown in Figure 13.

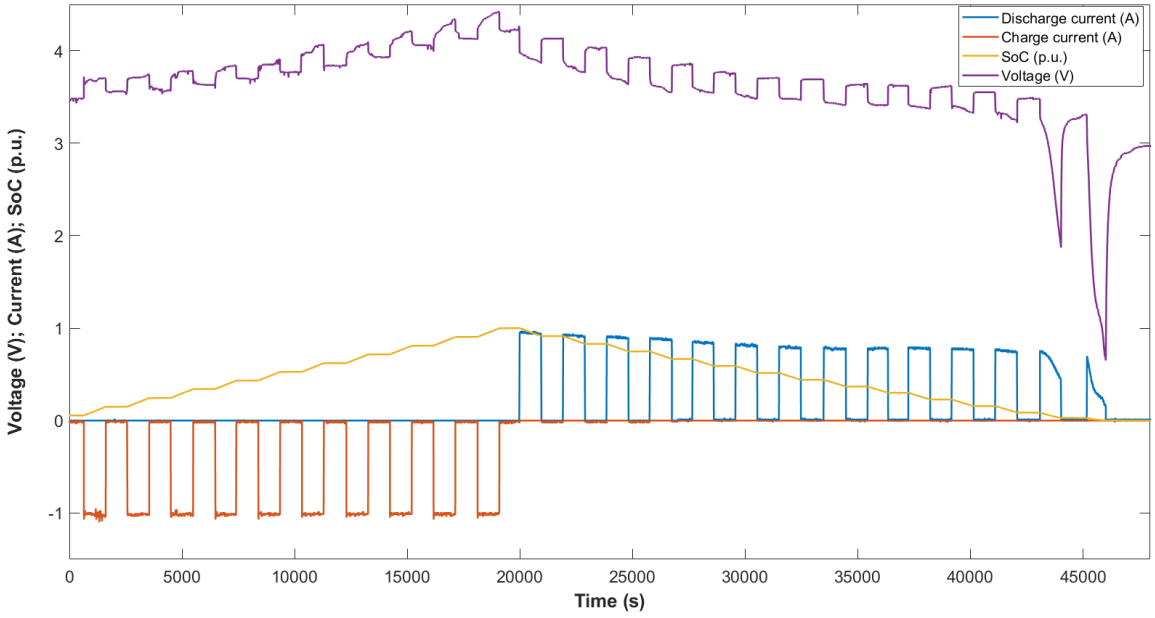

Figure 13. Charging/discharging test results

As it can be observed in the last figure, the sign criteria adopted for the direction of the current is negative while charging the battery, and positive in the discharge process. The Arduino board has been utilised for the data acquisition of voltage and current. The results concerning these variables are directly plotted from the lecture of the corresponding sensors; instead, the state-of-charge is obtained from the application of Equation 3.

The maximum voltage that the battery reaches exceeds 4 V, which is a considerable high value according to Table 4. This level of cell voltage implies a higher energy capacity than other battery chemistries, as commented in the State of the Art section, and justifies why lithium-ion batteries are the most common and spread option for EVs.

Looking more specifically at the voltage curve, it is possible to extract that the internal resistance of the tested battery is low (average value of 0.1 Ω) and it verifies the internal resistance value given in the product's datasheet (see section 5.1). This resistance is caused by the electrodes and electrolyte that try to oppose the current flow inside the cell. Making zoom-in to the voltage and isolating a certain pulse (Figure 14), the voltage drop caused by this resistor can be easily observed and it has an average value of 0.1 V as expected, given a 1 A pulse and a 0.1 Ω internal resistance (Equation 24).

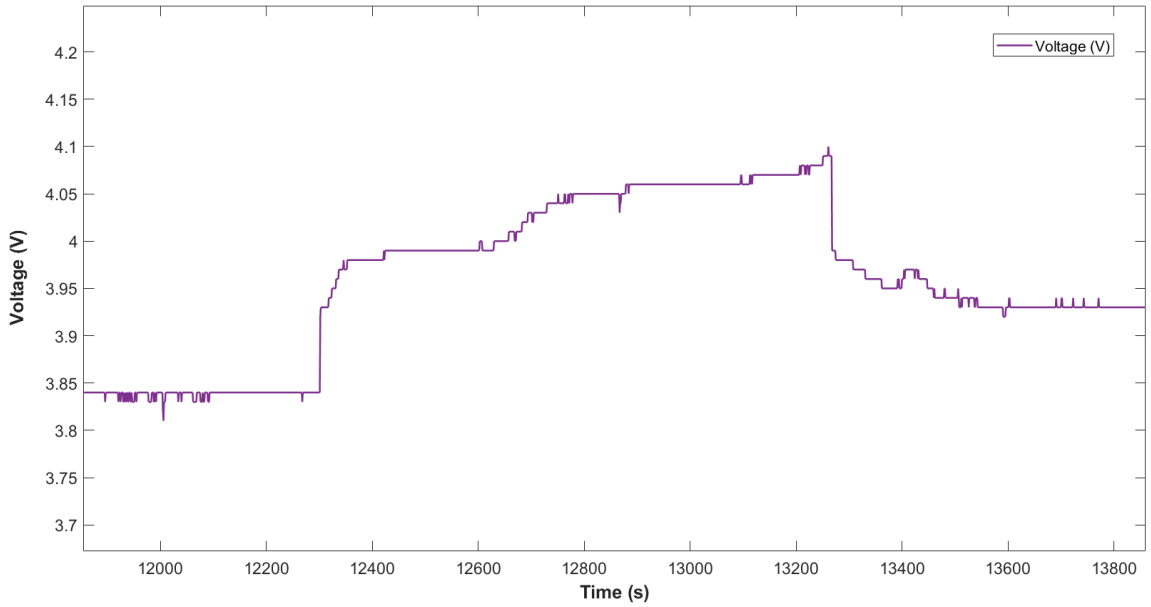

Figure 14. Test charging pulse

Moreover, Figure 14 serves to justify why it is necessary to assure a sufficient relaxation period to stabilise the voltage and be able to read and estimate the state-of-charge from it. As it can be appreciated when the pulse is over (around second 13250), the voltage shows a transient until second 13600 to clearly reach a steady state, which means that the battery needs 5.8 min to stabilise.

Also, it is noticeable that, in the discharge test, the voltage pattern suddenly changes when it reaches certain level. When the SoC is approximately 9 % (around 3.5 V), the voltage drops steeply when the pulse is applied. This phenomenon reflects that the battery has been over-discharged. Going further than this point can cause damage in the internal chemistry of the cell (it will lose capacity) and even may cause the ruin of the device. That's the reason why most of the electronic devices that use li-ion batteries are programmed to turn off when at this level in order to prevent possible damages.

The Open Circuit Voltage (OCV) curve of the battery can be also obtained from the test. To do so, it is necessary to read the voltage during the relaxation periods, and then interpolate through time in order to get a continuous curve. The resultant curve is shown in Figure 15**.** Looking at the OCV variation, it is possible to declare that it varies considerably over time during the charge/discharge process. This fact is perfect for SoC estimators used in BMS, so it is possible to accurately identify the level of charge by reading the voltage. In other chemistries of batteries, as LTO, the OCV variation in time is smoother and the slope of the curve is flatter, so there exist more uncertainty in the SoC estimation, and more complex and precise models are needed.

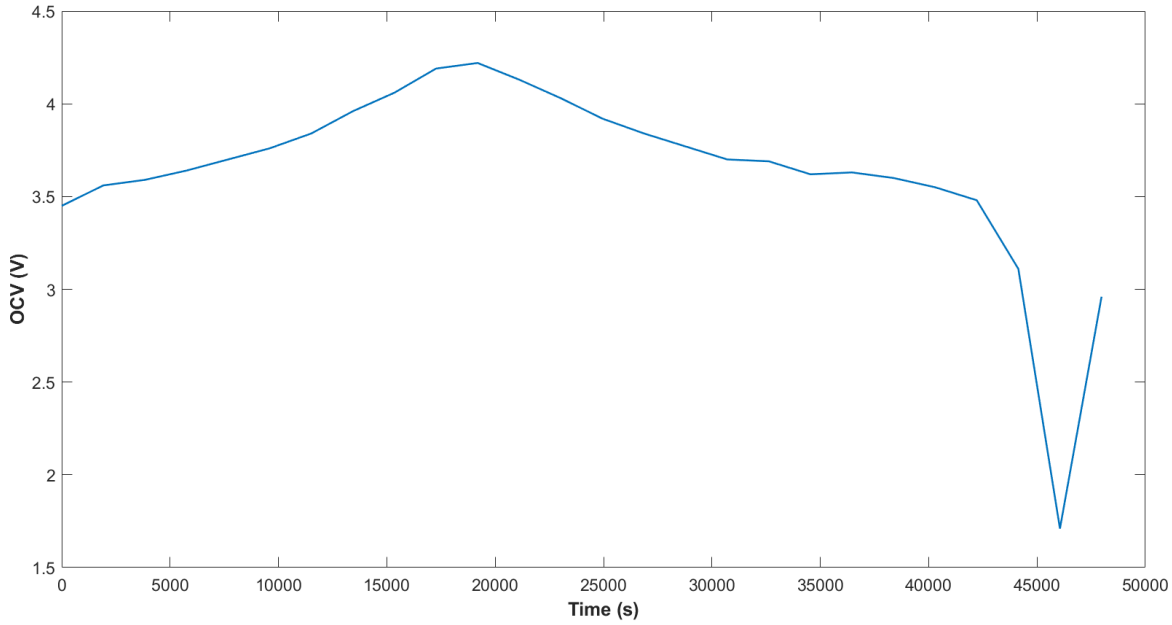

Figure 15. Test OCV curve

Finally, the correlation between OCV and SoC is represented in Figure 16. This is the main result of the test, as it allows to know the state-of-charge of the battery according to the cell voltage. This is, in fact, the principle that BMS use in their algorithms to estimate the SoC of the battery of any electronic device.

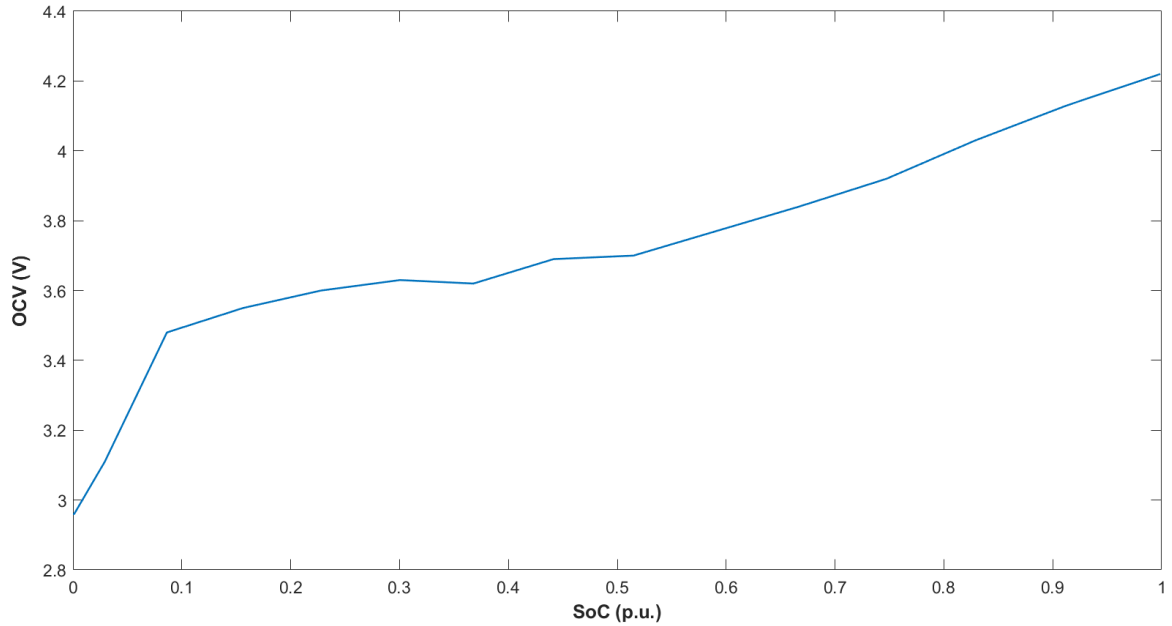

Figure 16. Test OCV-SoC curve

In the OCV-SoC curve, we can identify two different behaviours: when the battery is fully discharged, the slope of the curve raises drastically up to 10% charge. It is nothing but reversing the pattern already analysed in the previous results. In the gap between 0% and 10% SoC, the terminal voltage changes in a clear faster rate than it does from 10% to 100%.

6. Battery model simulation

6.1. Simple model simulation

The simple model, which was defined in section 4.1., is now implemented and simulated in order to obtain the voltage cell profile during charge and discharge. The Matlab code generated to carry out this simulation is attached in Annex B. Codes at the end of this thesis. Following the procedure explained in section 4.1., the resulting parameters of vector θ are shown in Table 9:

Table 9. Simple model parameters result

Parameter	Result
R_{charge}	0.1340 Ω
$R_{discharge}$	0.2738 Ω

The model has been implemented in Matlab and simulated with Simulink. A scheme of the model is represented in Figure 17.

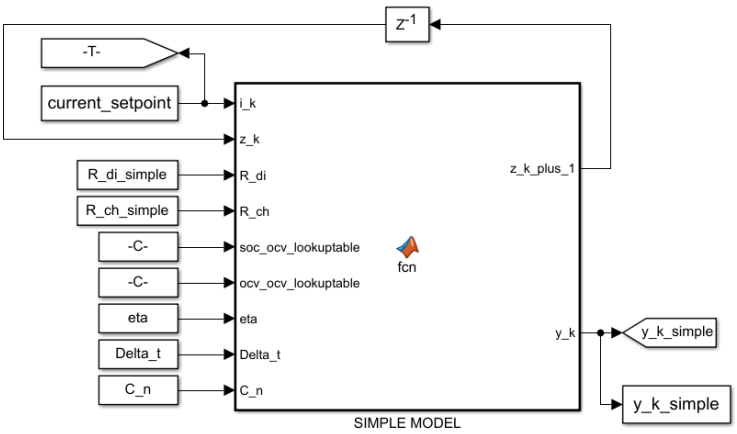

Figure 17. Simple model Simulink diagram

Where the inputs of the simple model function are:

- *I_k* is the current signal from the experimental test.
- *Z_k* is the SoC in the last state.
- *R_di* is resistor parameter when discharging.
- *R_ch* is the resistor parameter when charging.
- *Soc_ocv_lookuptable* is the vector that contains the SoC profile of the test.
- *Ocv_ocv_lookuptable* is the vector that contains the OCV profile of the test.
- *Eta* is the Coulombic efficiency (=1 in this case).
- *Delta_t* is the simulation time step.
- *C_n* is the nominal capacity of the cell.

And where the outputs are:

- *Z_k_plus_1* is the current SoC.
- *Y_k_simple* is the cell voltage.

By using the experimental test as an input for the current signal, and implementing the equations in the Simulink model, the results of the cell voltage simulated through the simple battery model are presented in Figure 18.

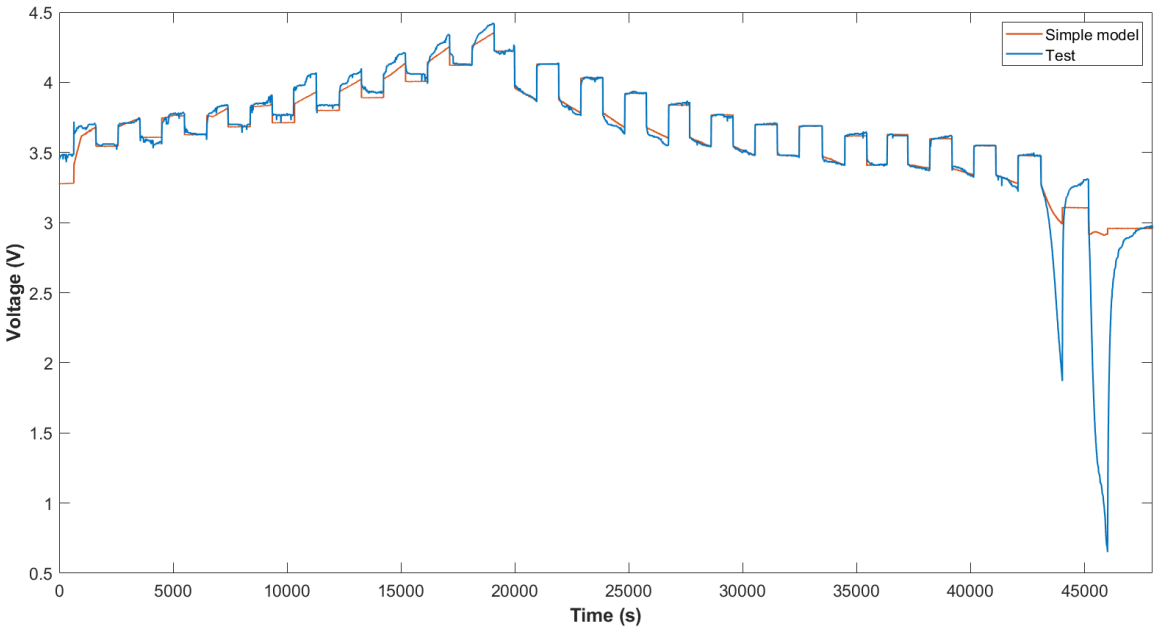

Figure 18. Simple model simulated voltage curve

Analysing the results of the simulation, some first comments arise. Comparing the charging and discharging phases, it is clear than the model fits better with the experimental data in the discharge process. Nevertheless, during the two last pulses where the voltage drops sharply, the model is not capable to represent the real behaviour of the battery.

In the charging phase, the transient in the first loop is slower in the simulation than in the real data. From there on, it is possible to distinguish some pulses where the model functions quite well, with an error between the test and the simulated curve low, and the last pulses where the model always remains lower than the real data during the pulses and the relaxation periods.

The clear difference between the charge and discharge with respect to the accuracy of simulation probably is influenced by the fact that the charging pulses from the test present more noise than in the discharge phase. The explanation of this fact is that the voltage sensor used in this experiment was so sensitive to any perturbation or vibration that the different ambient conditions clearly affected the normal behaviour of the battery.

All in all, the model results to be accurate enough considering the level of complexity its implementation requires, and the number of parameters and variables that considers.

6.2. Zero-hysteresis model simulation

The zero-state hysteresis model has been also implemented in Matlab-Simulink following the structure defined in 4.3. The resulting parameters of vector θ are shown in Table 10:

Table 10. Zero-hysteresis model parameters result

Parameter	Result
R_{charge}	0.1480 Ω
$R_{discharge}$	0.2907 Ω
M	-0.0140 V

And the scheme of the combined model implemented in Simulink is represented in Figure 19.

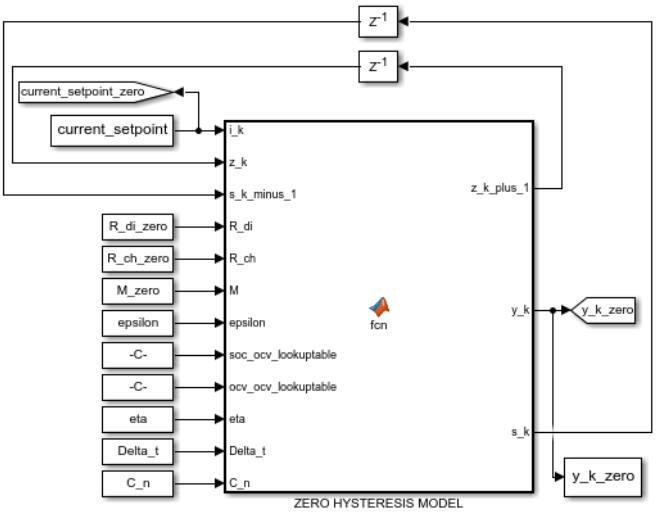

Figure 19. Zero-hysteresis Simulink model diagram

Where the inputs of the simple model function are:

- *I_k* is the current signal from the experimental test.
- *Z_k* is the SoC in the last state.
- *S_k_minus_1* is the previous value of the parameter *s_k* (current sign).
- *R_di* is resistor parameter when discharging.
- *R_ch* is the resistor parameter when charging.
- *M* is the constant that represents the hysteresis level.
- *Epsilon* is a positive constant. In this case, 0.1.
- *Soc_ocv_lookuptable* is the vector that contains the SoC profile of the test.
- *Ocv_ocv_lookuptable* is the vector that contains the OCV profile of the test.
- *Eta* is the Coulombic efficiency (=1 in this case).
- *Delta_t* is the simulation time step.

- C_n is the nominal capacity of the cell.

And where the outputs are:

- $Z\_k\_plus\_1$ is the current SoC.
- Y_k_zero is the cell voltage.
- S_k is the parameter that represents the current sign.

By using the experimental test as an input for the current signal, and implementing the equations in the Simulink model, the results of the cell voltage simulated through the zero-hysteresis battery model are presented in Figure 20.

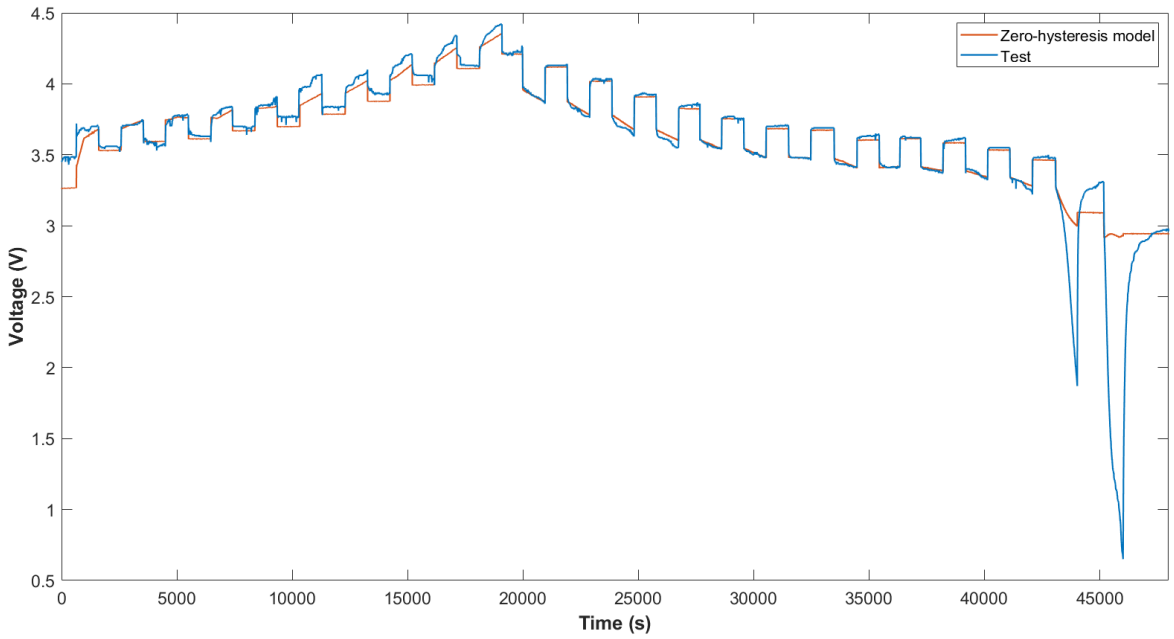

Figure 20. Zero-hysteresis model simulated voltage curve

This model is very similar in its terminal voltage definition to the simple model. Here, only a new parameter that is meant to represent the hysteresis effect is added. Consequently, the result obtained in the simulation reflects almost the same pattern and level of accuracy than the simple model.

As it can be observed in Figure 20, the simulated voltage remains lower than the real voltage during the pulses in the charging process. During the discharge, the value of the simulated voltage neither reaches the real one. In the first pulse of the test, the simulation provides a slow transient response, that starts fitting better in the next pulses. From the fifth pulse, it is noticeable than the experimental data is not so clean and consequently the model cannot reproduce well the battery behaviour. In the case of the last two pulses when the battery voltage is not stable, the model simulation provides a smoother response following the pattern of the rest of the test.

6.3. Combined model simulation

Following the same procedure, now the combined model is implemented in Matlab-Simulink following the structure defined in 4.2. Here, the resulting parameters of vector θ are shown in Table 11:

Table 11. Combined model parameters result

Parameter	Result
K_0	2.7354 V
K_1	0.0363 V
K_2	-1.5167 V
K_3	-0.4413 V
K_4	-0.0029 V
R_{charge}	0.1662 Ω
$R_{discharge}$	0.3016 Ω

The scheme of the combined model implemented in Simulink is represented in Figure 21.

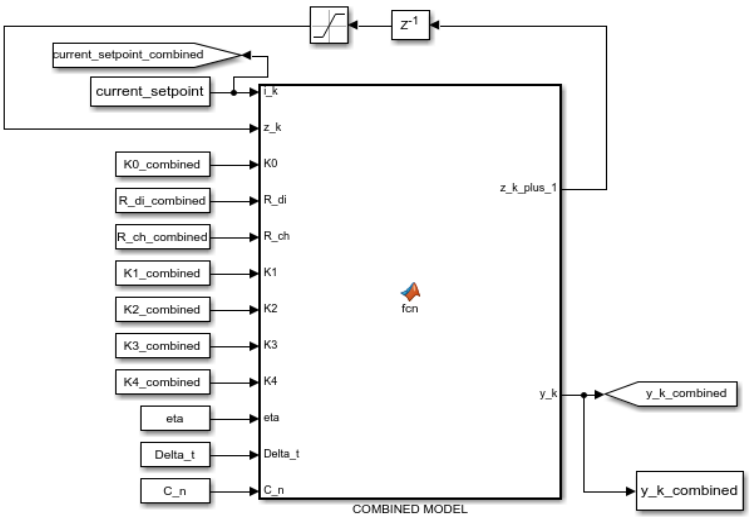

Figure 21. Combined model Simulink diagram

Where the inputs of the combined model function are:

- *I_k* is the current signal from the experimental test.
- *Z_k* is the SoC in the last state.
- *K0_combined* is the K0 parameter of the model.
- *R_di* is resistor parameter when discharging.
- *R_ch* is the resistor parameter when charging.
- *K1_combined* is the K1 parameter of the model.
- *K2_combined* is the K2 parameter of the model.

- *K3_combined* is the K3 parameter of the model.
- *K4_combined* is the K4 parameter of the model.
- *Eta* is the Coulombic efficiency (=1 in this case).
- *Delta_t* is the simulation time step.
- *C_n* is the nominal capacity of the cell.

And where the outputs are:

- *Z_k_plus_1* is the current SoC.
- *Y_k_simple* is the cell voltage.

By using the experimental test as an input for the current signal, and implementing the equations in the Simulink model, the results of the cell voltage simulated through the combined battery model are presented in Figure 22.

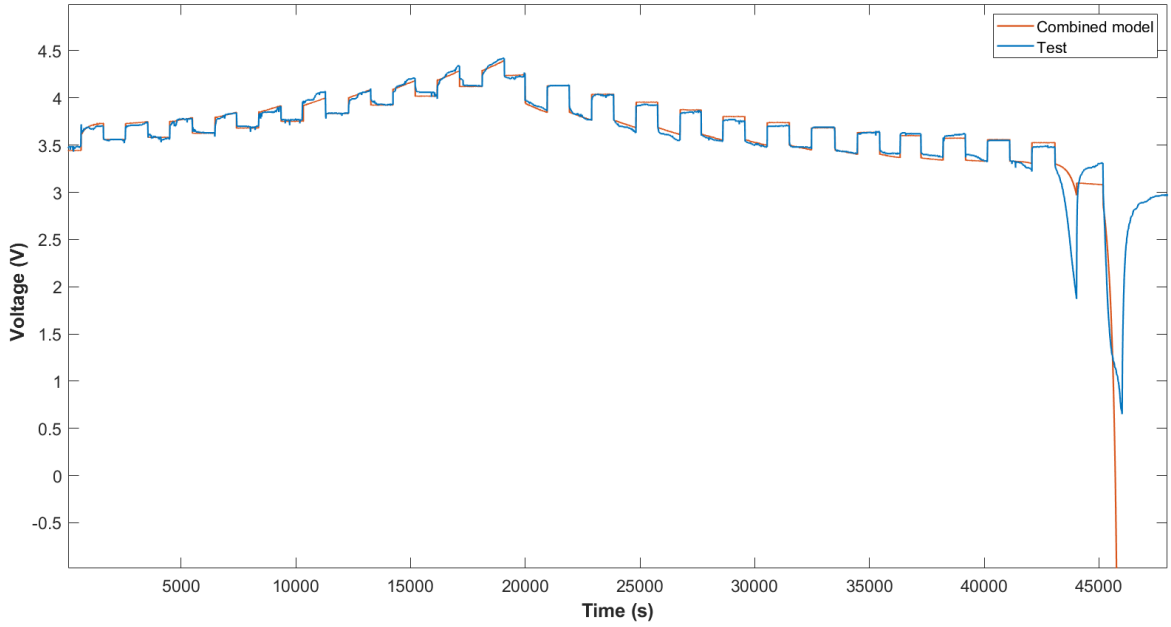

Figure 22. Combined model simulated voltage curve

Analysing the results of the combined model, it is noticeable that it reproduces better the experimental data than the simple model or the zero-hysteresis model. In the first pulse of the test, the significant gap between the simulation and the raw data in the first model is now solved.

On the other hand, the last pulses of the test during the discharge phase present a different result. It is clear in Figure 22 that the combined model is not able to reproduce the battery behaviour when the SoC is very low. To better appreciate this phenomenon, in Figure 23 a zoom-in of the last pulse is presented.

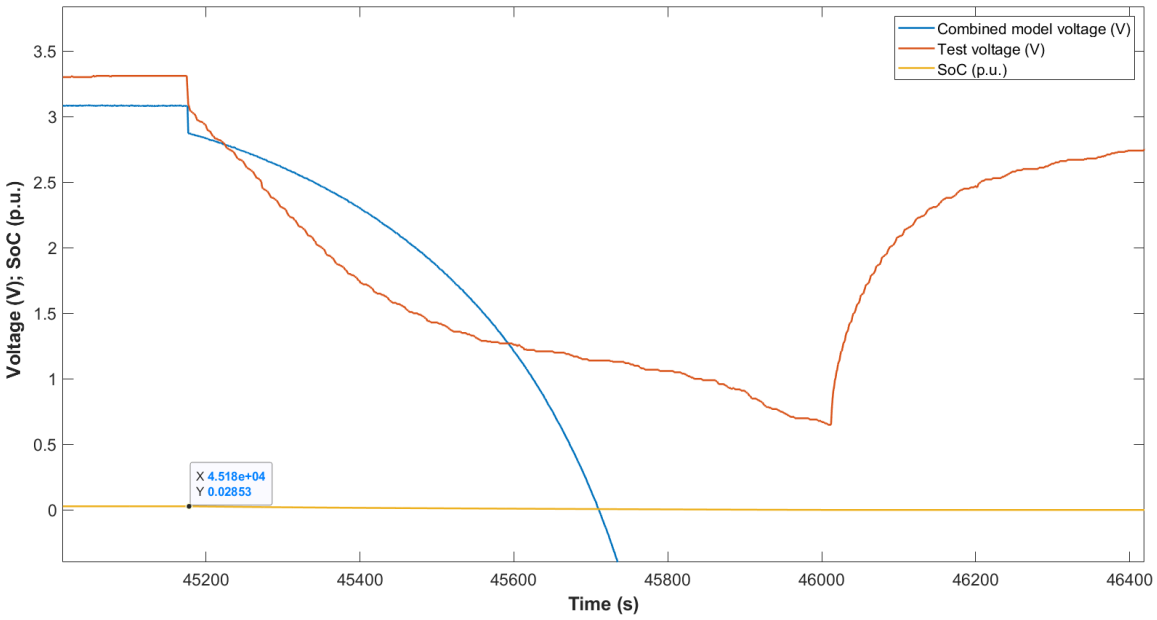

Figure 23. Combined model simulation discharging pulse

When the SoC is lower than 2.85%, the simulated voltage drastically drops being unable to follow the test data. If we analyse the resultant parameter values of the simulation and the contribution of each term of Equation 17 to the terminal voltage, it is possible to identify that the only terms that introduce a negative voltage are $-R_0 i_k$ and $-\frac{K_1}{z_k}$. The first term is function of the discharging current, that in this part of the test is low (around 0.6 A), so its influence is relatively low. On the contrary, the second term (third of Equation 17) is which governs the model result, as it has the SoC (z_k) in the denominator, so the term increases as soon as the SoC decreases.

6.4. Model validation and comparison

In this section, a comparative analysis of the three battery models results is addressed. The last two pulses have been removed from the error analysis, as it is a not-desirable level of SoC and the combined model is not able to reproduce it, making the absolute and relative error out of scale and consequently, the comparison between models, not fair.

First of all, the three simulated voltages have been represented together in Figure 24, as well as the test measured voltage, in order to better make a first visual comparison between them.

Analysing Figure 24, the combined model is the one which better reproduces the first pulse of the test, while the other two models present a slower response and an error of 0.2 V with respect to the test. Moving forward, along the charging period, the combined model is again the closest to the test data. However, during the discharge period, it seems like the simple and zero-hysteresis models are more accurate in reproducing the test than the combined model.

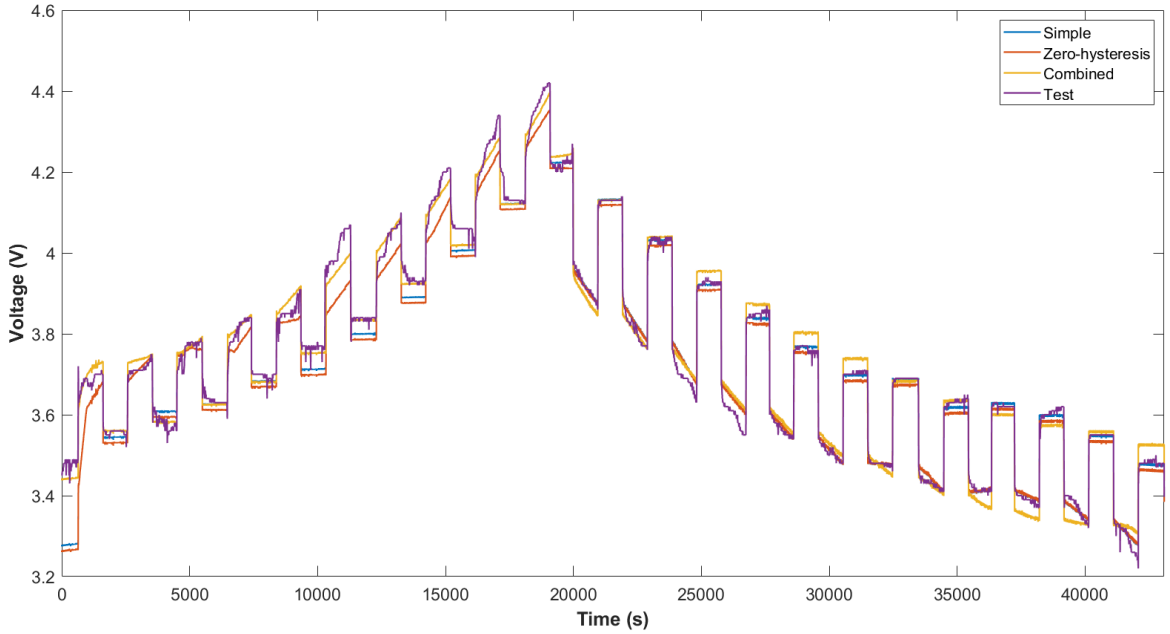

Figure 24. Comparison of test voltage curve and simulated voltage curves

In order to compare the results of the terminal voltage of the battery, the efficiency is now calculated for the test data and also the models. The efficiency of a battery is not a trivial concept, and there exist different expressions in the literature for evaluating it. Here, the 'energy efficiency' is calculated, and is given by:

$$\eta_i = \frac{E_{i,discharge}}{E_{i,charge}} = \frac{\int V_{i,discharge} \cdot I_{discharge}}{\int V_{i,charge} \cdot I_{charge}} \tag{25}$$

Where i represents the case study (test, simple model, zero-hysteresis model, combined model). The results of the application of Equation 25 to the test and models are presented in Table 12.

Table 12. Energy Efficiency of the different case studies

Case Study	Energy Efficiency (%)
Test	89.836
Simple Model	91.279
Zero-hysteresis Model	91.278
Combined Model	89.989

The energy efficiency obtained from the test is 89.8 %. This value is reasonably similar to normal Li-ion batteries energy efficiency, as seen in Table 1. Analysing the efficiency from the simulations, it is verified that the combined model is the closest one to the real data (89.9 %) and that the simple and zero-hysteresis models provide practically the same result.

Secondly, Figure 25 represents the difference between the voltage data from the test and the simulated voltage of the different models, in other words:

$$error\ curve_{model_i} = voltage_{test} - voltage_{model_i} \quad (26)$$

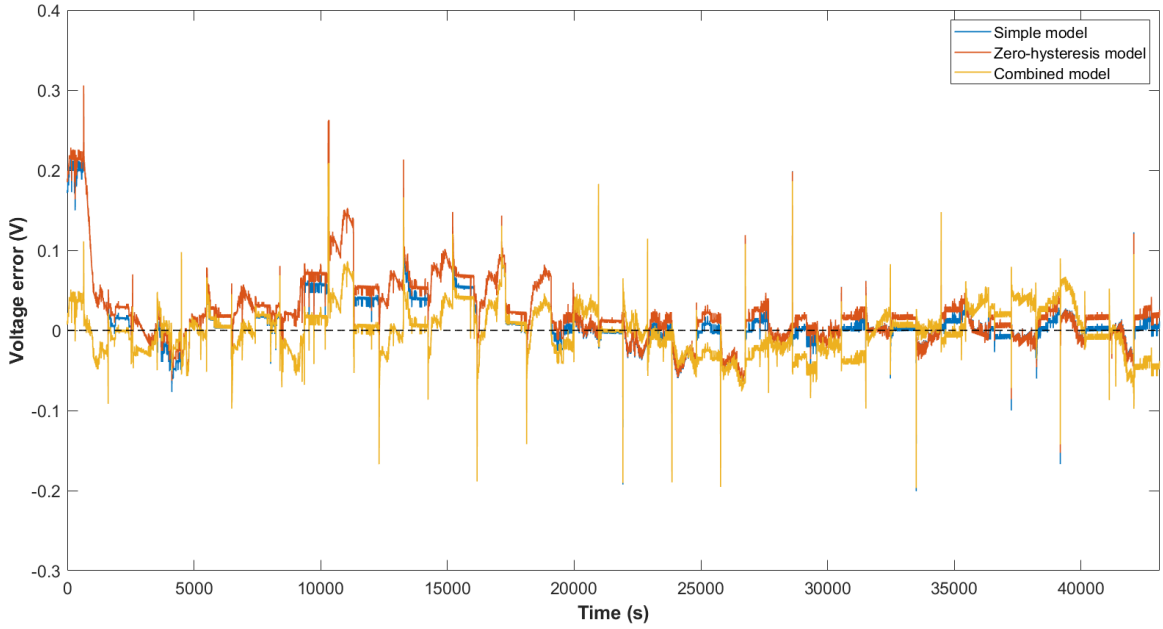

Figure 25. Simulated error curves

In the last figure, it is possible to identify where the models reproduce better the test data and where they don't. The first observation of these graph comes from the regular peaks of error of around 0.10 – 0.20 V all along with the test. These peaks correspond to the existent delay between the pulse start and the model response. To better reflect this fact, in Figure 26 a certain pulse has been isolated. The gap between test and simulation has been shadowed in the figure.

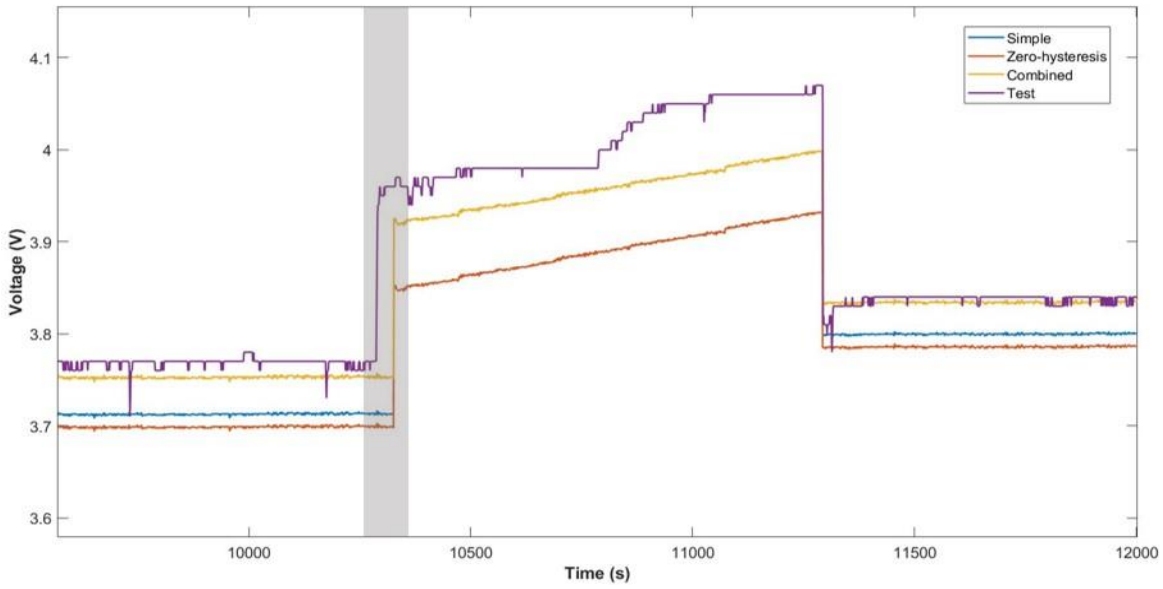

Figure 26. Simulated charging pulse

The observation of the results confirms that the simple model and the zero-hysteresis model provide a very similar voltage curve and that these two models behave contrarily to the combined model: when the combined model presents a low error with respect to the test, the other two models present considerable error; when the combined model is far from the test data, the simple and zero-hysteresis models are more accurate.

In order to numerically quantify the accuracy of the models, the Root-Mean-Squared Error (RMSE) of the resultant simulated voltage is calculated. The RMSE provides an averaged error with the same scale of the data, that is, volts, and the square root smooths the peaks of the error caused by noise in the measurement. The expression of RMSE is:

$$RMSE_{model_i} = \sqrt{\frac{1}{N}\sum_{j=1}^{N}\left(voltage_{test_j} - voltage_{model_{i_j}}\right)^2} \tag{27}$$

Being *N* the number of measured data. The results are gathered in Table 13**.**

Table 13. RMS of the simulated models

Model	RMSE
Simple	0.2150 V
Zero-hysteresis	0.2228 V
Combined	0.1879 V

Once again, it is verified that the combined model is the one with the lower averaged error with respect to the test, that is 0.1879 V. After it, the simple model presents an averaged error of 0.2150 V, very close to the error of the zero-hysteresis model with 0.2228 V.

7. Project summary

In this section, the project is evaluated with respect to its dedication time and cost of research and development, as well as to its associated environmental impact.

7.1. Timeline

This project started on the 4th of March of 2019, and its being delivered on the 16th of September of 2019, accounting a total of 197 days since its start. As a Master Thesis, the theoretical time of dedication to its development is estimated to be between 750 – 900 hours. This means that the average time spent per day between 3.80 and 4.57 hours/day. The Gantt char of the project is presented in Figure 27.

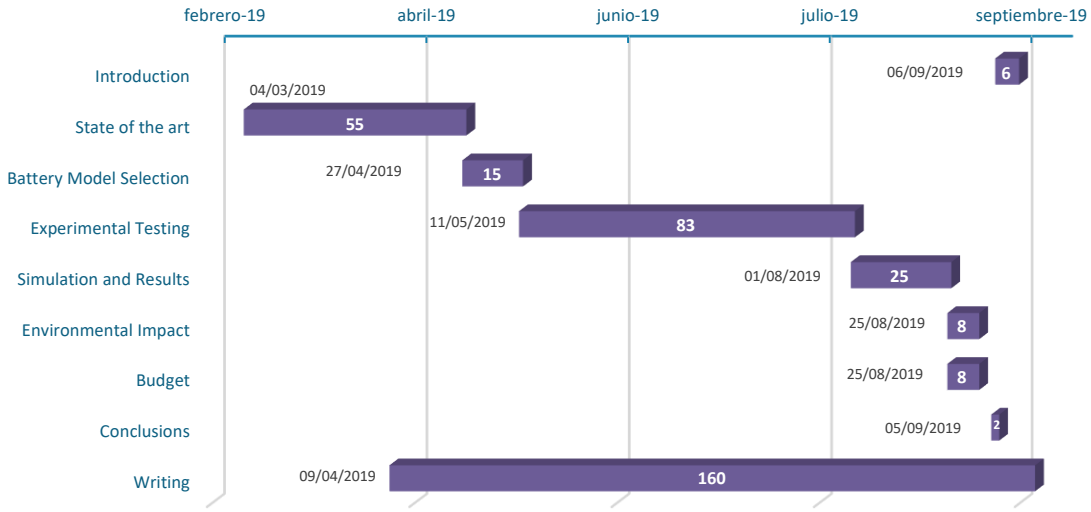

Figure 27. Grantt Char of the thesis

7.2. Budget estimation

The remuneration selected to estimate the cost of the thesis is 9 €/h. It is assumed that the total hours spent in the project is 800 hours. The breakdown of the different phases is resumed in Table 14.

Table 14. Thesis development cost

Phase	Hours	Remuneration
Literature review	168	1512 €
Experimental testing	184	1656 €
Simulation	55	495 €
Writing	393	3537 €
Total	**800**	**7200 €**

7.3. Environmental impact

As this project is focused on secondary batteries from a research and simulation point of view, the environmental impact of the project only considers the development of the thesis itself, because no real application is involved.

The first aspect to be analysed is the consumption of electricity required to perform the experimental test and also the electricity used to charge the laptop:

- The experimental test lasted 48000 seconds, which is, 13.3 h. However, in order to reach the final configuration of the electric circuit and the ultimate test, several days of tries were also necessary. The estimated hours of electricity used for experimental testing are 30 h. Considering the power of the controllable source used in the test:

$$E_{test} = 150W \cdot 30\ h = 4500\ Wh = 4.5\ kWh$$

- The laptop has been used practically during the whole project development. Every phase has required consults on the Internet, writing, calculations… So considering the 65 W of the laptop charger, and assuming that half of the time of use the laptop has been plugged and half unplugged:

$$E_{laptop} = 65W \cdot 169\ h = 10985\ Wh = 10.985\ kWh$$

Secondly, the majority of time spent in the thesis development has occurred in the Electrical Engineering Department of the University (let is assume 70%). During this time, the AC unit and lights were always ON, which has an associated energy consumption that can be estimated as:

$$E_{lighting} = 36\ lightpoints \cdot 18\frac{W}{lightpoint} \cdot 0.7 \cdot 338\ h = 153316.8\ Wh = 153.32\ kWh$$

$$E_{AC} = 125W \cdot 0.7 \cdot 338\ hours = 29575\ Wh = 29.575\ kWh$$

In order to estimate the environmental impact of all the previous energy consumptions, the '*Guia Pràctica per al càlcul d'emissions de gasos amb effecte d'hivernacle'* [33] of the Catalan Government has been consulted, from where a conversion coefficient of 0.321 $kgCO_2/kWh$ of electricity has been adopted. The environmental impact is resumed in Table 15.

Table 15. Thesis environmental impact

Energy Consumer	Energy (kWh)	Emissions ($kgCO_{2eq}$)
Experimental testing	4.50	1.445
Laptop	10.99	3.526
Lighting	153.32	49.216
AC	29.58	9.494
Total	**198.38**	**63.681**

8. Conclusions

The main goal of this project has been fulfilled. From a deep literature review of secondary batteries, the necessary knowledge has been acquired to address the study of different battery models and SoC estimators, its implementation and simulation, and finally the comparison between them, analysing and validating the results. Furthermore, a hardware platform has been built in order to perform experimental tests with secondary batteries, using Arduino for data acquisition. This objective has been also reached. And what is more, the current platform has the potential to be upgraded in future steps with automatic control algorithms to provide a more accurate, autonomous data.

A charging-discharging test of a 4.2 V (maximum voltage) Li-ion battery has been conducted. The procedure used was the application of a stepped current signal of 1 A during battery charging, and the connection of the battery to a 4 Ω resistor during battery discharging. The current pulses have been distributed with relaxation periods of 0 A in order to let the cell voltage stabilise. Evaluating the test result, the energy efficiency of the battery, in other words, the delivered energy during discharge in relation with the energy needed to charge the battery, results 89.836 %, a value slightly below the expected for a Li-ion battery, but close enough to the normal range considering the experiment's boundary conditions.

After the collection and treatment of test data, three battery models have been implemented in Matlab-Simulink: the simple model, the zero-hysteresis model and the combined model. These three models are no more than three different ways to adjust the voltage curve of the battery. The Least-Squares Estimation has been used as offline method for the identification of the model parameters in all the cases.

The simple model simulation has provided a voltage curve that reproduces better the discharging phase than the charging one. It presents a slow response in the first pulse of the simulation, and the simulated voltage is always below the test voltage during pulses. Its validation reports a battery energy efficiency of 91.279 % with an RMSE of 0.215 V.

The zero-hysteresis model introduces the hysteresis effect in the voltage estimation. The simulation of this model provides a very similar result than the simple model, with an energy efficiency of 91.278 % and an RMSE of 0.222 V. The energy efficiency is practically the same than the simple model simulation, while it presents a lightly larger averaged error.

The combined model results to be the one which better reproduces the experimental data. However, this is only true if the two last pulses of the test are not considered. During these pulses, where the battery voltage drops significantly, the combined model is not able to adjust its voltage curve. In the rest of the experiment, the combined model provides a considerably accurate curve with respect to the test, whit an energy efficiency of 89.989 % and an RMSE of 0.188 V.

The tendency of the simulations suggests that the higher the error, the higher is also the energy efficiency, which means that the battery models provide an optimistic representation of the reality.

8.1. Future steps

One of the strong points of this thesis is its potential for future extensions. As it has been described in the literature review, secondary batteries and energy storage are on the top of the research in the energy sector, so new achievements and findings appear every day. Battery models and SoC estimators are crucial in this research, as BMS as a key factor in fields like the transition to a global electric transport system, the energy storage for the residential sector or the large-scale energy storage plants for power systems. All these factors make valuable to develop a flexible methodology and a multifunctional platform that can be easily adjusted to perform many different studies.

Going to the specific topics studied here, there exist multiple battery models already discovered and tested. In this project, just three of the simplest models have been presented and simulated, but the methodology followed to solve them can be used to implement new, more accurate and complex battery models, validate their extents and their potential and compare them to extract conclusions.

Furthermore, the adjustment technique to solve the battery models and run the simulation in the cases of this thesis has been the LSE. This is just one of the multiple techniques available to identify the model parameters. For example, the first option that could be implemented is a Kalman Filter to the models presented. In the case of new battery models from the simple, combined and zero-hysteresis, other types of techniques could be applied.

Finally, other SoC estimators (see Table 2) could be also implemented in order to analyse different features of the battery, as well as deeper chemical phenomena in the cell.

The other strong point of upgrading in the future is the hardware platform built to run the test and measure the currents and voltages of the charging/discharging processes of the battery. Indeed, this point has been already addressed and a new version of the platform is under construction at the time this thesis is presented.

The main objective of the new platform is to make it able to run and carry out the same kind of test already done in the thesis, but this time in a more controlled, autonomous way. To do that, a DC-DC converter has been introduced, in order to de-couple the voltage source and the terminal voltage of the battery, and also to have the possibility to implement some automatic control on the algorithm, what is, a double PI control loop, one for the charge/discharge current and another for the voltage control. A conceptual scheme of this new platform is shown in Figure 28.

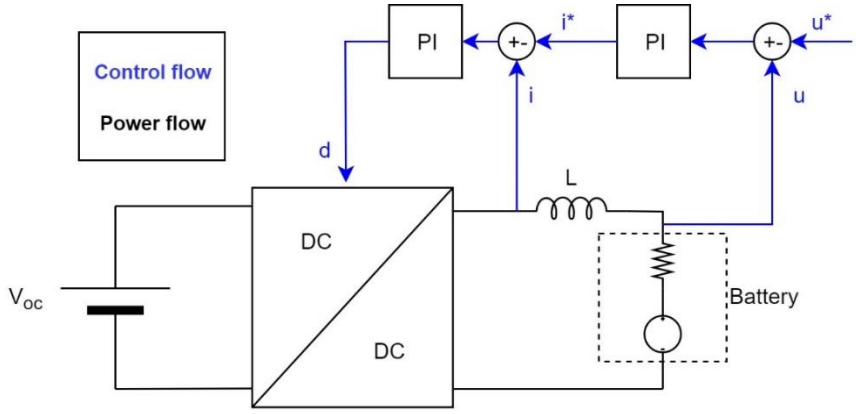

Figure 28. Diagram of the upgraded Arduino platform for testing batteries

In this new configuration, now the voltage and current measurements of the sensors are used to automatically correct the current flowing from the converter to charge/discharge the battery. The converter that is being tested is a full-bridge driver that contains some distributed transistors that allow it to Pulse-Width Modulation (PWM) the output signals of the Arduino board to adjust the current flow accordingly to the set points or reference signals. Different models of converters are being tested, as L293 Quadruple Half-H Bridge or Multiwatt11 L6203 DMOS Full Bridge Driver (Annex C. Datasheets). In Figure 29, a picture of the current state of the platform is presented.

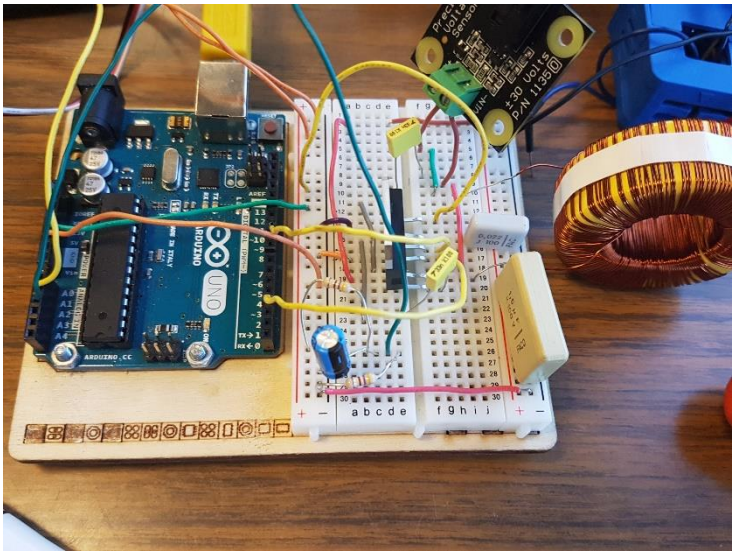

Figure 29. Real picture of the upgraded Arduino platform

Once the platform and components work properly, the experimental testing will be less demanding in terms of physical intrusion, what it is supposed to provide a more accurate, clean test data, and consequently, more faithful results.

Acknowledgements

First of all, I must thank Francisco Diaz for his advice, his patience and his readiness. This topic was completely new and a big challenge, and it couldn´t have been possible without his support and knowledge.

Secondly, I am grateful to all the CITCEA-UPC group for providing me the necessary material to perform this thesis, and for giving me a spot at the department and always be willing to help me.

To my family. Their support through my whole life is a debt that I will never be able to repay. Thank you so much for everything.

To Marina. I love you.

References

[1] 'The Keeling Curve | A daily record of atmospheric carbon dioxide from Scripps Institution of Oceanography at UC San Diego', *Scripps Institution of Oceanography at UC San Diego*, 2019. [Online]. Available: https://scripps.ucsd.edu/programs/keelingcurve/. [Accessed: 12-Sep-2019].

[2] C. McKerracher *et al.*, 'Electric Vehicle Outlook 2019 | Bloomberg NEF', 2019.

[3] L. Goldie-Scot, 'A Behind the Scenes Take on Lithium-ion Battery Prices | Bloomberg NEF', *BloombergNEF*, 2019. [Online]. Available: https://about.bnef.com/blog/behind-scenes-take-lithium-ion-battery-prices/. [Accessed: 06-Mar-2019].

[4] 'Top ten innovations 2019 - Energy Storage Highlights', *pv Mag.*, no. February, 2019.

[5] P. Cotti, 'The discovery of the electric current', 1995.

[6] B. Viswanathan, *Batteries*. 2017.

[7] A. Díaz-gonzález, Francisco Sumper and O. Gomis-Bellmunt, *Energy Storage in Power Systems*. Chichester, UK: John Wiley & Sons Ltd, 2016.

[8] B. B. Owens, P. Reale, and B. Scrosati, 'PRIMARY BATTERIES | Overview', *Encycl. Electrochem. Power Sources*, pp. 22–27, Jan. 2009.

[9] P. Kurzweil, 'Gaston Planté and his invention of the lead-acid battery - The genesis of the first practical rechargeable battery', *J. Power Sources*, vol. 195, pp. 4424–4434, 2010.

[10] T. Oshima, M. Kajita, and A. Okuno, 'Development of Sodium-Sulfur Batteries', *Int. J. Appl. Ceram. Technol.*, 2010.

[11] W.-Y. Chang, 'The State of Charge Estimating Methods for Battery: A Review', *ISRN Appl. Math.*, vol. 2013, pp. 1–7, 2013.

[12] F. Pan and Q. Wang, 'Redox species of redox flow batteries: A review', *Molecules*. 2015.

[13] M. Messaggi *et al.*, 'Analysis of flow field design on vanadium redox flow battery performance: Development of 3D computational fluid dynamic model and experimental validation', *Appl. Energy*, vol. 228, no. July, pp. 1057–1070, 2018.

[14] Y. Shi *et al.*, 'Recent development of membrane for vanadium redox flow battery applications: A review', *Appl. Energy*, vol. 238, pp. 202–224, Mar. 2019.

[15] C. Zhang, T. S. Zhao, Q. Xu, L. An, and G. Zhao, 'Effects of operating temperature on the performance of vanadium redox flow batteries', *Appl. Energy*, vol. 155, pp. 349–353, Oct. 2015.

[16] A. Khor *et al.*, 'Review of zinc-based hybrid flow batteries: From fundamentals to applications', 2018.

[17] Q. Wang, S. M. Zakeeruddin, D. Wang, I. Exnar, and M. Grätzel, 'Redox targeting of insulating electrode materials: A new approach to high-energy-density batteries', *Angew. Chemie - Int. Ed.*, 2006.

[18] I. Renewable Energy Agency, *ELECTRICITY STORAGE AND RENEWABLES: COSTS AND MARKETS TO 2030*. 2017.

[19] F. Saidani, F. X. Hutter, R.-G. Scurtu, W. Braunwarth, and J. N. Burghartz, 'Lithium-ion battery models: a comparative study and a model-based powerline communication', *Adv. Radio Sci*, vol. 15, pp. 83–91, 2017.

[20] S. Barcellona and L. Piegari, 'Lithium ion battery models and parameter identification techniques', *Energies*, vol. 10, no. 12, 2017.

[21] T. B. Reddy, 'LINDEN'S HANDBOOK OF BATTERIES'.

[22] J. F. Manwell and J. G. McGowan, 'Lead acid battery storage model for hybrid energy systems', *Sol. Energy*, 1993.

[23] C. F. Chiasserini and R. R. Rao, 'A traffic control scheme to optimize the battery pulsed discharge', 2003.

[24] M. S. Farag, 'Lithium-Ion Batteries: Modelling and State of Charge Estimation', McMaster University, 2013.

[25] G. L. Plett, 'Part 1 - Extended Kalman filtering for battery management systems of LiPB-based HEV battery packs - Background', *J. Power Sources*, vol. 134, no. 2, pp. 252–261, 2004.

[26] G. L. Plett, 'Part 2 - Extended Kalman filtering for battery management systems of LiPB-based HEV battery packs - Modeling and identification', *J. Power Sources*, 2004.

[27] G. L. Plett, 'Part 3 - Extended Kalman filtering for battery management systems of LiPB-based HEV battery packs - State and parameter estimation', *J. Power Sources*, vol. 134, no. 2, pp. 252–261, 2004.

[28] X. Hu, S. Li, and H. Peng, 'A comparative study of equivalent circuit models for Li-ion batteries', *J. Power Sources*, vol. 198, pp. 359–367, Jan. 2012.

[29] H. Rahimi-Eichi and M. Y. Chow, 'Adaptive parameter identification and State-of-Charge estimation of lithium-ion batteries', *IECON Proc. (Industrial Electron. Conf.*, pp. 4012–4017, 2012.

[30] L. Lu, X. Han, J. Li, J. Hua, and M. Ouyang, 'A review on the key issues for lithium-ion battery management in electric vehicles', *J. Power Sources*, vol. 226, pp. 272–288, 2013.

[31] J. Kalawoun, K. Biletska, F. Suard, and M. Montaru, 'From a novel classification of the battery state of charge estimators toward a conception of an ideal one', *J. Power Sources*, vol. 279, pp. 694–706, 2015.

[32] V. Srinivasan, J. W. Weidner, and J. Newman, 'Hysteresis during Cycling of Nickel Hydroxide Active Material', *J. Electrochem. Soc.*, vol. 148, no. 9, p. A969, Sep. 2001.

[33] O. C. Canvi Climàtic, 'GUIA PRÀCTICA PER AL CÀLCUL D'EMISSIONS DE GASOS AMB EFECTE D'HIVERNACLE (GEH)', Barcelona, 2019.

Annexes

A. Main global Li-ion batteries manufacturers compilation

Here, a compilation of the main lithium-ion manufacturers worldwide is attached. The information has been extracted from the '*Top-Ten Innovations 2019 – Energy storage highlights'* [4]**.**

Table 16. Global Li-ion batteries manufacturers

Company	Headquarters (country)	Distribution countries	Manufacturing battery cells	Manufacturing betteries	Manufacturing battery	Manufacturing battery inverters	Manufacturing energy	Programming energy	Manufacturing complete battery systems	EPC services for battery storage	Operation management of
ABB AG - BU Microgrids	CHE	Worldwide	no	no	no	yes	yes	yes	yes	no	no
Ads-tec Energy	DEU	EU, USA, Asia	no	yes	yes	no	yes	yes	yes	no	yes
Aggreko Microgrid and Storage Solutions	GBR	Worldwide	no	no	no	no	yes	yes	yes	yes	yes
AKASOL	DEU	Worldwide	no	yes	yes	no	yes	yes	no	no	no
ASD Automatic Storage Device	DEU	Worldwide	no	yes	yes	yes	yes	yes	yes	yes	yes
AutarcTech	DEU	Worldwide	no	no	yes	no	no	no	no	yes	no
BayWa r.e. Solar Energy Systems	DEU	DEU, AUT, CHE, POL, Scandinavia, Benelux…	no	no	no	no	no	no	no	no	no
BECK Automation	DEU	no	no	no	no	yes	yes	yes	yes	yes	
BlueSky Energy	AUT	Worldwide	no	no	yes	no	no	yes	yes	no	yes
BMZ	DEU	Worldwide	yes	yes	yes	no	no	no	no	no	no
BYD	CHN	DEU, AUT, CHE, ESP, ITA, AUS	yes	yes	yes	no	yes	yes	no	no	no
Digital Energy Solutions	DEU	DEU, AUT	no	no	no	no	no	yes	no	yes	yes
Durion	DEU		no	no	no	no	no	yes	yes	yes	yes
E3/DC	DEU	DEU, AUT,CHE	no	no	yes	yes	yes	yes	yes	no	no
Eaton	USA	EMEA, USA, LATAM, APAC	no	yes	yes	yes	yes	yes	yes	no	yes
Enerox (CellCube)	AUT	Worldwide	yes	yes	yes	no	no	no	yes	no	no
FENECON	DEU	EU	no	no	no	no	no	yes	yes	yes	no
Gustav	Klein	DEU	no	no	no	yes	no	no	no	no	no
IBC SOLAR	DEU	Worldwide except USA	no	no	no	no	no	yes	yes	yes	yes
IRIS Energy	DEU	EU, Asia, Middle East	no	no	no	yes	yes	yes	yes	yes	no
KACO new energy	DEU		no	no	no	yes	no	no	no	no	no
NEC Energy Solutions	USA	169 countries	yes	yes	yes						
Pfenning Elektroanlagen	DEU	EU	no	yes	yes	no	yes	yes	yes	yes	yes
QINOUS	DEU	Worldwide	no	no	no	yes	no	yes	yes	no	no
RCT Power	DEU	EU	no	yes	yes	yes	yes	yes	yes	no	yes
REFU Elektronik	DEU	EU, KOR, AUS	no	no	no	yes	no	no	no	no	no
RES	GBR	DEU, FRA, TUR, USA, CAN, AUS, SWE, IRL	no	no	no	no	no	yes	no	yes	yes
Rhino Energy Solutions	ZAF		no	no	no	no	no	yes	yes	yes	yes
SegenSolar	DEU	EU, Africa	no	no	no	no	no	no	no	no	no
SMA Solar Technology	DEU	Worldwide	no	no	no	yes	yes	yes	no	no	yes
Smart Power	DEU	EU	no	no	yes	no	no	yes	yes	yes	yes
SOCOMEC	FRA		no	no	no	yes	no	yes	yes	no	no
SOLARWATT	DEU	DEU, FRA, NDL, ITA, ESP, AUS, UK, CHE, AUT, CZE, DNK	no	yes	yes	yes	yes	yes	yes	no	no
Sungrow-Samsung SDI Energy Storage Power Co.	CHN	Worldwide	no	yes	yes	yes	yes	yes	yes	yes	no
TESVOLT	DEU	Worldwide	no	no	yes	no	no	no	no	yes	yes
The Mobility House	DEU	NLD, FRA, USA	no	no	no	no	yes	yes	no	yes	yes
VARTA Storage	DEU	DEU, AUT, CHE	no	yes	yes	yes	yes	yes	yes	no	yes
Vattenfall	SWE	DEU, DNK, FRA, NLD, SWE, UK	no	no	no	no	no	no	no	yes	yes
VENSYS Elektrotechnik	DEU	Worldwide	no	yes	yes	yes	yes	yes	yes	no	no
WEMAG	DEU	EU	no	no	no	no	no	yes	yes	yes	yes
Xelectrix Power	AUT	Worldwide	no	yes	yes	yes	yes	yes	yes	yes	yes

B. Codes

B.1. Arduino code for test data acquisition

```
float sens_v = 0.0669; // Voltage sensor +-30V sensitivity
float sens_i = 0.135; // Current sensor 5A sensitivity


void setup() {

  Serial.begin(9600); // Opening serial port

}

void loop() {

  float t = millis();
  float V = get_voltageSensor(5000); // Function to obtain averaged voltage
  float I = get_corriente (500); // Function to obtain averaged current


  Serial.print(t);
  Serial.print(",");
  Serial.print(V);
  Serial.print(",");
  Serial.println(I);

  delay(1);
}


float get_corriente(int n_muestras) // Function to obtain averaged current
{
  float voltajeSensor_i;
  float corriente = 0;
  for (int i = 0; i < n_muestras; i++)
  {
    voltajeSensor_i = analogRead(A1) * (5.0 / 1023.0);
    corriente = corriente + (voltajeSensor_i - 2.499) / sens_i;
  }
  corriente = corriente / n_muestras;
  return (corriente);
}


float get_voltageSensor(int n_muestras) // Function to obtain averaged voltage
{
  float voltageSensor = 0;
  float voltageRead = 0;

  for (int i = 0; i < n_muestras; i++)
  {
    voltageRead = analogRead(A0) * (5.0 / 1023.0);
    voltageSensor = voltageSensor + ((voltageRead - 2.51) / sens_v);
  }
  voltageSensor = voltageSensor / n_muestras;
  return (voltageSensor);
}
```

B.2. MATLAB code for serial port communication with Arduino

```
%% Matlab-Arduino communication
% Author: Alejandro Zaragoza
% Master Thesis: Modelling of secondary batteries for SOC estimation

%% Code
close all;clear all;
clc;

t=zeros(1,1);
V=zeros(1,1);
I=zeros(1,1);

%Serial port initialisation
delete(instrfind({'Port'},{'COM8'}));
puerto_serial=serial('COM8','BaudRate',9600,'Terminator','CR/LF');
warning('off','MATLAB:serial:fscanf:unsuccessfulRead');

%Serial port opening
fopen(puerto_serial);

%Counter declearing
contador_muestras=1;
numero_muestras = 6000;

%Creation of a figure window
figure('Name','Serial communication: Matlab + Arduino. Alejandro Zaragoza')
title('SERIAL COMMUNICATION MATLAB+ARDUINO');
grid on;
hold on;

%Button to manually stop the test reading
ButtonHandle = uicontrol('Style', 'PushButton', ...
                         'String', 'Stop loop', ...
                         'Callback', 'delete(gcbf)');

%Reading and plotting loop
while contador_muestras<=numero_muestras


        a=fscanf(puerto_serial,'%f,%f,%f')';
        t(contador_muestras)=a(1);
        V(contador_muestras)=a(2);
        I(contador_muestras)=a(3);

        subplot(2,1,1);
        plot(contador_muestras,V(contador_muestras),'+-b');
        hold on;
        xlim([contador_muestras-300 contador_muestras+50]);

        subplot(2,1,2);
        plot(contador_muestras,I(contador_muestras),'x-g');
        hold on;
        xlim([contador_muestras-300 contador_muestras+50]);

        drawnow limitrate
        contador_muestras=contador_muestras+1;

        if ~ishandle(ButtonHandle)
            break;
        end
        pause(0.01);
end
drawnow
```

```
time=t./1000;

%Final plotitng
figure
plot(time,V,'r','LineWidth',1.2)
xlabel('Time (s)');ylabel('Voltage (V)');title('Charging Voltage');
ylim([0 4.5]);
figure
plot(time,I,'b','LineWidth',1.2)
xlabel('Time (s)');ylabel('Current (I)');title('Charging Current');
```

B.3. MATLAB code for data treatment, model simulation and SoC estimation

```
%% Battery modelling and SoC estimation
% Authors: Francisco Diaz / Alejandro Zaragoza
% Master Thesis: Modelling of secondary batteries for SOC estimation

%% INITIALIZATION
clear all;
close all;
clc;

%% INPUT DATA

% Reading test data

load Combined_Test.mat

current = totalI';
voltage = totalV';
soc = totalsoc';

for i=1:1:length(totalI)
    time(i,1) = i;
end

%%
% Treating it

    % Obtaining the data for pulsed charging and discharging current
    sample = 1;
    epsilon = 0.1;  % This is for obtaining the sign of current. Should be
                    % sufficiently small. See (Plett 2004(b)), page 268.

    discharge_current_sample = zeros(ceil(size(current,1)/sample),1);
    charge_current_sample = zeros(ceil(size(current,1)/sample),1);
    current_sample = zeros(ceil(size(current,1)/sample),1);
    voltage_sample = zeros(ceil(size(current,1)/sample),1);
    soc_sample = zeros(ceil(size(current,1)/sample),1);
    time_sample = zeros(ceil(size(current,1)/sample),1);
    sk_sample = zeros(ceil(size(current,1)/sample),1);
    ocv_sample = zeros(ceil(size(current,1)/sample),1);

    j = 1;
    for i=1:sample:size(current,1)
        if current(i,1) >= 0
            discharge_current_sample(j,1) = current(i,1);
            charge_current_sample(j,1) = 0;
        else
            charge_current_sample(j,1) = current(i,1);
            discharge_current_sample(j,1) = 0;
        end
```

```
        voltage_sample(j,1) = voltage(i,1);
        soc_sample(j,1) = soc(i,1);
        time_sample(j,1) = time(i,1);
        j = j + 1;
    end

    % Obtaining the sign of the current with some memory (zero-state
    % hysteresis model)
    if current(1,1) > epsilon
        sk_sample(1,1) = 1;
    else
        sk_sample(1,1) = -1;
    end

    j = 2;

    for i=(sample+1):sample:size(current,1)
        if current(i,1) > epsilon
            sk_sample(j,1) = 1;
        elseif current(i,1) < -epsilon
            sk_sample(j,1) = -1;
        else
            sk_sample(j,1) = sk_sample(j-1,1);
        end
        j = j + 1;
    end

    % Obtaining the OCV profiles
    sample_ocv = floor(size(current,1)/25); % 25 points to measure OCV in the data
    time_ocv = zeros(floor(size(current,1)/sample_ocv),1);
    ocv_ocv = zeros(floor(size(current,1)/sample_ocv),1);
    soc_ocv = zeros(floor(size(current,1)/sample_ocv),1);

    j = 1;
    for i=1:sample_ocv:size(current,1)
        ocv_sample(i,1) = voltage(i,1);
        time_ocv(j,1) = time(i,1);
        ocv_ocv(j,1) = voltage(i,1);
        soc_ocv(j,1) = soc(i,1);
        j = j + 1;
    end

    ocv_sample = interp1(time_ocv,ocv_ocv,time_sample,'pchip');

% Plotting it (2/2)
figure
plot(time_sample,discharge_current_sample,time_sample,charge_current_sample,time_sa
mple,soc_sample,time_sample,voltage_sample)
xlabel('Time (s)'); ylabel('Voltage (V); Current (A); SoC (p.u.)')
ax = gca;
ax.XRuler.Exponent = 0;
ylim([-1.5 4.5]);
xlim([0 length(time)]);
legend('Discharge current (A)','Charge current (A)','SoC (p.u.)','Voltage (V)')
figure
plot(time_ocv,ocv_ocv)
xlabel('Time (s)'); ylabel('OCV (V)')
ax = gca;
ax.XRuler.Exponent = 0;
figure
plot(time_ocv,ocv_ocv,time_sample,ocv_sample)
xlabel('Time (s)'); ylabel('Voltage (V)')
ax = gca;
ax.XRuler.Exponent = 0;
title('Open circuit voltage')
```

```
legend('Test (rough) data','Sampled data for least-squared estimation')
figure
plot(soc_ocv(1:25),ocv_ocv(1:25))
xlabel('State-of-charge (p.u.)'); ylabel('Open circuit voltage (V)')
ax = gca;
ax.XRuler.Exponent = 0;
title('OCV(SoC) characteristic')

ocv_ocv(25)=ocv_ocv(26);
soc_ocv_lookuptable = flipud(soc_ocv);    % For simulation
ocv_ocv_lookuptable = flipud(ocv_ocv);    % For simulation
figure
plot(soc_ocv_lookuptable(1:16),ocv_ocv_lookuptable(1:16))
xlabel('State-of-charge (p.u.)'); ylabel('Open circuit voltage (V)')
ax = gca;
ax.XRuler.Exponent = 0;
title('OCV(SoC) characteristic for simulation')


voltage_samp = voltage_sample(1:42561);
discharge_current_samp = discharge_current_sample(1:42561);
charge_current_samp = charge_current_sample(1:42561);
soc_samp = soc_sample(1:42561);
ocv_samp = ocv_sample(1:42561);
sk_samp = sk_sample(1:42561);

% Battery efficiency
P_cha = voltage_sample(1:1:19540).*charge_current_sample(1:1:19540);
P_dis = voltage_sample(19540:1:43544).*discharge_current_sample(19540:1:43544);
E_cha = trapz(abs(P_cha));
E_dis = trapz(abs(P_dis));
eta_bat = E_dis/E_cha;


%% LEAST-SQUARED ESTIMATION
% For simple model BETA = [R+, R-]
Y_simple_model = [voltage_samp-ocv_samp];
X_simple_model = [discharge_current_samp, charge_current_samp];
BETA_simple_model = pinv(X_simple_model)*Y_simple_model;

% For combined model BETA = [k0, R+, R-, k1, k2, k3, k4]
Y_combined_model = voltage_samp;
X_combined_model = [ones(size(discharge_current_samp,1),1), -
discharge_current_samp, -charge_current_samp, -
(ones(size(discharge_current_samp,1),1))./soc_samp, -soc_samp, log(soc_samp),
log(1-soc_samp)];
BETA_combined_model = pinv(X_combined_model)*Y_combined_model;

% For zero-state hysteresis model = [R+, R-, M]
Y_zero_hysteresis_model = [voltage_samp - ocv_samp];
X_zero_hysteresis_model = [discharge_current_samp, charge_current_samp, sk_samp];
BETA_zero_hysteresis_model = pinv(X_zero_hysteresis_model)*Y_zero_hysteresis_model;

%% SIMPLE MODEL PARAMETERS

Delta_t = 1;                % Simulation time step
current_setpoint = timeseries(current,time);
voltage_real = timeseries(voltage,time);
Simulation_time = current_setpoint.time(size(current_setpoint.time,1)-1);
C_n = 10503.55; % [As]
eta = 1;                          % Coulombic efficiency
R_di_simple = -BETA_simple_model(1);    % Discharge efficiency, Ohm
R_ch_simple = -BETA_simple_model(2);    % Charge efficiency, Ohm

%% ZERO HYSTERESIS MODEL PARAMETERS
```

```
Delta_t = 1;                % Simulation time step
current_setpoint = timeseries(current,time);
voltage_real = timeseries(voltage,time);
Simulation_time = current_setpoint.time(size(current_setpoint.time,1)-1);
C_n = 10503.55; % [As]
eta = 1;                        % Coulombic efficiency
R_di_zero = -BETA_zero_hysteresis_model(1);    % Discharge efficiency, Ohm
R_ch_zero = -BETA_zero_hysteresis_model(2);    % Charge efficiency, Ohm
M_zero = -BETA_zero_hysteresis_model(3);

%% COMBINED MODEL PARAMETERS

Delta_t = 1;                % Simulation time step
current_setpoint = timeseries(current,time);
voltage_real = timeseries(voltage,time);
Simulation_time = current_setpoint.time(size(current_setpoint.time,1));
C_n = 10503.55; % [As]
eta = 1;                        % Coulombic efficiency
K0_combined = BETA_combined_model(1);
R_di_combined = BETA_combined_model(2);    % Discharge efficiency, Ohm
R_ch_combined = BETA_combined_model(3);    % Charge efficiency, Ohm
K1_combined = BETA_combined_model(4);
K2_combined = BETA_combined_model(5);
K3_combined = BETA_combined_model(6);
K4_combined = BETA_combined_model(7);

%% SIMULATION AND RESULTS

sim('battery_v1.slx');

y_simple = y_k_simple.Data(1:47981);
y_zero = y_k_zero.Data(1:47981);
y_combined = y_k_combined.Data(1:47981);

% Simulated Battery Efficiency
P_cha_simple = y_simple(1:1:19540).*charge_current_sample(1:1:19540);
P_dis_simple = y_simple(19540:1:43544).*discharge_current_sample(19540:1:43544);
E_cha_simple = trapz(abs(P_cha_simple));
E_dis_simple = trapz(abs(P_dis_simple));
eta_simple = E_dis_simple/E_cha_simple;

P_cha_zero = y_zero(1:1:19540).*charge_current_sample(1:1:19540);
P_dis_zero = y_zero(19540:1:43544).*discharge_current_sample(19540:1:43544);
E_cha_zero = trapz(abs(P_cha_zero));
E_dis_zero = trapz(abs(P_dis_zero));
eta_zero = E_dis_zero/E_cha_zero;

P_cha_comb = y_combined(1:1:19540).*charge_current_sample(1:1:19540);
P_dis_comb = y_combined(19540:1:43544).*discharge_current_sample(19540:1:43544);
E_cha_comb = trapz(abs(P_cha_comb));
E_dis_comb = trapz(abs(P_dis_comb));
eta_comb = E_dis_comb/E_cha_comb;

figure
plot(time_sample,y_simple,time_sample,voltage_sample)
xlabel('Time (s)');ylabel('Voltage (V)');
ax = gca;
ax.XRuler.Exponent = 0;
xlim([0 length(time)]);
legend('Simple model','Test')

figure
plot(time_sample,y_zero,time_sample,voltage_sample)
xlabel('Time (s)');ylabel('Voltage (V)');
```

```
ax = gca;
ax.XRuler.Exponent = 0;
xlim([0 length(time)]);
legend('Zero-hysteresis model','Test')

figure
plot(time_sample,y_combined,time_sample,voltage_sample,
time_sample,soc_sample,time_sample,current_sample)
xlabel('Time (s)');ylabel('Voltage (V)');
ax = gca;
ax.XRuler.Exponent = 0;
xlim([0 length(time)]);
legend('Combined model voltage (V)','Test voltage (V)','SoC','Current (A)')

figure
plot(RESULTS_SIMPLE_MODEL.time(:,1),RESULTS_SIMPLE_MODEL.signals.values(:,1),RESULT
S_ZERO_MODEL.time(:,1),RESULTS_ZERO_MODEL.signals.values(:,1),RESULTS_COMBINED_MODE
L.time(1:1:45710,1),RESULTS_COMBINED_MODEL.signals.values(1:1:45710,1),RESULTS_SIMP
LE_MODEL.time(:,1),RESULTS_SIMPLE_MODEL.signals.values(:,2))
xlabel('Time (s)'); ylabel('Voltage (V)')
xlim([0 43087]);
ax = gca;
ax.XRuler.Exponent = 0;
legend('Simple','Zero-hysteresis','Combined','Test')

%% Error analysis
err_simple_curve = voltage_sample-y_simple;
err_zero_curve = voltage_sample-y_zero;
err_combined_curve = voltage_sample-y_combined;

for j=1:43087
    nul(i)=0;
end

figure
plot(err_simple_curve(1:43087))
hold on
plot(err_zero_curve(1:43087))
hold on
plot(err_combined_curve(1:43087))
hold on
plot(nul,'r--')
xlim([0 43100]);
ylabel('Voltage error (V)');
xlabel('Time (s)');
ax = gca;
ax.XRuler.Exponent = 0;
legend('Simple model','Zero-hysteresis model','Combined model');

MSE_SIMPLE_MODEL = rms(RESULTS_SIMPLE_MODEL.signals.values(1:1:43544,1)-
RESULTS_SIMPLE_MODEL.signals.values(1:1:43544,2));
MSE_ZERO_MODEL = rms(RESULTS_ZERO_MODEL.signals.values(1:1:43544,1)-
RESULTS_ZERO_MODEL.signals.values(1:1:43544,2));
MSE_COMBINED_MODEL = rms(RESULTS_COMBINED_MODEL.signals.values(1:1:43544,1)-
RESULTS_COMBINED_MODEL.signals.values(1:1:43544,3));

RMSE_SIMPLE_MODEL = sqrt(MSE_SIMPLE_MODEL);
RMSE_ZERO_MODEL = sqrt(MSE_ZERO_MODEL);
RMSE_COMBINED_MODEL = sqrt(MSE_COMBINED_MODEL);
```

B.4. MATLAB code for battery models functions

- Simple battery model:

```
function [z_k_plus_1,y_k] =
fcn(i_k,z_k,R_di,R_ch,soc_ocv_lookuptable,ocv_ocv_lookuptable,eta,Delta_t,C_n)

if i_k > 0
    y_k = interp1(soc_ocv_lookuptable,ocv_ocv_lookuptable,z_k,'linear','extrap') -
R_di * i_k;
else
    y_k = interp1(soc_ocv_lookuptable,ocv_ocv_lookuptable,z_k,'linear','extrap') -
R_ch * i_k;
end

z_k_plus_1 = z_k - ( eta * Delta_t / C_n ) * i_k;
```

- Zero-hysteresis battery model:

```
function [z_k_plus_1,y_k,s_k] =
fcn(i_k,z_k,s_k_minus_1,R_di,R_ch,M,epsilon,soc_ocv_lookuptable,ocv_ocv_lookuptable
,eta,Delta_t,C_n)

if i_k > epsilon
    s_k = 1;
elseif i_k < epsilon
    s_k = -1;
else
    s_k = s_k_minus_1;
end

if i_k > 0
    y_k = interp1(soc_ocv_lookuptable,ocv_ocv_lookuptable,z_k,'linear','extrap') -
R_di * i_k - M * s_k;
else
    y_k = interp1(soc_ocv_lookuptable,ocv_ocv_lookuptable,z_k,'linear','extrap') -
R_ch * i_k - M * s_k;
end

z_k_plus_1 = z_k - ( eta * Delta_t / C_n ) * i_k;
```

- Combined model:

```
function [z_k_plus_1,y_k] = fcn(i_k,z_k,K0,R_di,R_ch,K1,K2,K3,K4,eta,Delta_t,C_n)


if i_k > 0
    y_k = K0 - R_di * i_k - K1/z_k - K2 * z_k + K3 * log(z_k) + K4 * log( 1 - z_k
);
else
    y_k = K0 - R_ch * i_k - K1/z_k - K2 * z_k + K3 * log(z_k) + K4 * log( 1 - z_k
);
end

z_k_plus_1 = z_k - ( eta * Delta_t / C_n ) * i_k;
```

C. Datasheets

C.1. Arduino UNO

C.2. Li-ion battery

C.3. Inductor

C.4. Voltage sensor

C.5. Current sensor

C.6. Controllable source

C.7. Multiwatt 11 L6203 Bridge

Arduino Uno

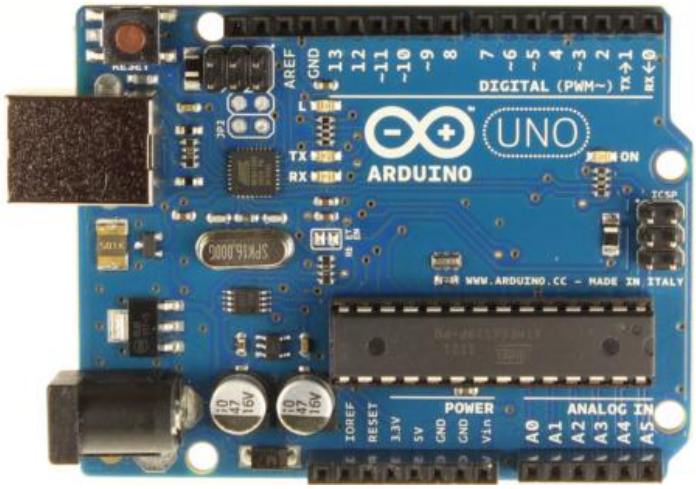

Arduino Uno R3 Front

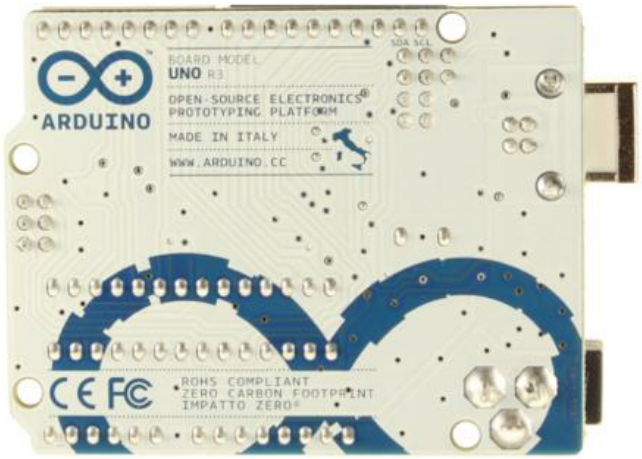

Arduino Uno R3 Back

Arduino Uno R2 Front

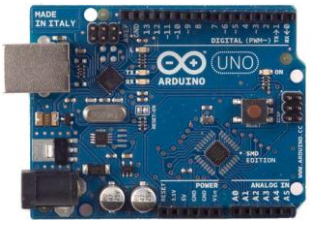

Arduino Uno SMD

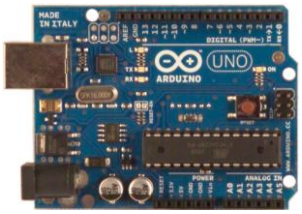

Arduino Uno Front

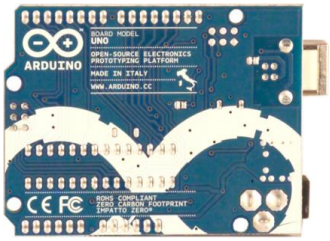

Arduino Uno Back

Overview

The Arduino Uno is a microcontroller board based on the ATmega328 (datasheet). It has 14 digital input/output pins (of which 6 can be used as PWM outputs), 6 analog inputs, a 16 MHz ceramic resonator, a USB connection, a power jack, an ICSP header, and a reset button. It contains everything needed to support the microcontroller; simply connect it to a computer with a USB cable or power it with a AC-to-DC adapter or battery to get started.
The Uno differs from all preceding boards in that it does not use the FTDI USB-to-serial driver chip. Instead, it features the Atmega16U2 (Atmega8U2 up to version R2) programmed as a USB-to-serial converter.
Revision 2 of the Uno board has a resistor pulling the 8U2 HWB line to ground, making it easier to put into DFU mode.
Revision 3 of the board has the following new features:

- 1.0 pinout: added SDA and SCL pins that are near to the AREF pin and two other new pins placed near to the RESET pin, the IOREF that allow the shields to adapt to the voltage provided from the board. In future, shields will be compatible both with the board that use the AVR, which operate with 5V and with the Arduino Due that operate with 3.3V. The second one is a not connected pin, that is reserved for future purposes.
- Stronger RESET circuit.
- Atmega 16U2 replace the 8U2.

"Uno" means one in Italian and is named to mark the upcoming release of Arduino 1.0. The Uno and version 1.0 will be the reference versions of Arduino, moving forward. The Uno is the latest in a series of USB Arduino boards, and the reference model for the Arduino platform; for a comparison with previous versions, see the index of Arduino boards.

Summary

Microcontroller	ATmega328
Operating Voltage	5V
Input Voltage (recommended)	7-12V

Input Voltage (limits)	6-20V
Digital I/O Pins	14 (of which 6 provide PWM output)
Analog Input Pins	6
DC Current per I/O Pin	40 mA
DC Current for 3.3V Pin	50 mA
Flash Memory	32 KB (ATmega328) of which 0.5 KB used by bootloader
SRAM	2 KB (ATmega328)
EEPROM	1 KB (ATmega328)
Clock Speed	16 MHz

Schematic & Reference Design

EAGLE files: arduino-uno-Rev3-reference-design.zip (NOTE: works with Eagle 6.0 and newer)
Schematic: arduino-uno-Rev3-schematic.pdf
Note: The Arduino reference design can use an Atmega8, 168, or 328, Current models use an ATmega328, but an Atmega8 is shown in the schematic for reference. The pin configuration is identical on all three processors.

Power

The Arduino Uno can be powered via the USB connection or with an external power supply. The power source is selected automatically.
External (non-USB) power can come either from an AC-to-DC adapter (wall-wart) or battery. The adapter can be connected by plugging a 2.1mm center-positive plug into the board's power jack. Leads from a battery can be inserted in the Gnd and Vin pin headers of the POWER connector.
The board can operate on an external supply of 6 to 20 volts. If supplied with less than 7V, however, the 5V pin may supply less than five volts and the board may be unstable. If using more than 12V, the voltage regulator may overheat and damage the board. The recommended range is 7 to 12 volts.
The power pins are as follows:

- **VIN.** The input voltage to the Arduino board when it's using an external power source (as opposed to 5 volts from the USB connection or other regulated power source). You can supply voltage through this pin, or, if supplying voltage via the power jack, access it through this pin.
- **5V.**This pin outputs a regulated 5V from the regulator on the board. The board can be supplied with power either from the DC power jack (7 - 12V), the USB connector (5V), or the VIN pin of the board (7-12V). Supplying voltage via the 5V or 3.3V pins bypasses the regulator, and can damage your board. We don't advise it.
- **3V3.** A 3.3 volt supply generated by the on-board regulator. Maximum current draw is 50 mA.
- **GND.** Ground pins.

Memory

The ATmega328 has 32 KB (with 0.5 KB used for the bootloader). It also has 2 KB of SRAM and 1 KB of EEPROM (which can be read and written with the EEPROM library).

Input and Output

Each of the 14 digital pins on the Uno can be used as an input or output, using pinMode(), digitalWrite(), and digitalRead() functions. They operate at 5 volts. Each pin can provide or receive a maximum of 40 mA and has an internal pull-up resistor (disconnected by default) of 20-50 kOhms. In addition, some pins have specialized functions:

- **Serial: 0 (RX) and 1 (TX).** Used to receive (RX) and transmit (TX) TTL serial data. These pins are connected to the corresponding pins of the ATmega8U2 USB-to-TTL Serial chip.
- **External Interrupts: 2 and 3.** These pins can be configured to trigger an interrupt on a low value, a rising or falling edge, or a change in value. See the attachInterrupt() function for details.
- **PWM: 3, 5, 6, 9, 10, and 11.** Provide 8-bit PWM output with the analogWrite() function.

- **SPI: 10 (SS), 11 (MOSI), 12 (MISO), 13 (SCK).** These pins support SPI communication using the SPI library.
- **LED: 13.** There is a built-in LED connected to digital pin 13. When the pin is HIGH value, the LED is on, when the pin is LOW, it's off.

The Uno has 6 analog inputs, labeled A0 through A5, each of which provide 10 bits of resolution (i.e. 1024 different values). By default they measure from ground to 5 volts, though is it possible to change the upper end of their range using the AREF pin and the analogReference() function. Additionally, some pins have specialized functionality:

- **TWI: A4 or SDA pin and A5 or SCL pin.** Support TWI communication using the Wire library.

There are a couple of other pins on the board:

- **AREF.** Reference voltage for the analog inputs. Used with analogReference().
- **Reset.** Bring this line LOW to reset the microcontroller. Typically used to add a reset button to shields which block the one on the board.

See also the mapping between Arduino pins and ATmega328 ports. The mapping for the Atmega8, 168, and 328 is identical.

Communication

The Arduino Uno has a number of facilities for communicating with a computer, another Arduino, or other microcontrollers. The ATmega328 provides UART TTL (5V) serial communication, which is available on digital pins 0 (RX) and 1 (TX). An ATmega16U2 on the board channels this serial communication over USB and appears as a virtual com port to software on the computer. The '16U2 firmware uses the standard USB COM drivers, and no external driver is needed. However, on Windows, a .inf file is required. The Arduino software includes a serial monitor which allows simple textual data to be sent to and from the Arduino board. The RX and TX LEDs on the board will flash when data is being transmitted via the USB-to-serial chip and USB connection to the computer (but not for serial communication on pins 0 and 1).
A SoftwareSerial library allows for serial communication on any of the Uno's digital pins.
The ATmega328 also supports I2C (TWI) and SPI communication. The Arduino software includes a Wire library to simplify use of the I2C bus; see the documentation for details. For SPI communication, use the SPI library.

Programming

The Arduino Uno can be programmed with the Arduino software (download). Select "Arduino Uno from the **Tools > Board** menu (according to the microcontroller on your board). For details, see the reference and tutorials.
The ATmega328 on the Arduino Uno comes preburned with a bootloader that allows you to upload new code to it without the use of an external hardware programmer. It communicates using the original STK500 protocol (reference, C header files).
You can also bypass the bootloader and program the microcontroller through the ICSP (In-Circuit Serial Programming) header; see these instructions for details.
The ATmega16U2 (or 8U2 in the rev1 and rev2 boards) firmware source code is available . The ATmega16U2/8U2 is loaded with a DFU bootloader, which can be activated by:

- On Rev1 boards: connecting the solder jumper on the back of the board (near the map of Italy) and then resetting the 8U2.
- On Rev2 or later boards: there is a resistor that pulling the 8U2/16U2 HWB line to ground, making it easier to put into DFU mode.

You can then use Atmel's FLIP software (Windows) or the DFU programmer (Mac OS X and Linux) to load a new firmware. Or you can use the ISP header with an external programmer (overwriting the DFU bootloader). See this user-contributed tutorial for more information.

Automatic (Software) Reset

Rather than requiring a physical press of the reset button before an upload, the Arduino Uno is designed in a way that allows it to be reset by software running on a connected computer. One of the hardware flow control lines (DTR) of the ATmega8U2/16U2 is connected to the reset line of the ATmega328 via a 100 nanofarad capacitor. When this line is asserted (taken low), the reset line drops long enough to reset the chip. The Arduino software uses this capability to allow you to upload code by simply pressing the upload button in the Arduino environment. This means that the bootloader can have a shorter timeout, as the lowering of DTR can be well-coordinated with the start of the upload. This setup has other implications. When the Uno is connected to either a computer running Mac OS X or Linux, it resets each time a connection is made to it from software (via USB). For the following half-second or so, the bootloader is running on the Uno. While it is programmed to ignore malformed data (i.e. anything besides an upload of new code), it will intercept the first few bytes of data sent to the board after a connection is opened. If a sketch running on the board receives one-time configuration or other data when it first starts, make sure that the software with which it communicates waits a second after opening the connection and before sending this data.
The Uno contains a trace that can be cut to disable the auto-reset. The pads on either side of the trace can be soldered together to re-enable it. It's labeled "RESET-EN". You may also be able to disable the auto-reset by connecting a 110 ohm resistor from 5V to the reset line; see this forum thread for details.

USB Overcurrent Protection

The Arduino Uno has a resettable polyfuse that protects your computer's USB ports from shorts and overcurrent. Although most computers provide their own internal protection, the fuse provides an extra layer of protection. If more than 500 mA is applied to the USB port, the fuse will automatically break the connection until the short or overload is removed.

Physical Characteristics

The maximum length and width of the Uno PCB are 2.7 and 2.1 inches respectively, with the USB connector and power jack extending beyond the former dimension. Four screw holes allow the board to be attached to a surface or case. Note that the distance between digital pins 7 and 8 is 160 mil (0.16"), not an even multiple of the 100 mil spacing of the other pins.

Spec. No.	ICR18650-26F	Version No.	1.0

Specification of product

for Lithium-ion Rechargeable Cell

Model : ICR18650-26F

November, 2009

Samsung SDI Co.,Ltd.

Energy Business Division

Spec. No.	ICR18650-26F	Version No.	1.0

1. Scope

This product specification has been prepared to specify the rechargeable lithium-ion cell ('cell') to be supplied to the customer by Samsung SDI Co., Ltd.

2. Description and Model

2.1 Description Cell (lithium-ion rechargeable cell)

2.2 Model ICR18650-26F

3. Nominal Specifications

Item	Specification
3.1 Nominal Capacity	2600mAh (0.2C, 2.75V discharge)
3.2 Charging Voltage	4.2 ±0.05 V
3.3 Nominal Voltage	3.7V
3.4 Charging Method	CC-CV (constant voltage with limited current)
3.5 Charging Current	Standard charge: 1300mA Rapid charge : 2600mA
3.6 Charging Time	Standard charge : 3hours Rapid charge : 2.5hours
3.7 Max. Charge Current	2600mA
3.8 Max. Discharge Current	5200mA
3.9 Discharge Cut-off Voltage	2.75V
3.10 Cell Weight	47.0g max
3.11 Cell Dimension	Diameter(max.) : Φ 18.40 mm Height(max.) : 65.00 mm
3.12 Operating Temperature	Charge: 0 to 45℃ Discharge: -20 to 60℃
3.13 Storage Temperature	1 year: -20~25℃ (1*) 3 months: -20~45℃ (1*) 1 month: -20~60℃ (1*)

Note (1): If the cell is kept as ex-factory status (50% of charge),
the capacity recovery rate is more than 80%.

Spec. No.	ICR18650-26F	Version No.	1.0

5. Appearance

There shall be no such defects as scratch, rust, discoloration, leakage which may adversely affect commercial value of the cell.

6. Standard Test Conditions

6.1 Environmental Conditions

Unless otherwise specified, all tests stated in this specification are conducted at temperature 25±5℃ and humidity 65±20%.

6.2 Measuring Equipment

(1) Ammeter and Voltmeter

The ammeter and voltmeter should have an accuracy of the grade 0.5 or higher.

(2) Slide caliper

The slide caliper should have 0.01 mm scale.

(3) Impedance meter

The impedance meter with AC 1kHz should be used.

7. Characteristics

7.1 Standard Charge

This "Standard Charge" means charging the cell with charge current 1300mA and constant voltage 4.2V at 25℃ for 3hours.

7.2 Standard Discharge Capacity

The standard discharge capacity is the initial discharge capacity of the cell, which is measured with discharge current of 520mA with 2.75V cut-off at 25℃ within 1hour after the standard charge.

Standard Discharge Capacity ≥ 2550mAh

7.3 Initial internal impedance

Initial internal impedance measured at AC 1kHz after rated charge.

Initial internal impedance ≤ 100mΩ

7.4 Temperature Dependence of Discharge Capacity

Capacity comparison at each temperature, measured with discharge constant current 520mA and 2.75V cut-off with follow temperature after the standard charging at 25℃.

Charge Temperature	Discharge temperature			
25℃	-10℃	0℃	25℃	45℃
Relative Capacity	50%	70%	100%	95%

Spec. No.	ICR18650-26F	Version No.	1.0

Note: If charge temperature and discharge temperature is not the same,
the interval for temperature change is 3 hours.
Percentage as an index of the Standard discharge capacity(=2550mAh) is 100%.

7.5 Temperature Dependence of Charge Capacity

Capacity comparison at each temperature, measured with discharge constant current 520mA and 2.75V cut-off at 25℃ after the standard charge is as follow temperature.

	Charge temperature			Discharge temperature
	0℃	25℃	45℃	25℃
Relative Capacity	80%	100%	100%	

Note: If charge temperature and discharge temperature is not the same,
the interval for temperature change is 3 hours.
Percentage as an index of the Standard discharge capacity(=2550mAh) is 100%.

7.6 Charge Rate Capabilities

Discharge capacity is measured with constant current 520mA and 2.75V cut-off after the cell is charged with 4.2V as follows.

	Charge Condition		
Current	0.2C (520mA)	0.5C (1300mA)	1.0C (2600mA)
Cut-off	7h or 0.05C	3h or 0.05C	2.5h or 0.05C
Relative Capacity	100%	95%	90%

Note: Percentage as an index of the capacity at 25℃(=2550mAh) is 100%.

7.7 Discharge Rate Capabilities

Discharge capacity is measured with the various currents in under table and 2.75V cut-off after the standard charge.

	Discharge Condition			
Current	0.2C (520mA)	0.5C (1300mA)	1.0C (2600mA)	2.0C (5200mA)
Relative Capacity	100%	95%	90%	80%

Note: Percentage as an index of the capacity at 25℃(=2550mAh) is 100%.

Spec. No.	ICR18650-26F	Version No.	1.0

7.8 Cycle Life

Each cycle is an interval between the charge (charge current 1300mA) with 0.05C cut-off and the discharge (discharge current 1300mA) with 2.75V cut-off. Capacity after 299cycles and plus 1 day, measured under the same condition in 7.2

Capacity ≥ 1785mAh

7.9 Storage Characteristics

Capacity after storage for 30days at 25℃ from the standard charge, measured with discharge current 1300mA with 2.75V cut-off at 25℃.

Capacity retention(after the storage) ≥ 2040mAh

7.10 Status of the cell as of ex-factory

The cell should be shipped in 50% charged state. In this case, OCV is from 3.65V to 3.85V.

8. Mechanical Characteristics

8.1 Drop Test

Test method: Cell(as of shipment or full charged) drop onto the oak-board (thickness: ≥30mm) from 4 feet height at a random direction 6 times.

Criteria: No leakage

8.2 Vibration Test

Test method: Cell(as of shipment) is vibrated along 2 mutually perpendicular axes with total excursion of 1.6mm and with frequency cycling between 10Hz and 55Hz by 1Hz/min.

Criteria: No leakage

9. Safety

9.1 Overcharge Test

Test method: To charge the standard charged cell with 12V and 2600mA at 25℃ for 2.5 hours.

Criteria: No fire, and no explosion.

9.2 External Short-circuit Test

Test method: To short-circuit the standard charged cell by connecting positive and negative terminal by less than 50mΩ wire for 3hours.

Criteria: No fire, and no explosion.

† RoHS COMPLIANT

High Current Toroid Inductors

Features

- Low radiation
- High current capacity
- High inductance
- Increase inductance with AC excitation current to compensate reduced inductance with DC bias
- Low cost
- Operating temperature: -55 to 105 °C

† RoHS Directive 2002/95/EC Jan. 27, 2003 including annex and RoHS Recast 2011/65/EU June 8, 2011.

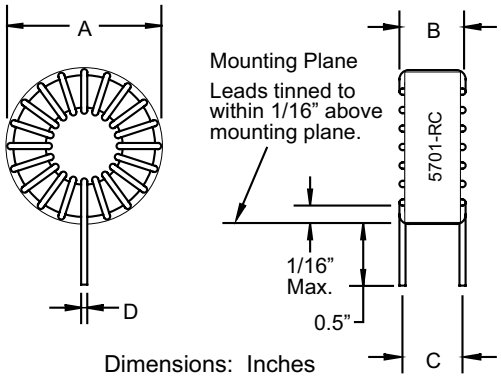

5700 Series								
Part Number	L (µH) ±15 % @ 1 KHz	I (A) Max.	L (µH) Min. @ I rated	DCR Ω Max.	Dim. A Max.	Dim. B Max.	Dim. C Nom.	Dim. D Nom.
5701-RC	10	11.00	5	0.008	0.875	0.437	0.32	0.064
5702-RC	25	5.50	12	0.014	0.875	0.437	0.30	0.040
5703-RC	125	2.75	70	0.12	0.875	0.437	0.30	0.020
5704-RC	275	2.00	150	0.24	0.875	0.437	0.30	0.016
5705-RC	450	1.50	270	0.49	0.875	0.437	0.30	0.016
5706-RC	25	9.00	15	0.012	1.125	0.562	0.45	0.064
5707-RC	75	5.00	40	0.04	1.125	0.562	0.42	0.036
5708-RC	400	2.25	225	0.33	1.125	0.562	0.42	0.018
5709-RC	800	1.75	475	0.64	1.125	0.562	0.42	0.015
5710-RC	1000	1.50	575	0.98	1.125	0.562	0.40	0.012
5711-RC	50	9.50	25	0.012	1.250	0.625	0.53	0.064
5712-RC	150	4.75	85	0.046	1.250	0.625	0.50	0.036
5713-RC	700	2.25	400	0.42	1.250	0.625	0.50	0.018
5714-RC	1250	1.75	750	0.85	1.250	0.625	0.48	0.015
5715-RC	1600	1.50	950	1.27	1.250	0.625	0.48	0.012
5716-RC	125	7.75	65	0.032	1.812	0.750	0.68	0.064
5717-RC	500	4.00	275	0.15	1.812	0.750	0.65	0.032
5718-RC	1100	2.50	650	0.33	1.812	0.750	0.65	0.025
5719-RC	2250	1.75	1350	0.92	1.812	0.750	0.65	0.018
5720-RC	4500	1.25	2700	2.64	1.812	0.750	0.65	0.012
5721-RC	250	8.00	125	0.041	2.125	0.937	0.79	0.062
5722-RC	900	3.75	500	0.175	2.125	0.937	0.75	0.032
5723-RC	1800	2.50	1000	0.55	2.125	0.937	0.75	0.023
5724-RC	4000	1.75	2100	1.16	2.125	0.937	0.74	0.018
5725-RC	8000	1.00	4500	3.34	2.125	0.937	0.74	0.012
5726-RC	25	2.50	16	0.040	0.550	0.220	0.21	0.020
5727-RC	35	2.50	29	0.035	0.700	0.320	0.30	0.025
5728-RC	50	2.50	35	0.060	0.750	0.320	0.28	0.020
5729-RC	100	2.50	70	0.080	0.850	0.360	0.33	0.020
5730-RC	70	3.00	50	0.050	0.850	0.360	0.33	0.025
5731-RC	40	4.00	30	0.025	0.850	0.360	0.34	0.032

"-RC" suffix indicates RoHS compliance.

Precision Voltage Sensor

ID: 1135_0

This voltage sensor measures ±30V DC and connects to an Analog Input or VINT Hub port.

Replaced by 1135_0B






Description | Connection & Compatibility | User Guide | API | Specifications | Resources | Other Voltage Sensors

Product Specifications

Sensor Properties	
Sensor Type	Voltage (DC)
Controlled By	Voltage Input (0-5V)
Sensor Output Type	Non-Ratiometric
Voltage Sensor	
Voltage Difference Max	± 30 V DC
Relative Input Voltage Max	± 40 V DC
Measurement Error Max	0.5 %
Sensor Response Time Max	10 ms
Voltage Offset Max	± 100 mV DC
Electrical Properties	
Supply Voltage	5 V DC
Current Consumption Max	3.6 mA
Sensor Input Impedance	1 MΩ
Output Voltage Min	0 V DC
Output Voltage Max	5 V DC
Physical Properties	
Recommended Wire Size	16 - 26 AWG
Operating Temperature Min	-40 °C
Operating Temperature Max	85 °C

Fully Integrated, Hall Effect-Based Linear Current Sensor IC with 2.1 kVRMS Isolation and a Low-Resistance Current Conductor

Features and Benefits

- Low-noise analog signal path
- Device bandwidth is set via the new FILTER pin
- 5 µs output rise time in response to step input current
- 80 kHz bandwidth
- Total output error 1.5% at T_A = 25°C
- Small footprint, low-profile SOIC8 package
- 1.2 mΩ internal conductor resistance
- 2.1 kVRMS minimum isolation voltage from pins 1-4 to pins 5-8
- 5.0 V, single supply operation
- 66 to 185 mV/A output sensitivity
- Output voltage proportional to AC or DC currents
- Factory-trimmed for accuracy
- Extremely stable output offset voltage
- Nearly zero magnetic hysteresis
- Ratiometric output from supply voltage

TÜV America
Certificate Number:
U8V 06 05 54214 010

Package: 8 Lead SOIC (suffix LC)

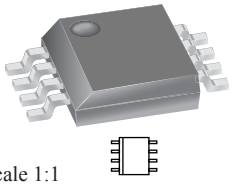

Approximate Scale 1:1

Description

The Allegro® ACS712 provides economical and precise solutions for AC or DC current sensing in industrial, commercial, and communications systems. The device package allows for easy implementation by the customer. Typical applications include motor control, load detection and management, switch-mode power supplies, and overcurrent fault protection. The device is not intended for automotive applications.

The device consists of a precise, low-offset, linear Hall circuit with a copper conduction path located near the surface of the die. Applied current flowing through this copper conduction path generates a magnetic field which the Hall IC converts into a proportional voltage. Device accuracy is optimized through the close proximity of the magnetic signal to the Hall transducer. A precise, proportional voltage is provided by the low-offset, chopper-stabilized BiCMOS Hall IC, which is programmed for accuracy after packaging.

The output of the device has a positive slope (>$V_{IOUT(Q)}$) when an increasing current flows through the primary copper conduction path (from pins 1 and 2, to pins 3 and 4), which is the path used for current sampling. The internal resistance of this conductive path is 1.2 mΩ typical, providing low power loss. The thickness of the copper conductor allows survival of

Continued on the next page…

Typical Application

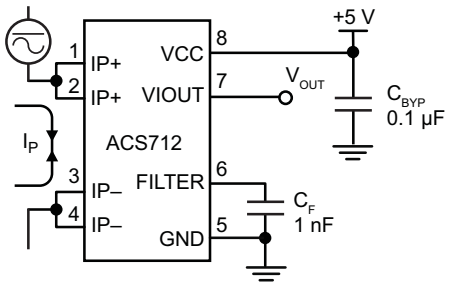

Application 1. The ACS712 outputs an analog signal, V_{OUT}. that varies linearly with the uni- or bi-directional AC or DC primary sampled current, I_P, within the range specified. C_F is recommended for noise management, with values that depend on the application.

Description (continued)

the device at up to 5× overcurrent conditions. The terminals of the conductive path are electrically isolated from the signal leads (pins 5 through 8). This allows the ACS712 to be used in applications requiring electrical isolation without the use of opto-isolators or other costly isolation techniques.

The ACS712 is provided in a small, surface mount SOIC8 package. The leadframe is plated with 100% matte tin, which is compatible with standard lead (Pb) free printed circuit board assembly processes. Internally, the device is Pb-free, except for flip-chip high-temperature Pb-based solder balls, currently exempt from RoHS. The device is fully calibrated prior to shipment from the factory.

Selection Guide

Part Number	Packing*	T_A (°C)	Optimized Range, I_P (A)	Sensitivity, Sens (Typ) (mV/A)
ACS712ELCTR-05B-T	Tape and reel, 3000 pieces/reel	–40 to 85	±5	185
ACS712ELCTR-20A-T	Tape and reel, 3000 pieces/reel	–40 to 85	±20	100
ACS712ELCTR-30A-T	Tape and reel, 3000 pieces/reel	–40 to 85	±30	66

*Contact Allegro for additional packing options.

Absolute Maximum Ratings

Characteristic	Symbol	Notes	Rating	Units
Supply Voltage	V_{CC}		8	V
Reverse Supply Voltage	V_{RCC}		–0.1	V
Output Voltage	V_{IOUT}		8	V
Reverse Output Voltage	V_{RIOUT}		–0.1	V
Output Current Source	$I_{IOUT(Source)}$		3	mA
Output Current Sink	$I_{IOUT(Sink)}$		10	mA
Overcurrent Transient Tolerance	I_P	1 pulse, 100 ms	100	A
Nominal Operating Ambient Temperature	T_A	Range E	–40 to 85	ºC
Maximum Junction Temperature	T_J(max)		165	ºC
Storage Temperature	T_{stg}		–65 to 170	ºC

Isolation Characteristics

Characteristic	Symbol	Notes	Rating	Unit
Dielectric Strength Test Voltage*	V_{ISO}	Agency type-tested for 60 seconds per UL standard 60950-1, 1st Edition	2100	VAC
Working Voltage for Basic Isolation	V_{WFSI}	For basic (single) isolation per UL standard 60950-1, 1st Edition	354	VDC or V_{pk}
Working Voltage for Reinforced Isolation	V_{WFRI}	For reinforced (double) isolation per UL standard 60950-1, 1st Edition	184	VDC or V_{pk}

* Allegro does not conduct 60-second testing. It is done only during the UL certification process.

Parameter	Specification
Fire and Electric Shock	CAN/CSA-C22.2 No. 60950-1-03 UL 60950-1:2003 EN 60950-1:2001

Functional Block Diagram

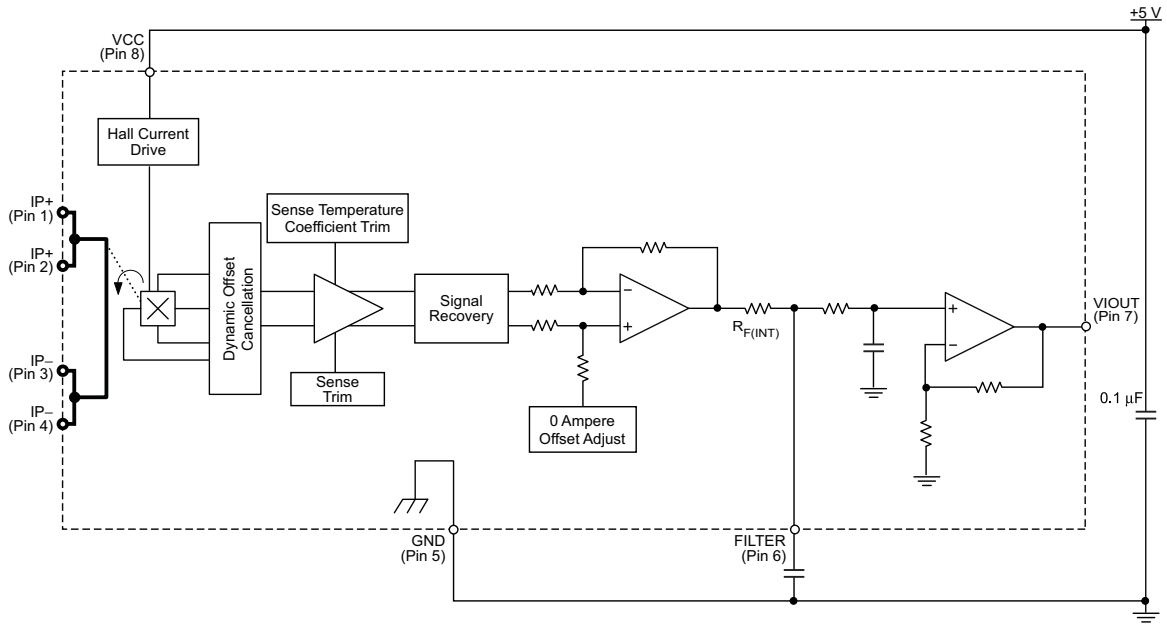

Pin-out Diagram

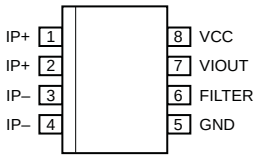

Terminal List Table

Number	Name	Description
1 and 2	IP+	Terminals for current being sampled; fused internally
3 and 4	IP–	Terminals for current being sampled; fused internally
5	GND	Signal ground terminal
6	FILTER	Terminal for external capacitor that sets bandwidth
7	VIOUT	Analog output signal
8	VCC	Device power supply terminal

COMMON OPERATING CHARACTERISTICS[1] over full range of T_A, C_F = 1 nF, and V_{CC} = 5 V, unless otherwise specified

Characteristic	Symbol	Test Conditions	Min.	Typ.	Max.	Units
ELECTRICAL CHARACTERISTICS						
Supply Voltage	V_{CC}		4.5	5.0	5.5	V
Supply Current	I_{CC}	V_{CC} = 5.0 V, output open	–	10	13	mA
Output Capacitance Load	C_{LOAD}	VIOUT to GND	–	–	10	nF
Output Resistive Load	R_{LOAD}	VIOUT to GND	4.7	–	–	kΩ
Primary Conductor Resistance	$R_{PRIMARY}$	T_A = 25°C	–	1.2	–	mΩ
Rise Time	t_r	I_P = I_P(max), T_A = 25°C, C_{OUT} = open	–	3.5	–	µs
Frequency Bandwidth	f	–3 dB, T_A = 25°C; I_P is 10 A peak-to-peak	–	80	–	kHz
Nonlinearity	E_{LIN}	Over full range of I_P	–	1.5	–	%
Symmetry	E_{SYM}	Over full range of I_P	98	100	102	%
Zero Current Output Voltage	$V_{IOUT(Q)}$	Bidirectional; I_P = 0 A, T_A = 25°C	–	V_{CC} × 0.5	–	V
Power-On Time	t_{PO}	Output reaches 90% of steady-state level, T_J = 25°C, 20 A present on leadframe	–	35	–	µs
Magnetic Coupling[2]			–	12	–	G/A
Internal Filter Resistance[3]	$R_{F(INT)}$			1.7		kΩ

[1]Device may be operated at higher primary current levels, I_P, and ambient, T_A, and internal leadframe temperatures, T_A, provided that the Maximum Junction Temperature, T_J(max), is not exceeded.

[2]1G = 0.1 mT.

[3]$R_{F(INT)}$ forms an RC circuit via the FILTER pin.

COMMON THERMAL CHARACTERISTICS[1]

			Min.	Typ.	Max.	Units
Operating Internal Leadframe Temperature	T_A	E range	–40	–	85	°C
					Value	Units
Junction-to-Lead Thermal Resistance[2]	$R_{\theta JL}$	Mounted on the Allegro ASEK 712 evaluation board			5	°C/W
Junction-to-Ambient Thermal Resistance	$R_{\theta JA}$	Mounted on the Allegro 85-0322 evaluation board, includes the power consumed by the board			23	°C/W

[1]Additional thermal information is available on the Allegro website.

[2]The Allegro evaluation board has 1500 mm^2 of 2 oz. copper on each side, connected to pins 1 and 2, and to pins 3 and 4, with thermal vias connecting the layers. Performance values include the power consumed by the PCB. Further details on the board are available from the Frequently Asked Questions document on our website. Further information about board design and thermal performance also can be found in the Applications Information section of this datasheet.

x05B PERFORMANCE CHARACTERISTICS[1] T_A = –40°C to 85°C, C_F = 1 nF, and V_{CC} = 5 V, unless otherwise specified

Characteristic	Symbol	Test Conditions	Min.	Typ.	Max.	Units
Optimized Accuracy Range	I_P		–5	–	5	A
Sensitivity	Sens	Over full range of I_P, T_A = 25°C	180	185	190	mV/A
Noise	$V_{NOISE(PP)}$	Peak-to-peak, T_A = 25°C, 185 mV/A programmed Sensitivity, C_F = 47 nF, C_{OUT} = open, 2 kHz bandwidth	–	21	–	mV
Zero Current Output Slope	$\Delta V_{OUT(Q)}$	T_A = –40°C to 25°C	–	–0.26	–	mV/°C
		T_A = 25°C to 150°C	–	–0.08	–	mV/°C
Sensitivity Slope	ΔSens	T_A = –40°C to 25°C	–	0.054	–	mV/A/°C
		T_A = 25°C to 150°C	–	–0.008	–	mV/A/°C
Total Output Error[2]	E_{TOT}	I_P =±5 A, T_A = 25°C	–	±1.5	–	%

[1]Device may be operated at higher primary current levels, I_P, and ambient temperatures, T_A, provided that the Maximum Junction Temperature, $T_{J(max)}$, is not exceeded.

[2]Percentage of I_P, with I_P = 5 A. Output filtered.

x20A PERFORMANCE CHARACTERISTICS[1] T_A = –40°C to 85°C, C_F = 1 nF, and V_{CC} = 5 V, unless otherwise specified

Characteristic	Symbol	Test Conditions	Min.	Typ.	Max.	Units
Optimized Accuracy Range	I_P		–20	–	20	A
Sensitivity	Sens	Over full range of I_P, T_A = 25°C	96	100	104	mV/A
Noise	$V_{NOISE(PP)}$	Peak-to-peak, T_A = 25°C, 100 mV/A programmed Sensitivity, C_F = 47 nF, C_{OUT} = open, 2 kHz bandwidth	–	11	–	mV
Zero Current Output Slope	$\Delta V_{OUT(Q)}$	T_A = –40°C to 25°C	–	–0.34	–	mV/°C
		T_A = 25°C to 150°C	–	–0.07	–	mV/°C
Sensitivity Slope	ΔSens	T_A = –40°C to 25°C	–	0.017	–	mV/A/°C
		T_A = 25°C to 150°C	–	–0.004	–	mV/A/°C
Total Output Error[2]	E_{TOT}	I_P =±20 A, T_A = 25°C	–	±1.5	–	%

[1]Device may be operated at higher primary current levels, I_P, and ambient temperatures, T_A, provided that the Maximum Junction Temperature, T_J(max), is not exceeded.

[2]Percentage of I_P, with I_P = 20 A. Output filtered.

x30A PERFORMANCE CHARACTERISTICS[1] T_A = –40°C to 85°C, C_F = 1 nF, and V_{CC} = 5 V, unless otherwise specified

Characteristic	Symbol	Test Conditions	Min.	Typ.	Max.	Units
Optimized Accuracy Range	I_P		–30	–	30	A
Sensitivity	Sens	Over full range of I_P, T_A = 25°C	63	66	69	mV/A
Noise	$V_{NOISE(PP)}$	Peak-to-peak, T_A = 25°C, 66 mV/A programmed Sensitivity, C_F = 47 nF, C_{OUT} = open, 2 kHz bandwidth	–	7	–	mV
Zero Current Output Slope	$\Delta V_{OUT(Q)}$	T_A = –40°C to 25°C	–	–0.35	–	mV/°C
		T_A = 25°C to 150°C	–	–0.08	–	mV/°C
Sensitivity Slope	ΔSens	T_A = –40°C to 25°C	–	0.007	–	mV/A/°C
		T_A = 25°C to 150°C	–	–0.002	–	mV/A/°C
Total Output Error[2]	E_{TOT}	I_P = ±30 A, T_A = 25°C	–	±1.5	–	%

[1]Device may be operated at higher primary current levels, I_P, and ambient temperatures, T_A, provided that the Maximum Junction Temperature, T_J(max), is not exceeded.

[2]Percentage of I_P, with I_P = 30 A. Output filtered.

ELECTRONICA DE POTENCIA
POWER SUPPLY
ELECTRONIQUE DE PUISSANCE

FUENTES SERIE *GVD*

ESPECIFICACIONES TÉCNICAS

La diversidad de posibilidades las convierten en un instrumento apreciado.
Les características mas notables son su gran estabilidad delante de variaciones en la carga y en la red; su baja impedancia y su mínimo nivel de ondulación residual.
La salida estabilizada y regulable a partir de 0 voltios, con margen de hasta 30Vcc 60Vcc y desde 0-5A hasta 20A en corriente.
La selección de la tensión e intensidad de salida se gobierna por medio de potenciómetros multivueltas de esmerada precisión.
La lectura de la tensión y la corriente que entrega la fuente es simultánea.
La versión SF (*) dispone de una salida adicional de 5Vcc/1A y otra de ±15Vcc/±1A



CARACTERÍSTICAS PROPIAS				
Modelo	Tensión de salida	Corriente de salida	Dimensiones	Potencia
GVD305 *	0-30Vcc	0 a 5A	325x110x260	150w
GVD310 *	0-30Vcc	0 a 10A	325x135x260	300w
GVD3020	0-30Vcc	0 a 20A	231x160x420	600w
GVD605 *	0-60Vcc	0 a 5A	325x135x260	300w
GVD6010	0-60Vcc	0 a 10A	231x160x420	600w
GVD1442	0-144Vcc	0 a 2A	231x160x420	288w
GVD1444	0-144Vcc	0 a 4A	231x160x420	576w

ESPECIFICACIONES GENERALES		
Entrada	Tensión de red	230Vca ±10% -50Hz
	Protección de entrada	Fusible 5x20mm tipo F
Salida	| Regulación de carga en tensión 0-100%|	<5mV
	| Regulación de red en tensión ±10% |	<1mV
	Ondulación residual	<3mVrms
	Protección de sobrecarga y cortocircuito	si
Ambiente	Temperatura de trabajo	0 +40º
	Humedad	20 ~ 90% no condensable
Normas aplicables	Seguridad	EN60950-1, UL60950-1,
	EMI	Conforme EN55011, EN55022
	Inmunidad	Conforme EN61000-4
	Grado de protección envolvente	IP-20
Instrumentos	Voltímetro digital 3½. Resolución	100mV
	Error medida total del voltímetro	±200mV
	Amperímetro digital 3½. Resolución	10mA
	Error medida total del amperímetro	±20mA

GRELCO, S.A. C/. Sevilla, s/n - 08940 CORNELLÀ -Barcelona – Spain -Tel. +34.933 775 098 -Fax 34.933 775 404
www.grelco.com E-mail: info@grelco.com

L6201
L6202 - L6203

DMOS FULL BRIDGE DRIVER

- SUPPLY VOLTAGE UP TO 48V
- 5A MAX PEAK CURRENT (2A max. for L6201)
- TOTAL RMS CURRENT UP TO
  L6201: 1A; L6202: 1.5A; L6203/L6201PS: 4A
- $R_{DS\ (ON)}$ 0.3 Ω (typical value at 25 °C)
- CROSS CONDUCTION PROTECTION
- TTL COMPATIBLE DRIVE
- OPERATING FREQUENCY UP TO 100 KHz
- THERMAL SHUTDOWN
- INTERNAL LOGIC SUPPLY
- HIGH EFFICIENCY

MULTIPOWER BCD TECHNOLOGY

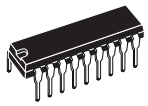

Powerdip 12+3+3

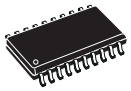

SO20 (12+4+4)

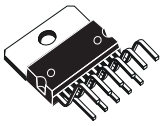

Multiwatt11

PowerSO20

ORDERING NUMBERS:
L6201 (SO20)
L6201PS (PowerSO20)
L6202 (Powerdip18)
L6203 (Multiwatt)

DESCRIPTION

The I.C. is a full bridge driver for motor control applications realized in Multipower-BCD technology which combines isolated DMOS power transistors with CMOS and Bipolar circuits on the same chip. By using mixed technology it has been possible to optimize the logic circuitry and the power stage to achieve the best possible performance. The DMOS output transistors can operate at supply voltages up to 42V and efficiently at high switching speeds. All the logic inputs are TTL, CMOS and μC compatible. Each channel (half-bridge) of the device is controlled by a separate logic input, while a common enable controls both channels. The I.C. is mounted in three different packages.

BLOCK DIAGRAM

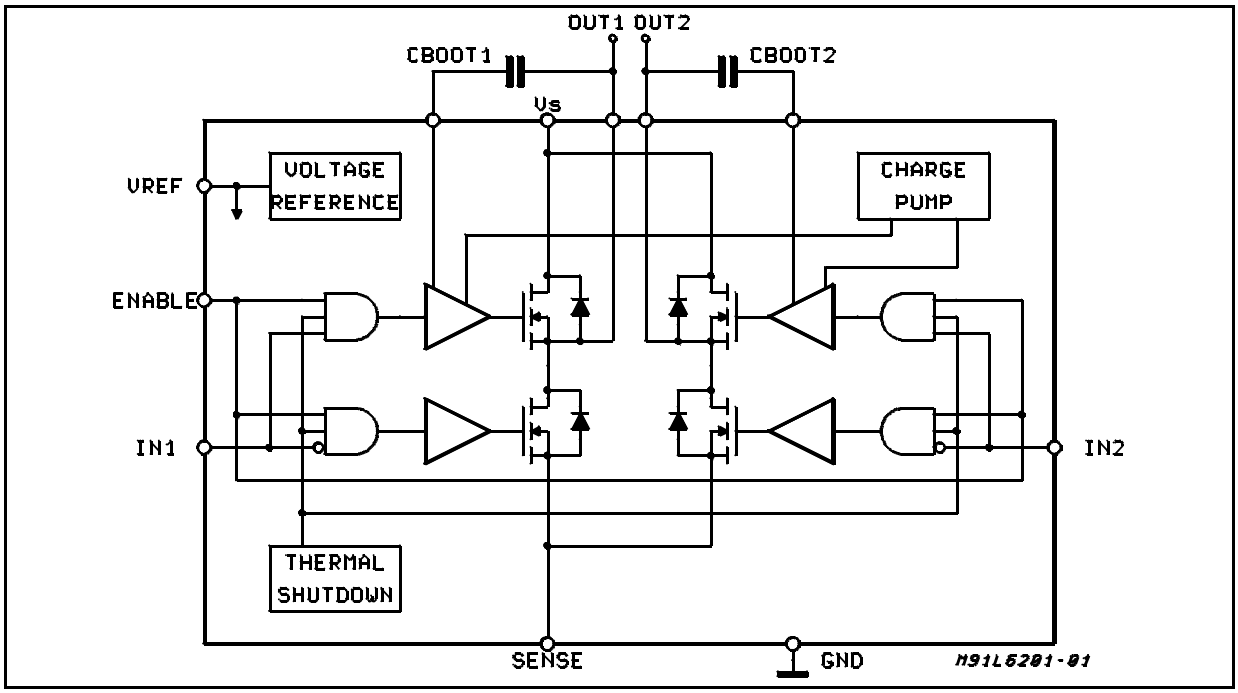

PIN CONNECTIONS (Top view)

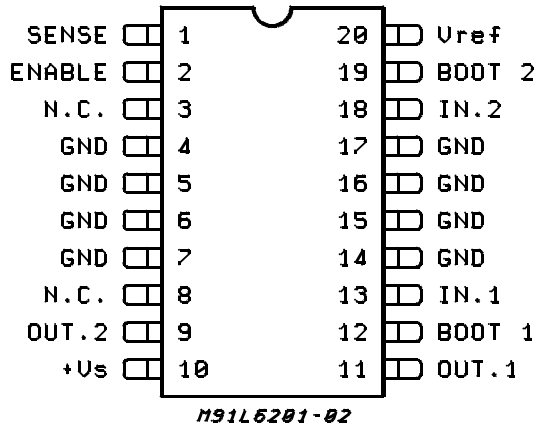

SO20

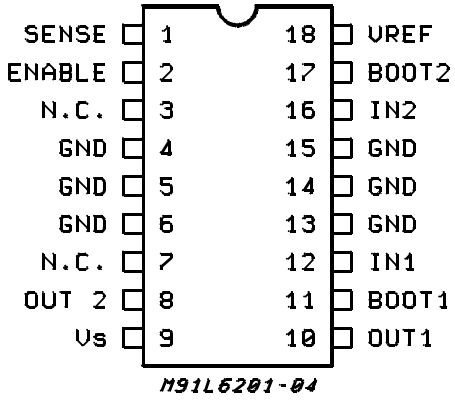

POWERDIP

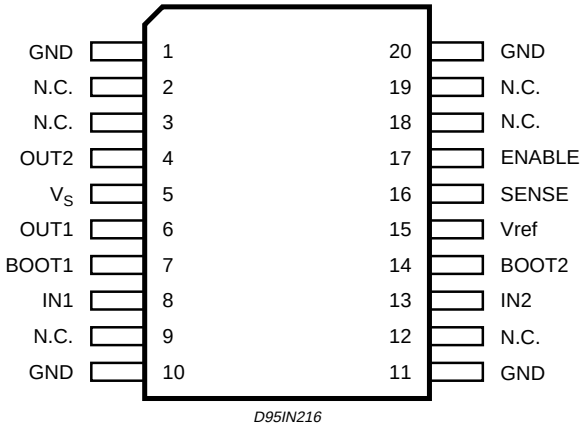

PowerSO20

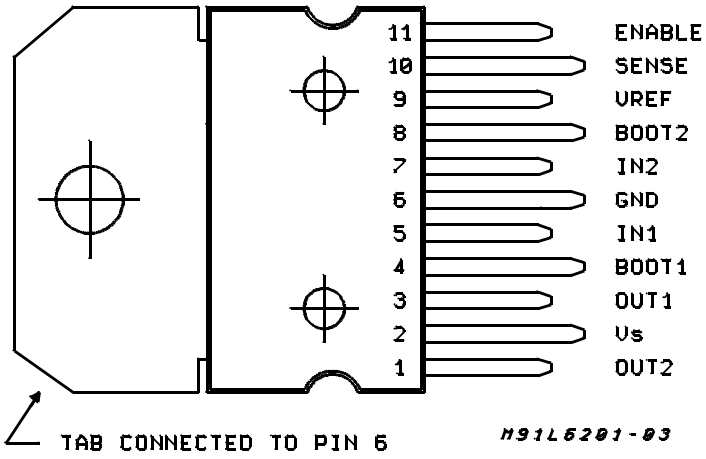

MULTIWATT11

PINS FUNCTIONS

Device				Name	Function
L6201	L6201PS	L6202	L6203		
1	16	1	10	SENSE	A resistor R_{sense} connected to this pin provides feedback for motor current control.
2	17	2	11	ENABLE	When a logic high is present on this pin the DMOS POWER transistors are enabled to be selectively driven by IN1 and IN2.
3	2,3,9,12, 18,19	3		N.C.	Not Connected
4,5	–	4	6	GND	Common Ground Terminal
–	1, 10	5		GND	Common Ground Terminal
6,7	–	6		GND	Common Ground Terminal
8	–	7		N.C.	Not Connected
9	4	8	1	OUT2	Ouput of 2nd Half Bridge
10	5	9	2	V_S	Supply Voltage
11	6	10	3	OUT1	Output of first Half Bridge
12	7	11	4	BOOT1	A boostrap capacitor connected to this pin ensures efficient driving of the upper POWER DMOS transistor.
13	8	12	5	IN1	Digital Input from the Motor Controller
14,15	–	13	6	GND	Common Ground Terminal
–	11, 20	14		GND	Common Ground Terminal
16,17	–	15		GND	Common Ground Terminal
18	13	16	7	IN2	Digital Input from the Motor Controller
19	14	17	8	BOOT2	A boostrap capacitor connected to this pin ensures efficient driving of the upper POWER DMOS transistor.
20	15	18	9	V_{ref}	Internal voltage reference. A capacitor from this pin to GND is recommended. The internal Ref. Voltage can source out a current of 2mA max.

ABSOLUTE MAXIMUM RATINGS

Symbol	Parameter	Value	Unit
V_S	Power Supply	52	V
V_{OD}	Differential Output Voltage (between Out1 and Out2)	60	V
V_{IN}, V_{EN}	Input or Enable Voltage	– 0.3 to + 7	V
I_o	Pulsed Output Current for L6201PS/L6202/L6203 (Note 1) – Non Repetitive (< 1 ms) for L6201 for L6201PS/L6202/L6203 DC Output Current for L6201 (Note 1)	5 5 10 1	A A A A
V_{sense}	Sensing Voltage	– 1 to + 4	V
V_b	Boostrap Peak Voltage	60	V
P_{tot}	Total Power Dissipation: T_{pins} = 90°C for L6201 for L6202 T_{case} = 90°C for L6201PS/L6203 T_{amb} = 70°C for L6201 (Note 2) for L6202 (Note 2) for L6201PS/L6203 (Note 2)	 4 5 20 0.9 1.3 2.3	 W W W W W W
T_{stg}, T_j	Storage and Junction Temperature	– 40 to + 150	°C

Note 1: Pulse width limited only by junction temperature and transient thermal impedance (see thermal characteristics)
Note 2: Mounted on board with minimized dissipating copper area.

THERMAL DATA

Symbol	Parameter		Value				Unit
			L6201	L6201PS	L6202	L6203	
$Rt_{h\ j\text{-}pins}$	Thermal Resistance Junction-pins	max	15	–	12	–	°C/W
$Rt_{h\ j\text{-}case}$	Thermal Resistance Junction Case	max.	–	–	–	3	
$Rt_{h\ j\text{-}amb}$	Thermal Resistance Junction-ambient	max.	85	13 (*)	60	35	

(*) Mounted on aluminium substrate.

ELECTRICAL CHARACTERISTICS (Refer to the Test Circuits; T_j = 25°C, V_S = 42V, V_{sens} = 0, unless otherwise specified).

Symbol	Parameter	Test Conditions	Min.	Typ.	Max.	Unit
V_s	Supply Voltage		12	36	48	V
V_{ref}	Reference Voltage	I_{REF} = 2mA		13.5		V
I_{REF}	Output Current				2	mA
I_s	Quiescent Supply Current	EN = H V_{IN} = L EN = H V_{IN} = H I_L = 0 EN = L (Fig. 1,2,3)		10 10 8	15 15 15	mA mA mA
f_c	Commutation Frequency (*)			30	100	KHz
T_j	Thermal Shutdown			150		°C
T_d	Dead Time Protection			100		ns

TRANSISTORS

OFF						
I_{DSS}	Leakage Current	Fig. 11 V_s = 52 V			1	mA
ON						
R_{DS}	On Resistance	Fig. 4,5		0.3	0.55	Ω
$V_{DS(ON)}$	Drain Source Voltage	Fig. 9 I_{DS} = 1A **L6201** I_{DS} = 1.2A **L6202** I_{DS} = 3A **L6201PS/03**		 0.3 0.36 0.9		 V V V
V_{sens}	Sensing Voltage		– 1		4	V

SOURCE DRAIN DIODE

V_{sd}	Forward ON Voltage	Fig. 6a and b I_{SD} = 1A **L6201** EN = L I_{SD} = 1.2A **L6202** EN = L I_{SD} = 3A **L6201PS/03** EN = L		 0.9 (**) 0.9 (**) 1.35(**)		 V V V
t_{rr}	Reverse Recovery Time	$\frac{dif}{dt}$ = 25 A/µs I_F = 1A L6201 I_F = 1.2A L6202 I_F = 3A L6203		300		ns
t_{fr}	Forward Recovery Time			200		ns

LOGIC LEVELS

$V_{IN\ L}$, $V_{EN\ L}$	Input Low Voltage		– 0.3		0.8	V
$V_{IN\ H}$, $V_{EN\ H}$	Input High Voltage		2		7	V
$I_{IN\ L}$, $I_{EN\ L}$	Input Low Current	V_{IN}, V_{EN} = L			–10	µA
$I_{IN\ H}$, $I_{EN\ H}$	Input High Current	V_{IN}, V_{EN} = H		30		µA

ELECTRICAL CHARACTERISTICS (Continued)
LOGIC CONTROL TO POWER DRIVE TIMING

Symbol	Parameter	Test Conditions	Min.	Typ.	Max.	Unit
t_1 (V_i)	Source Current Turn-off Delay	Fig. 12		300		ns
t_2 (V_i)	Source Current Fall Time	Fig. 12		200		ns
t_3 (V_i)	Source Current Turn-on Delay	Fig. 12		400		ns
t_4 (V_i)	Source Current Rise Time	Fig. 12		200		ns
t_5 (V_i)	Sink Current Turn-off Delay	Fig. 13		300		ns
t_6 (V_i)	Sink Current Fall Time	Fig. 13		200		ns
t_7 (V_i)	Sink Current Turn-on Delay	Fig. 13		400		ns
t_8 (V_i)	Sink Current Rise Time	Fig. 13		200		ns

(*) Limited by power dissipation
(**) In synchronous rectification the drain-source voltage drop VDS is shown in fig. 4 (L6202/03); typical value for the L6201 is of 0.3V.

Figure 1: Typical Normalized I_S vs. T_j

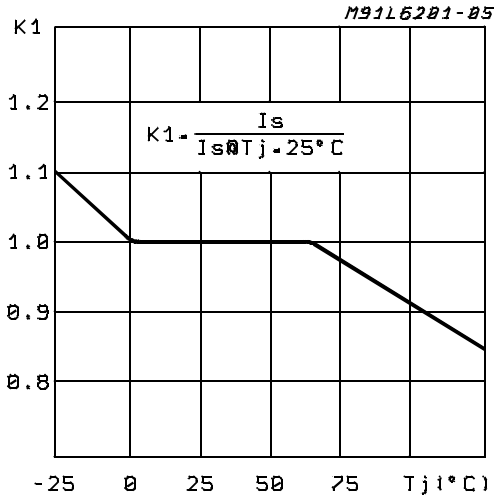

Figure 2: Typical Normalized Quiescent Current vs. Frequency

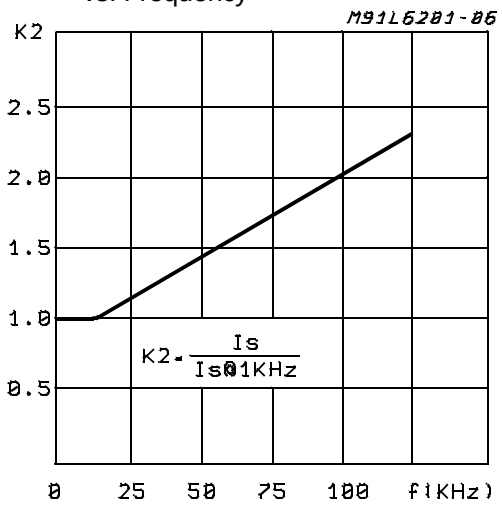

Figure 3: Typical Normalized I_S vs. V_S

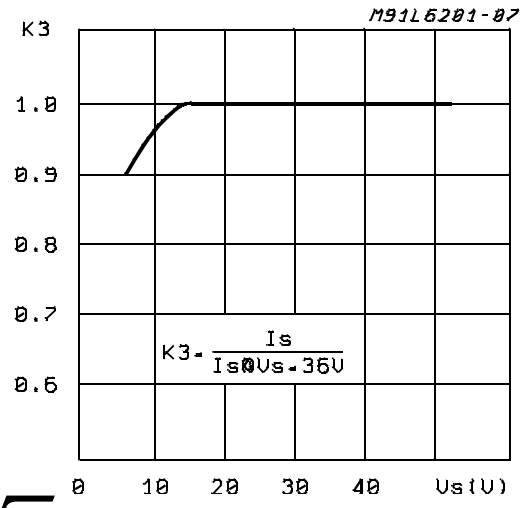

Figure 4: Typical $R_{DS\ (ON)}$ vs. V_S ~ V_{ref}

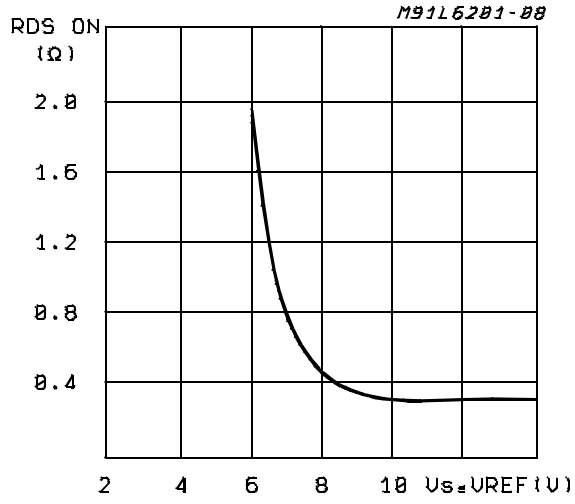

Figure 5: Normalized $R_{DS\ (ON)}$ at 25°C vs. Temperature Typical Values

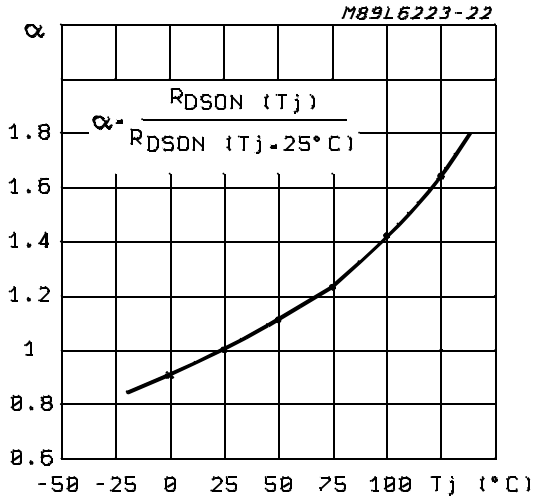

Figure 6a: Typical Diode Behaviour in Synchronous Rectification (L6201)

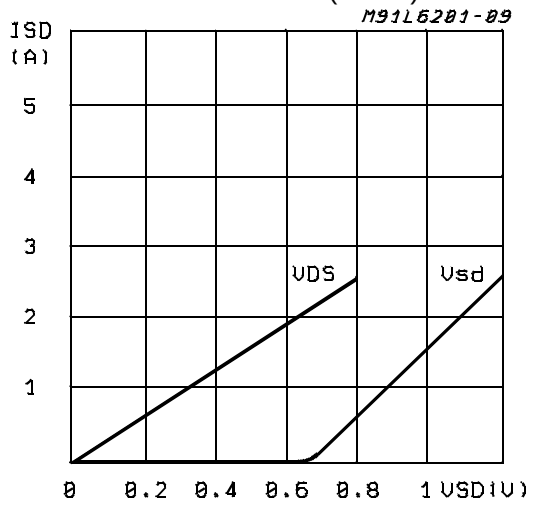

Figure 6b: Typical Diode Behaviour in Synchronous Rectification (L6201PS/02/03)

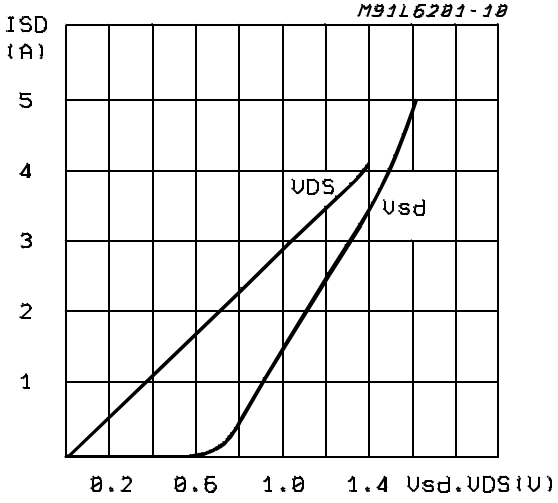

Figure 7a: Typical Power Dissipation vs I_L (L6201)

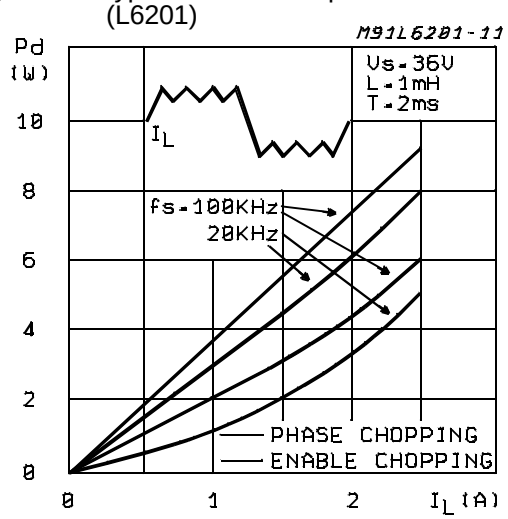

Figure 7b: Typical Power Dissipation vs I_L (L6201PS, L6202, L6203))

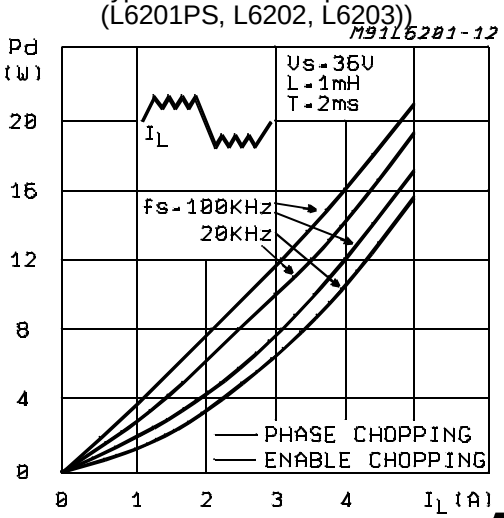

Figure 8a: Two Phase Chopping

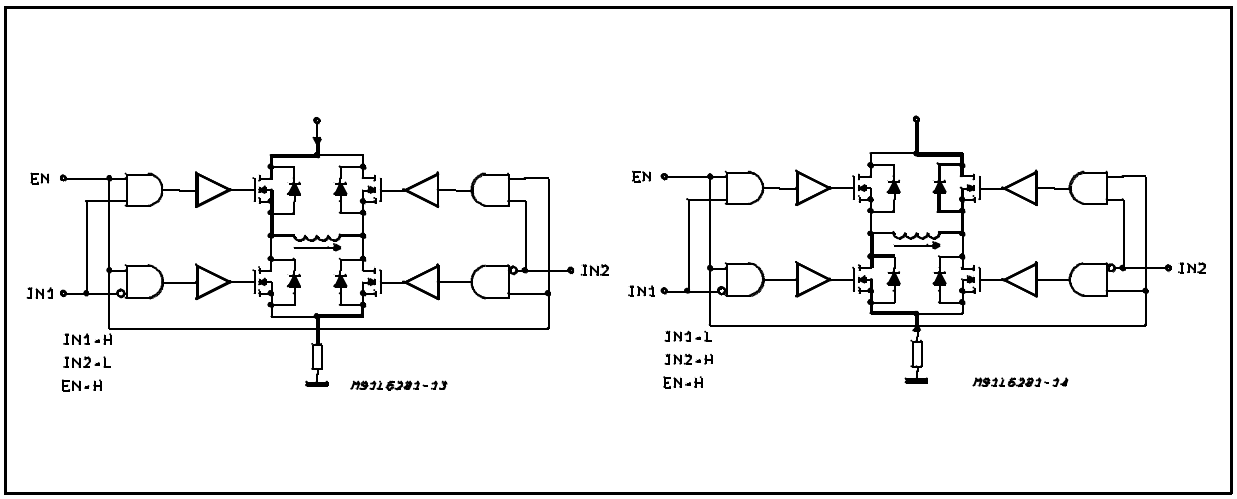

Figure 8b: One Phase Chopping

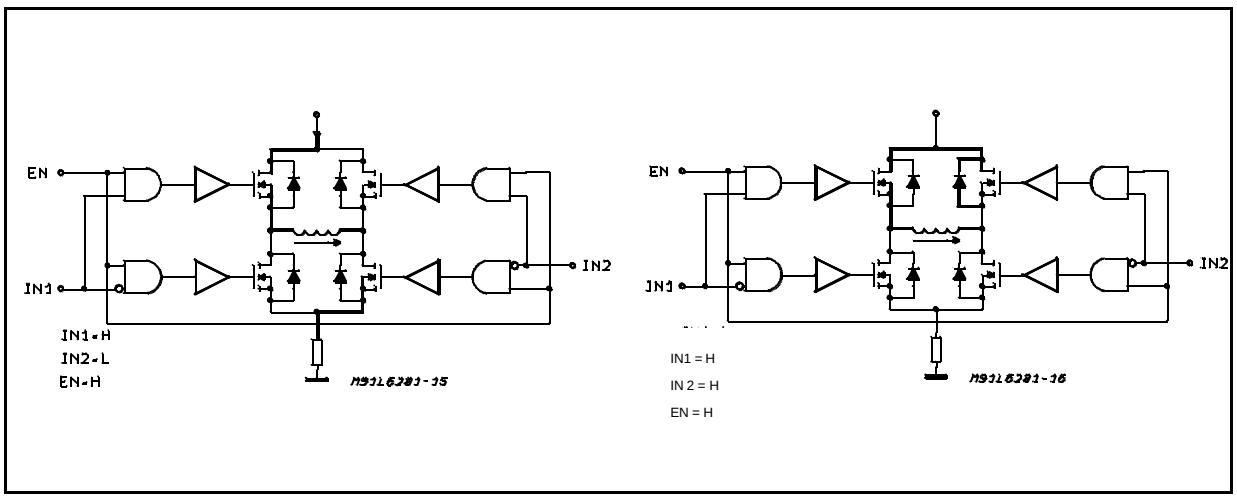

Figure 8c: Enable Chopping

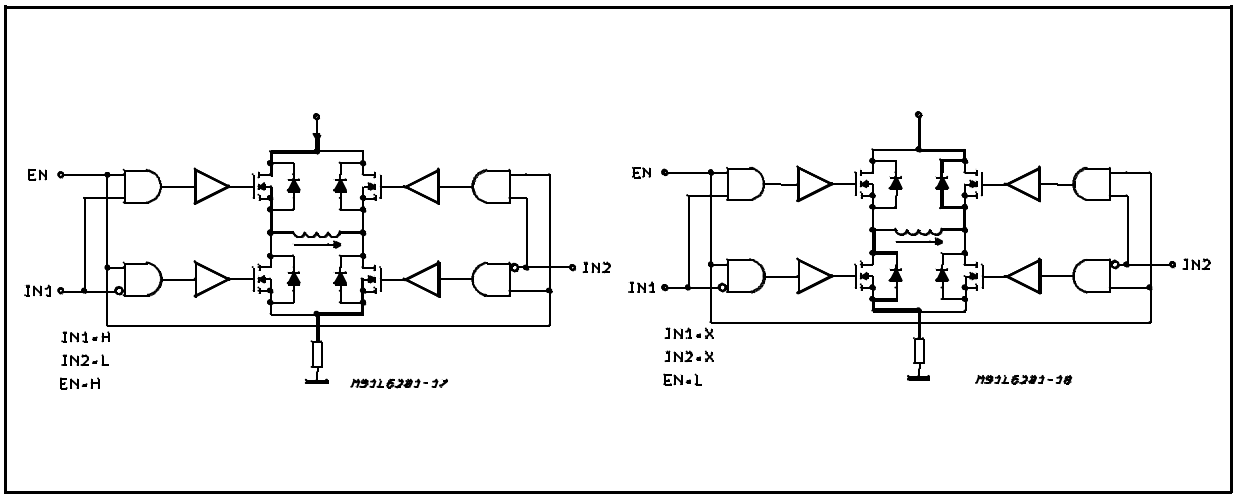

TEST CIRCUITS

Figure 9: Saturation Voltage

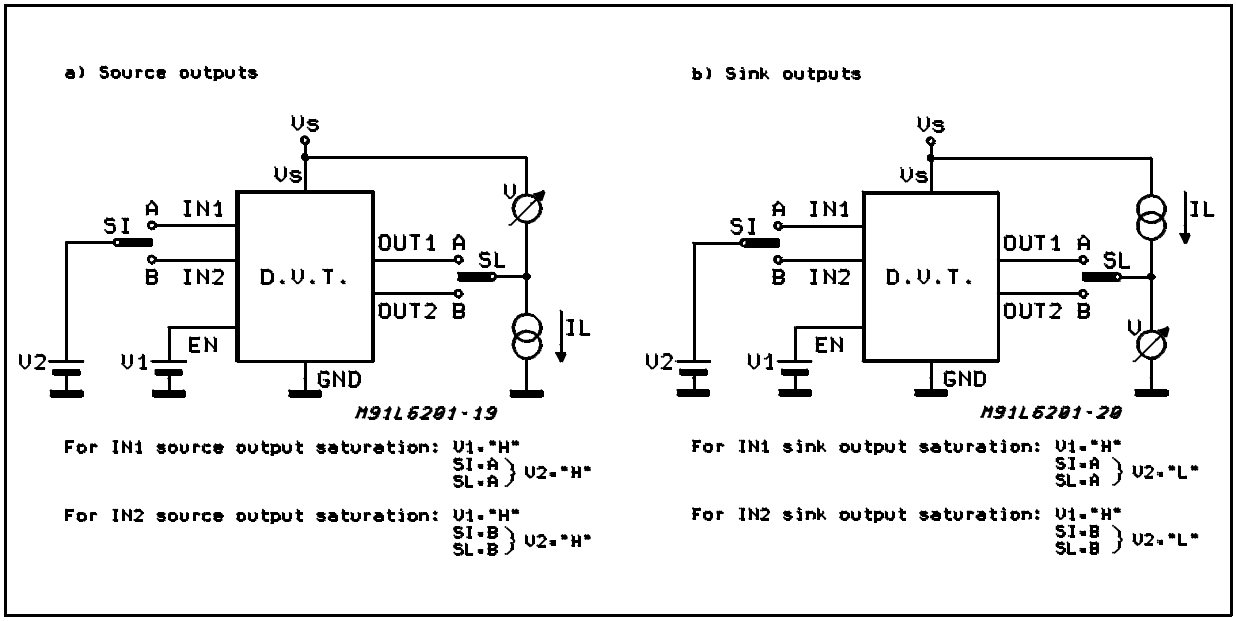

Figure 10: Quiescent Current

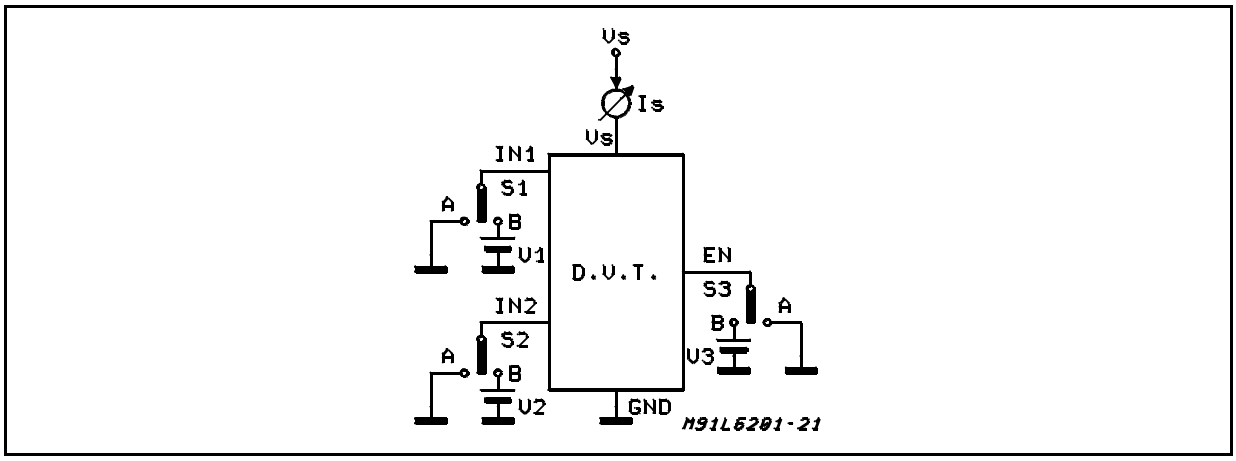

Figure 11: Leakage Current

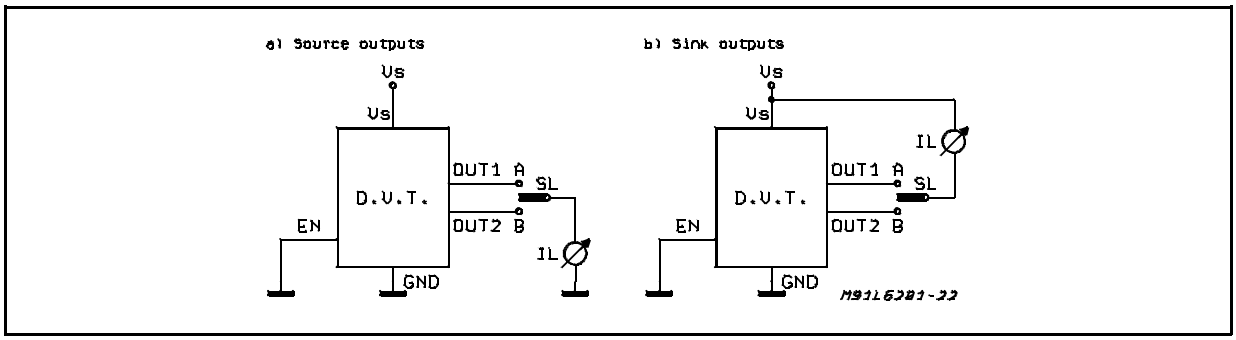

Figure 12: Source Current Delay Times vs. Input Chopper

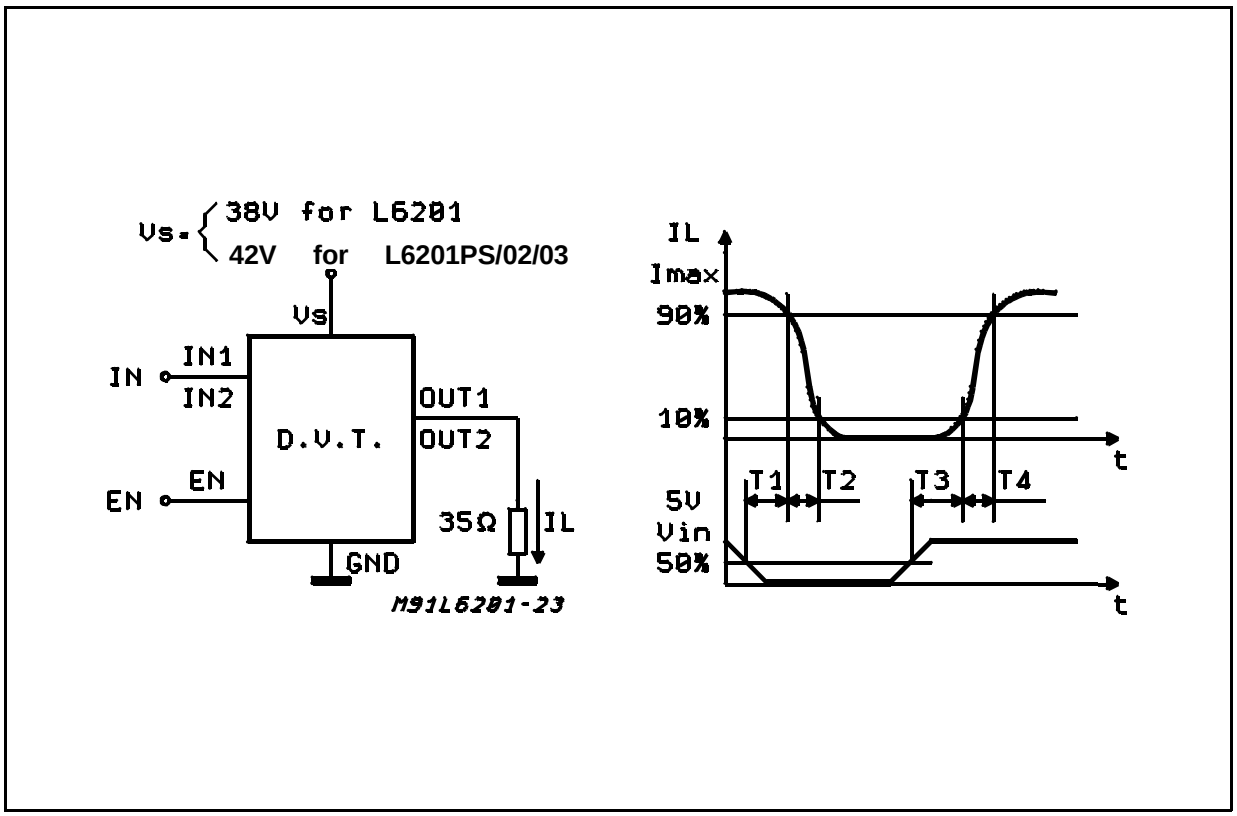

Figure 13: Sink Current Delay Times vs. Input Chopper

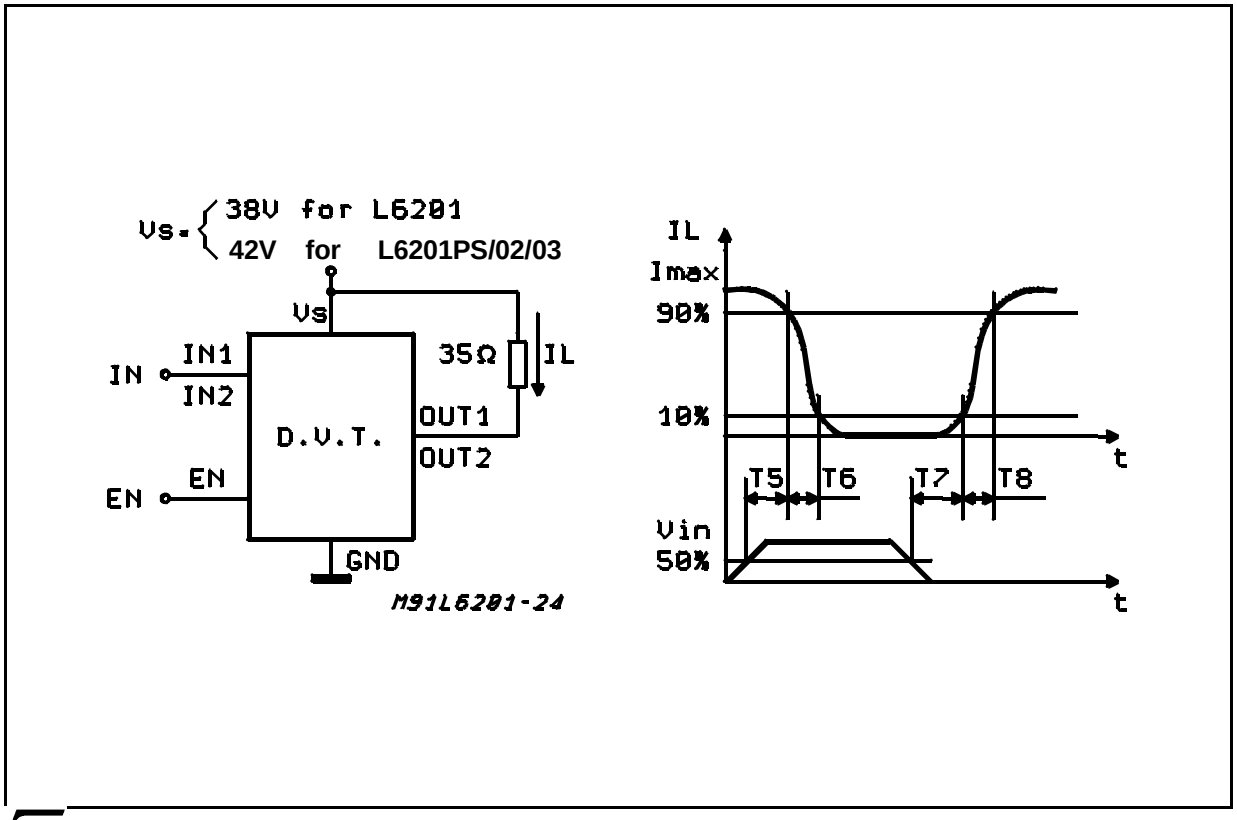

CIRCUIT DESCRIPTION

The L6201/1PS/2/3 is a monolithic full bridge switching motor driver realized in the new Multipower-BCD technology which allows the integration of multiple, isolated DMOS power transistors plus mixed CMOS/bipolar control circuits. In this way it has been possible to make all the control inputs TTL, CMOS and μC compatible and eliminate the necessity of external MOS drive components. The Logic Drive is shown in table 1.

Table 1

Inputs			Output Mosfets (*)
	IN1	IN2	
V_{EN} = H	L	L	Sink 1, Sink 2
	L	H	Sink 1, Source 2
	H	L	Source 1, Sink 2
	H	H	Source 1, Source 2
V_{EN} = L	X	X	All transistors turned oFF

L = Low H = High X = DON't care
(*) Numbers referred to INPUT1 or INPUT2 controlled output stages

Although the device guarantees the absence of cross-conduction, the presence of the intrinsic diodes in the POWER DMOS structure causes the generation of current spikes on the sensing terminals. This is due to charge-discharge phenomena in the capacitors C1 & C2 associated with the drain source junctions (fig. 14). When the output switches from high to low, a current spike is generated associated with the capacitor C1. On the low-to-high transition a spike of the same polarity is generated by C2, preceded by a spike of the opposite polarity due to the charging of the input capacity of the lower POWER DMOS transistor (fig. 15).

Figure 14: Intrinsic Structures in the POWER DMOS Transistors

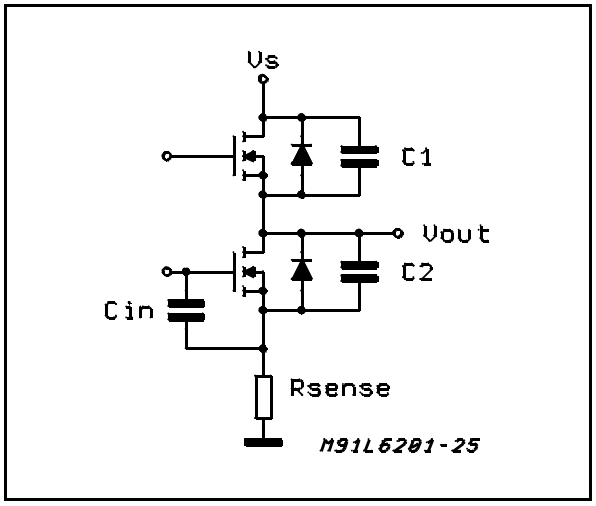

Figure 15: Current Typical Spikes on the Sensing Pin

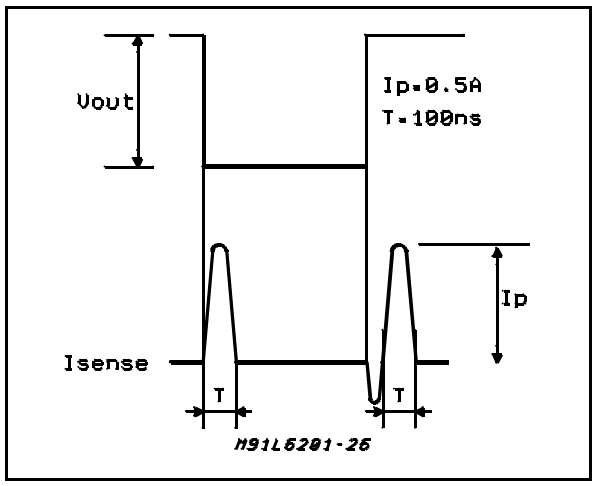

TRANSISTOR OPERATION

ON State

When one of the POWER DMOS transistor is ON it can be considered as a resistor $R_{DS\ (ON)}$ throughout the recommended operating range. In this condition the dissipated power is given by :

$$P_{ON} = R_{DS\ (ON)} \cdot I_{DS}^2 \text{ (RMS)}$$

The low $R_{DS\ (ON)}$ of the Multipower-BCD process can provide high currents with low power dissipation.

OFF State

When one of the POWER DMOS transistor is OFF the V_{DS} voltage is equal to the supply voltage and only the leakage current I_{DSS} flows. The power dissipation during this period is given by :

$$P_{OFF} = V_S \cdot I_{DSS}$$

The power dissipation is very low and is negligible in comparison to that dissipated in the ON STATE.

Transitions

As already seen above the transistors have an intrinsic diode between their source and drain that can operate as a fast freewheeling diode in switched mode applications. During recirculation with the ENABLE input high, the voltage drop across the transistor is $R_{DS\ (ON)} \cdot I_D$ and when it reaches the diode forward voltage it is clamped. When the ENABLE input is low, the POWER MOS is OFF and the diode carries all of the recirculation current. The power dissipated in the transitional times in the cycle depends upon the voltage-current waveforms and in the driving mode. (see Fig. 7ab and Fig. 8abc).

$$P_{trans.} = I_{DS}(t) \cdot V_{DS}(t)$$

Boostrap Capacitors

To ensure that the POWER DMOS transistors are driven correctly gate to source voltage of typ. 10 V must be guaranteed for all of the N-channel DMOS transistors. This is easy to be provided for the lower POWER DMOS transistors as their sources are refered to ground but a gate voltage greater than the supply voltage is necessary to drive the upper transistors. This is achieved by an internal charge pump circuit that guarantees correct DC drive in combination with the boostrap circuit. For efficient charging the value of the boostrap capacitor should be greater than the input capacitance of the power transistor which is around 1 nF. It is recommended that a capacitance of at least 10 nF is used for the bootstrap. If a smaller capacitor is used there is a risk that the POWER transistors will not be fully turned on and they will show a higher RDS (ON). On the other hand if a elevated value is used it is possible that a current spike may be produced in the sense resistor.

Reference Voltage

To by-pass the internal Ref. Volt. circuit it is recommended that a capacitor be placed between its pin and ground. A value of 0.22 µF should be sufficient for most applications. This pin is also protected against a short circuit to ground: a max. current of 2mA max. can be sinked out.

Dead Time

To protect the device against simultaneous conduction in both arms of the bridge resulting in a rail to rail short circuit, the integrated logic control provides a dead time greater than 40 ns.

Thermal Protection

A thermal protection circuit has been included that will disable the device if the junction temperature reaches 150 °C. When the temperature has fallen to a safe level the device restarts the input and enable signals under control.

APPLICATION INFORMATION

Recirculation

During recirculation with the ENABLE input high, the voltage drop across the transistor is RDS (ON)· IL, clamped at a voltage depending on the characteristics of the source-drain diode. Although the device is protected against cross conduction, current spikes can appear on the current sense pin due to charge/discharge phenomena in the intrinsic source drain capacitances. In the application this does not cause any problem because the voltage spike generated on the sense resistor is masked by the current controller circuit.

Rise Time T_r (See Fig. 16)

When a diagonal of the bridge is turned on current begins to flow in the inductive load until the maximum current I_L is reached after a time T_r. The dissipated energy $E_{OFF/ON}$ is in this case :

$$E_{OFF/ON} = [R_{DS\ (ON)} \cdot I_L^2 \cdot T_r] \cdot 2/3$$

Load Time T_{LD} (See Fig.16)

During this time the energy dissipated is due to the ON resistance of the transistors (E_{LD}) and due to commutation (E_{COM}). As two of the POWER DMOS transistors are ON, E_{ON} is given by :

$$E_{LD} = I_L^2 \cdot R_{DS\ (ON)} \cdot 2 \cdot T_{LD}$$

In the commutation the energy dissipated is :

$$E_{COM} = V_S \cdot I_L \cdot T_{COM} \cdot f_{SWITCH} \cdot T_{LD}$$

Where :

$T_{COM} = T_{TURN\text{-}ON} = T_{TURN\text{-}OFF}$

f_{SWITCH} = Chopping frequency.

Fall Time T_f (See Fig. 16)

It is assumed that the energy dissipated in this part of the cycle takes the same form as that shown for the rise time :

$$E_{ON/OFF} = [R_{DS\ (ON)} \cdot I_L^2 \cdot T_f] \cdot 2/3$$

Figure 16.

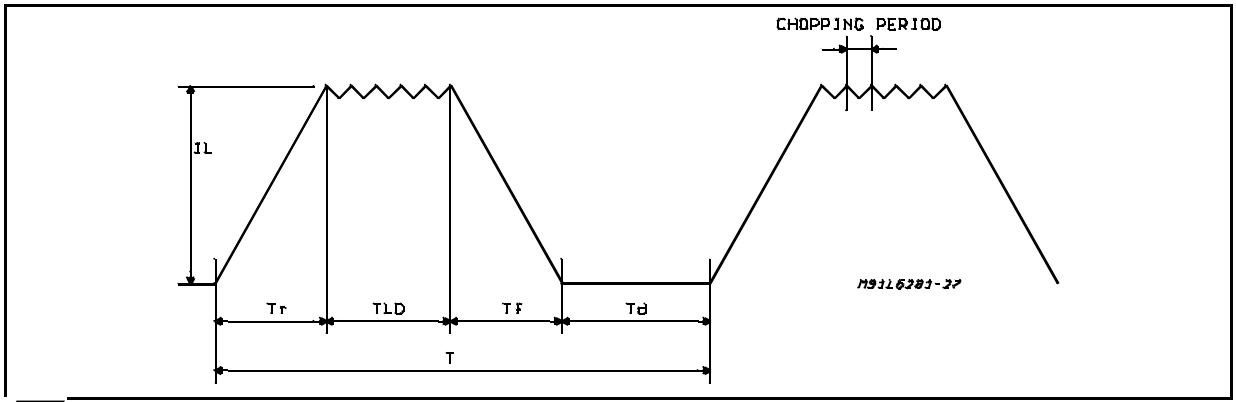

Quiescent Energy

The last contribution to the energy dissipation is due to the quiescent supply current and is given by:

$$E_{QUIESCENT} = I_{QUIESCENT} \cdot V_S \cdot T$$

Total Energy Per Cycle

$$E_{TOT} = E_{OFF/ON} + E_{LD} + E_{COM} +$$
$$+ E_{ON/OFF} + E_{QUIESCENT}$$

The Total Power Dissipation P_{DIS} is simply :

$$P_{DIS} = E_{TOT}/T$$

T_r = Rise time

T_{LD} = Load drive time

T_f = Fall time

T_d = Dead time

T = Period

$T = T_r + T_{LD} + T_f + T_d$

DC Motor Speed Control

Since the I.C. integrates a full H-Bridge in a single package it is idealy suited for controlling DC motors. When used for DC motor control it performs the power stage required for both speed and direction control. The device can be combined with a current regulator like the L6506 to implement a transconductance amplifier for speed control, as shown in figure 17. In this particular configuration only half of the L6506 is used and the other half of the device may be used to control a second motor.

The L6506 senses the voltage across the sense resistor R_S to monitor the motor current: it compares the sensed voltage both to control the speed and during the brake of the motor.

Between the sense resistor and each sense input of the L6506 a resistor is recommended; if the connections between the outputs of the L6506 and the inputs of the L6203 need a long path, a resistor must be added between each input of the L6203 and ground.

A snubber network made by the series of R and C must be foreseen very near to the output pins of the I.C.; one diode (BYW98) is connected between each power output pin and ground as well.

The following formulas can be used to calculate the snubber values:

$R \cong V_S/I_p$

$C = I_p/(dV/dt)$ where:

V_S is the maximum Supply Voltage foreseen on the application;
I_p is the peak of the load current;
dv/dt is the limited rise time of the output voltage (200V/µs is generally used).

If the Power Supply Cannot Sink Current, a suitable large capacitor must be used and connected near the supply pin of the L6203. Sometimes a capacitor at pin 17 of the L6506 let the application better work. For motor current up to 2A max., the L6202 can be used in a similar circuit configuration for which a typical Supply Voltage of 24V is recommended.

Figure 17: Bidirectional DC Motor Control

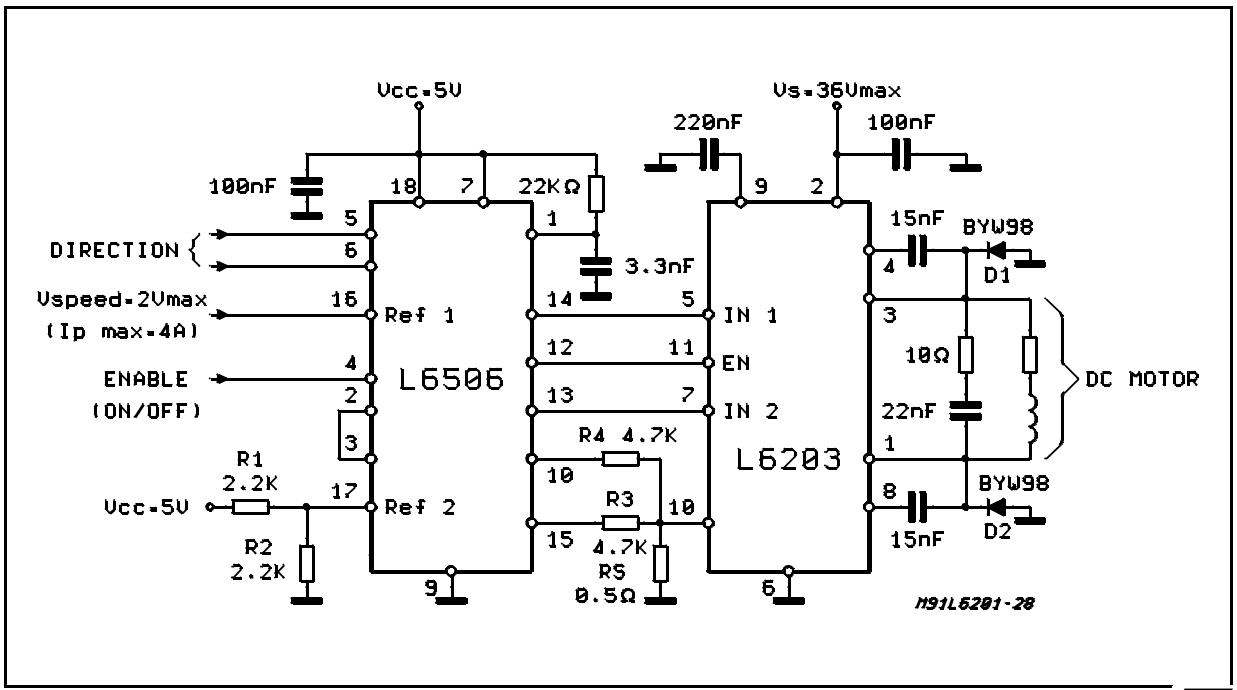

BIPOLAR STEPPER MOTORS APPLICATIONS

Bipolar stepper motors can be driven with one L6506 or L297, two full bridge BCD drivers and very few external components. Together these three chips form a complete microprocessor-to-stepper motor interface is realized.

As shown in Fig. 18 and Fig. 19, the controller connect directly to the two bridge BCD drivers. External component are minimalized: an R.C. network to set the chopper frequency, a resistive divider (R1; R2) to establish the comparator reference voltage and a snubber network made by R and C in series (See DC Motor Speed Control).

Figure 18: Two Phase Bipolar Stepper Motor Control Circuit with Chopper Current Control

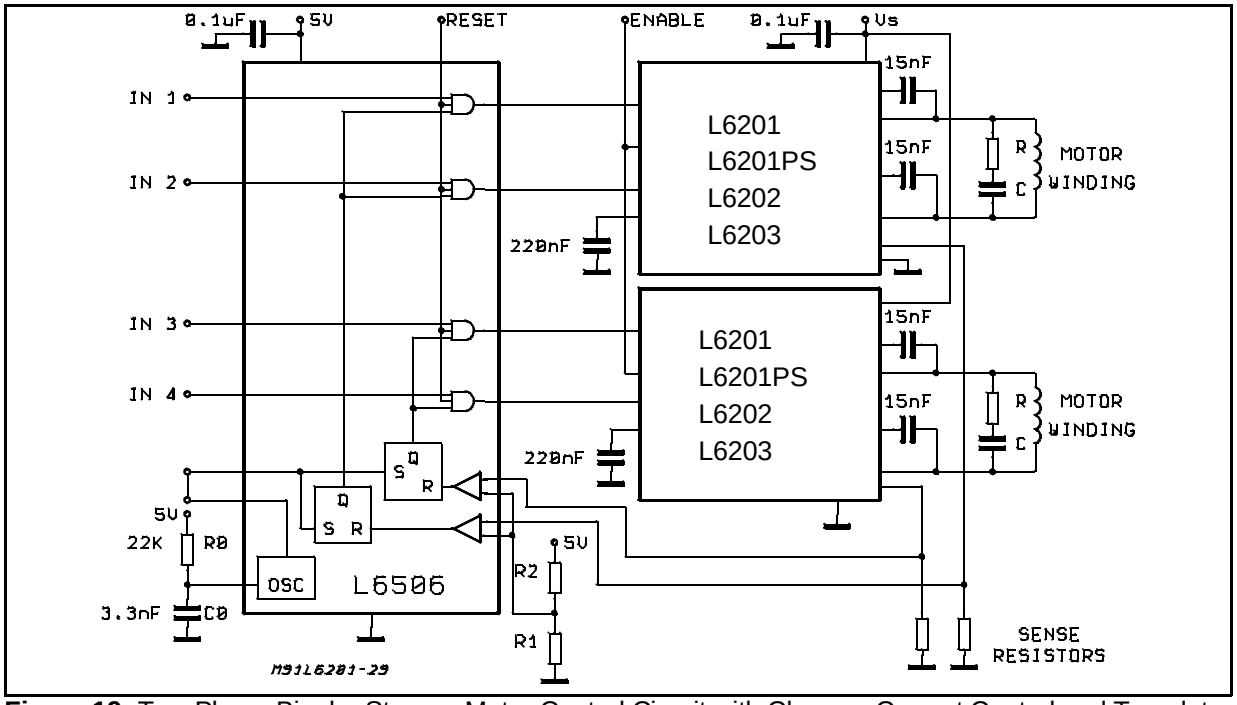

Figure 19: Two Phase Bipolar Stepper Motor Control Circuit with Chopper Current Control and Translator

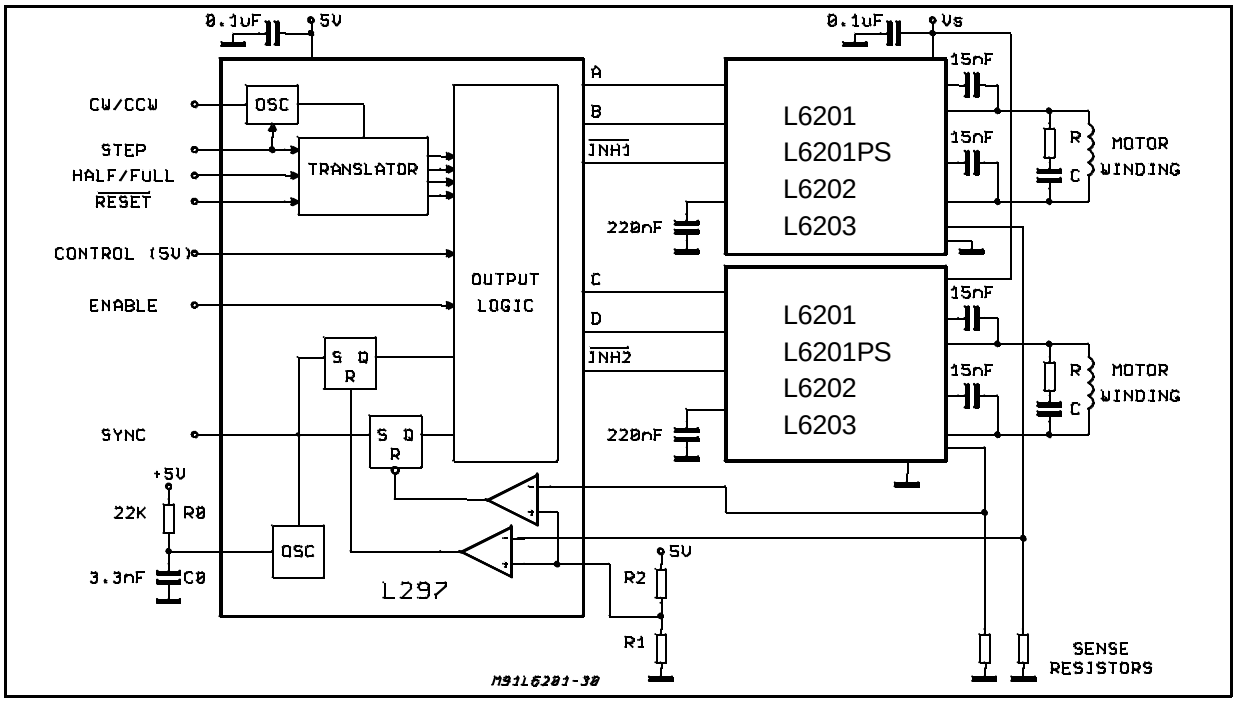

It could be requested to drive a motor at V_S lower than the minimum recommended one of 12V (See Electrical Characteristics); in this case, by accepting a possible small increas in the $R_{DS\ (ON)}$ resistance of the power output transistors at the lowest Supply Voltage value, may be a good solution the one shown in Fig. 20.

Figure 20: L6201/1P/2/3 Used at a Supply Voltage Range Between 9 and 18V

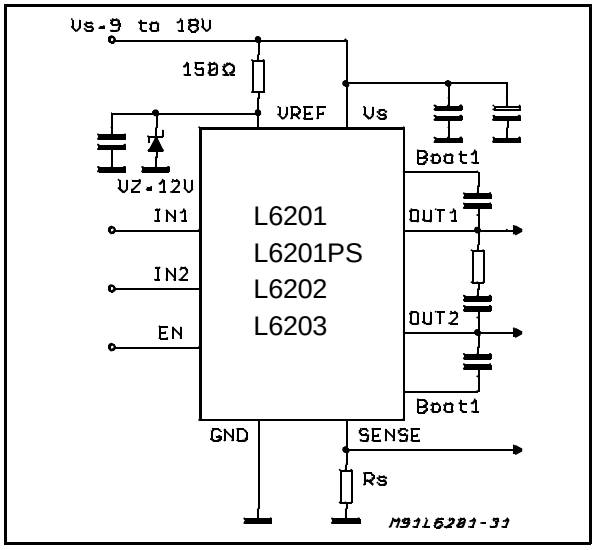

THERMAL CHARACTERISTICS

Thanks to the high efficiency of this device, often a true heatsink is not needed or it is simply obtained by means of a copper side on the P.C.B. (L6201/2).
Under heavy conditions, the L6203 needs a suitable cooling.
By using two square copper sides in a similar way as it shown in Fig. 23, Fig. 21 indicates how to choose the on board heatsink area when the L6201 total power dissipation is known since:

$$R_{Th\ j\text{-}amb} = (T_{j\ max.} - T_{amb\ max}) / P_{tot}$$

Figure 22 shows the Transient Thermal Resistance vs. a single pulse time width.
Figure 23 and 24 refer to the L6202.
For the Multiwatt L6203 addition information is given by Figure 25 (Thermal Resistance Junction-Ambient vs. Total Power Dissipation) and Figure 26 (Peak Transient Thermal Resistance vs. Repetitive Pulse Width) while Figure 27 refers to the single pulse Transient Thermal Resistance.

Figure 21: Typical $R_{Th\ J\text{-}amb}$ vs. "On Board" Heatsink Area (L6201)

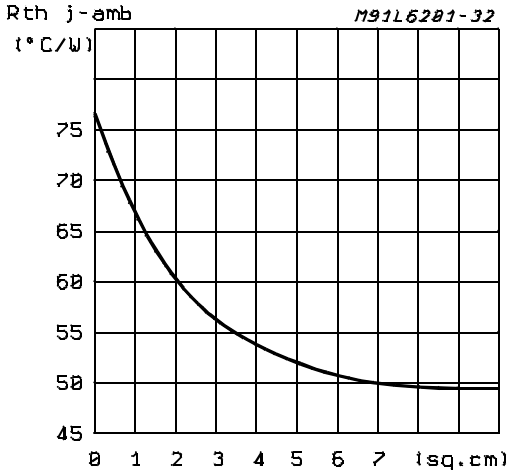

Figure 22: Typical Transient R_{TH} in Single Pulse Condition (L6201)

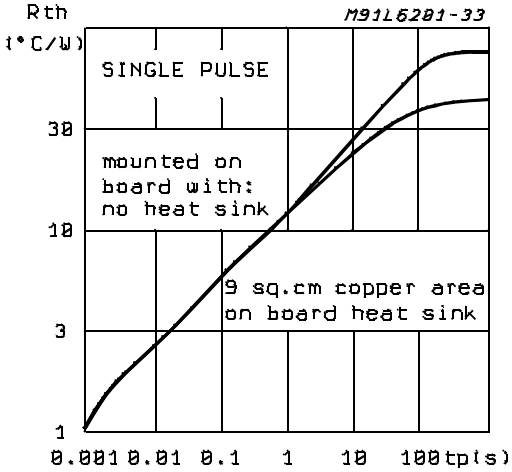

Figurre 23: Typical $R_{Th\ J\text{-}amb}$ vs. Two "On Board" Square Heatsink (L6202)

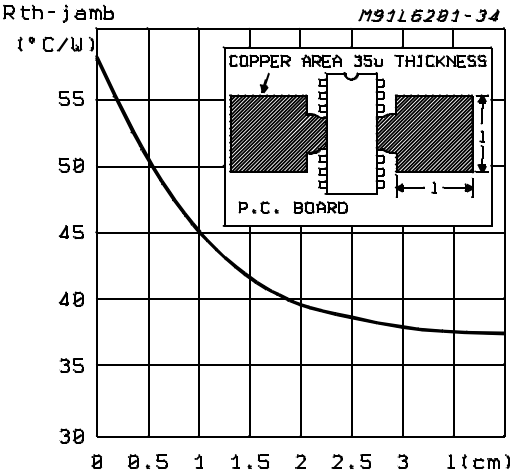

Figure 24: Typical Transient Thermal Resistance for Single Pulses (L6202)

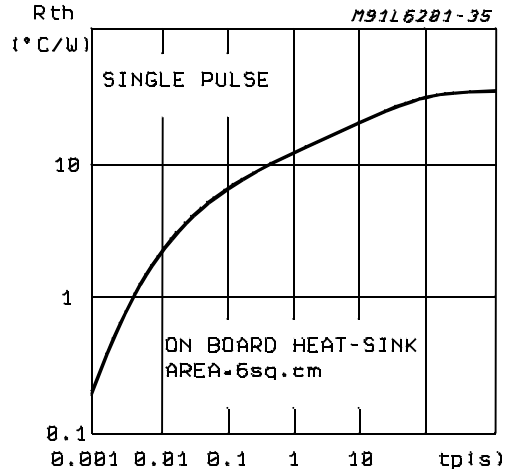

Figure 25: Typical $R_{Th\ J\text{-}amb}$ of Multiwatt Package vs. Total Power Dissipation

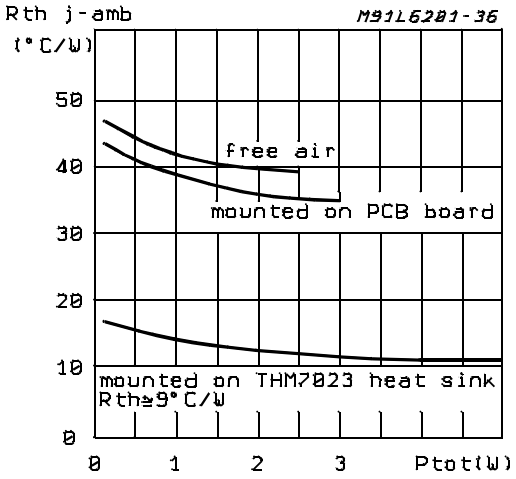

Figure 26: Typical Transient Thermal Resistance for Single Pulses with and without Heatsink (L6203)

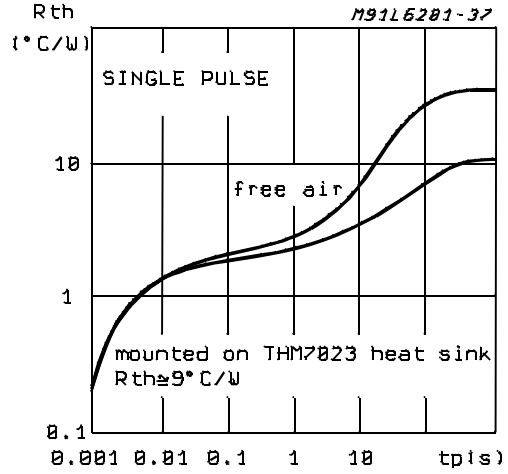

Figure 27: Typical Transient Thermal Resistance versus Pulse Width and Duty Cycle (L6203)

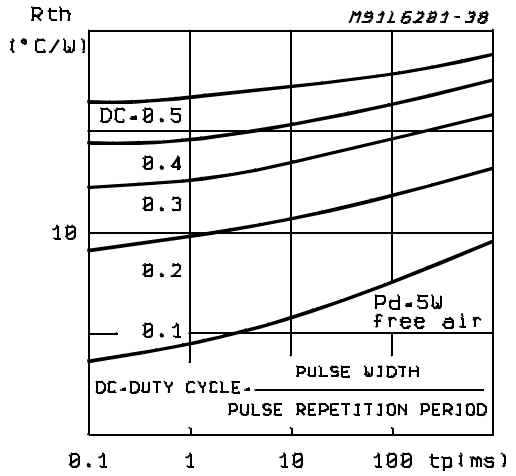

DIM.	mm			inch		
	MIN.	TYP.	MAX.	MIN.	TYP.	MAX.
A			5			0.197
B			2.65			0.104
C			1.6			0.063
D		1			0.039	
E	0.49		0.55	0.019		0.022
F	0.88		0.95	0.035		0.037
G	1.45	1.7	1.95	0.057	0.067	0.077
G1	16.75	17	17.25	0.659	0.669	0.679
H1	19.6			0.772		
H2			20.2			0.795
L	21.9	22.2	22.5	0.862	0.874	0.886
L1	21.7	22.1	22.5	0.854	0.87	0.886
L2	17.4		18.1	0.685		0.713
L3	17.25	17.5	17.75	0.679	0.689	0.699
L4	10.3	10.7	10.9	0.406	0.421	0.429
L7	2.65		2.9	0.104		0.114
M	4.25	4.55	4.85	0.167	0.179	0.191
M1	4.73	5.08	5.43	0.186	0.200	0.214
S	1.9		2.6	0.075		0.102
S1	1.9		2.6	0.075		0.102
Dia1	3.65		3.85	0.144		0.152

OUTLINE AND MECHANICAL DATA

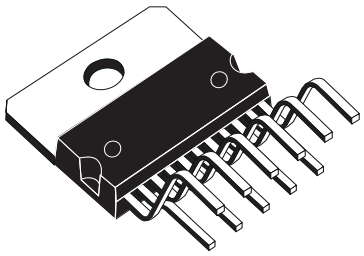

Multiwatt11 V